Analysis of Tsunami Propagation in Coastal Areas
- Lessons from Past Tsunamis -

沿岸域における津波の伝播の解析

－過去の津波の事例をふまえて－

February 2014

Rafael ARÁNGUIZ

アランギス　ラファエル

Analysis of Tsunami Propagation in Coastal Areas
- Lessons from Past Tsunamis -

沿岸域における津波の伝播の解析

－過去の津波の事例をふまえて－

February 2014

Waseda University

Graduate School of Creative Science and Engineering

Rafael ARÁNGUIZ

アランギス　ラファエル

Preface

This thesis is the result of a three-year research, which was carried out at the Department of Civil Engineering, Faculty of Engineering, Universidad Catolica de la Ssma Concepcion, in a joint work with the Department of Civil and Environmental Engineering, Faculty of Creative Science and Engineering, Waseda University, under the supervision of Prof. Tomoya Shibayama. The results of this research have been already published in two journal papers.

Acknowledgements

I would like to thank to my supervisor Prof. Tomoya Shibayama from the Department of Civil and Environmental Engineering of Waseda University for his suggestions, advices, encouragement and support given throughout the research and writing of this dissertation.

I also thank Prof Miguel Esteban from University of Tokyo for his constant advices and encouragement during this research.

I also like to thank the Dirección de Investigación (Research Department) of Universidad Católica de la Ssma Concepción as well as the JICA-SATREPS project between Chile and Japan for partial funding of this research. Furthermore, special thanks go to Dr. Hubert Mennickent, former Dean of Faculty of Engineering and Guillermo Bustamante, former Head of the Department of Civil Engineering of Universidad Católica de la Ssma Concepción, for their support.

I would like to give my special thanks to my wife Paulina for daily encouragement, particularly during difficult times and every time I needed to travel far from home.

Abstract

The Dissertation analyzes the tsunami behavior in coastal areas in Central Chile and improves the understanding of the main variables which affect tsunami propagation and runup. The reason to study this topic is due to diverse effects that the last tsunami, which occurred in February 2010, generated along the coast. The present thesis consists of 5 chapters. The first one is the introduction, which gives a general overview of the study area and the tsunami research after the last events in 2004, 2010 and 2011. The main objective of this research is the analysis of the effect of bathymetry on tsunami propagation and inundation during past events. In addition, the danger posed by future potential tsunamis was investigated, revealing the great threat that these events represent for coastal settlements in the area. Chapter 2 includes a description of tsunami generation in subduction zones, tsunamis propagation and the interaction with the coast. Tsunami propagation over abrupt changes in bathymetry is analyzed in detail, due to the fact that several phenomena are presented in this situation. Some basic concepts related to tsunami inundation are also defined in this chapter, such as runup, inundation height, flow depth and inundation area.

Chapter 3 is the main body of the present research. This chapter deals with the analysis of three past tsunamis generated in the Chilean margin which propagated to the Biobio Region. Numerical simulations of these three events were carried out with the NEOWAVE code. Initial conditions from finite fault models of 2010 and 1960 events were shown to provide good results in the Biobio Region, while uniform initial condition was used in the 1877 tsunami. Spectral analysis of waveforms in both deepwater, the continental shelf and inside the Bay of Concepcion was performed. The analysis also included the maximum inundation heights in both the Bay of Concepcion and the Gulf of Arauco in order to analyze possible effects at the Biobio River mouth. The results showed that both the 2010 and 1877 tsunamis showed well defined waves of large periods inside the Bay of Concepcion. In addition, the maximum inundation took place during the second wave in both cases. Moreover, spectral energy was amplified inside the Bay of Concepcion at a resonant periodic component between 90 and 100min. In the case of the 1960 event, there was also spectral energy amplification but it was not as significant as in the previous two scenarios. Moreover, the amplification took place at higher and lower periodic components than 95min, namely, at 30min and 130min. The

eastern shore of the Gulf showed to have low inundation height at the river mouth. In addition, small tsunami height amplifications were observed at both sides of the river mouth. Section 3 analyzed the effect of the submarine canyon located at the northern side of the Gulf of Arauco, just in front of the Biobio River. The length, width and depth of the canyon were varied, as well as the tsunami wave length. More than 300 simulations were performed using the TUNAMI model. It was found that the submarine canyon has a significant influence on tsunami propagation. The most important variables are the length and width of the canyon, with the depth playing a much less important part. The canyon essentially causes a spatial variation of the wave amplitude along the coastline. While the runup in front of the canyon is always lower than in the case without the canyon, there are tsunami amplification zones at each side of the canyon. Section 3 also included the resonance analysis of the Bay of Concepcion. The natural oscillation modes of the Bay were determined by means of Empirical Orthogonal Functions. The fundamental oscillation period was found to be 95min, which coincides with the resonant period from the spectral analysis of 2010 and 1877 event, i.e. the tsunami waves excited the fundamental period of the Bay. The second and third oscillation modes of the Bay have periods of 37 and 32 min, respectively, which are close to one of the resonant periodic components during the 1960 tsunami. Therefore, the relative low amplification given by the 1960 tsunami was due to excitation of a higher frequency oscillation rather than the fundamental period.

The effect of possible future tsunamis from northern Chile on the Bay of Concepcion was analyzed in Chapter 4. Hypothetical scenarios with magnitudes ranging from 8.0 to 8.8 were defined by means of empirical expressions of magnitude and size of the earthquake. The focal depth as well as the tidal level was varied for each event. A polynomial expression was fitted to the maximum tsunami wave amplitude at Talcahuano. Based on those results, the first forecast model for Talcahuano with pre-computing tsunami sources was developed. This model uses the earthquake magnitude, the focal depth and tidal level to determine maximum tsunami amplitude at Talcahuano. Finally, Chapter 5 presents the conclusions of the present research as well as indicates areas of research that should be prioritized in the future.

Resumen

La presente tesis doctoral analiza el comportamiento de tsunamis en zonas costeras de Chile Central y mejora la comprensión de las principales variables que afectan tanto la propagación de tsunamis como la inundación. El motivo para estudiar este tema se debe a los diferentes efectos que el último tsunami, que ocurrió en Febrero de 2010, generó a los largo de la costa. El primer capítulo de la tesis es una introducción, que entrega una visión general sobre el área de estudio y la investigación en tsunamis después de los últimos eventos de 2004, 2010 y 2011. El objetivo general es analizar los efectos de la batimetría sobre la propagación de tsunamis así como la inundación para eventos pasados. Además, se investigó el peligro potencial de eventos futuros, revelando que existe una gran amenaza en las zonas costeras del área de estudio. El capítulo 2 incluye una descripción de la generación de tsunamis en zonas de subducción así como la propagación e interacción con la costa. Se describe en detalle el comportamiento de tsunamis propagándose sobre cambios bruscos de batimetría debido a que varios fenómenos se identifican en este caso particular. En este capítulo también se explican algunos conceptos básicos, tales como runup, altura de inundación, profundidad de flujo y área de inundación.

El capítulo 3 es el cuerpo principal de la presente investigación. Este capítulo analiza tres tsunamis pasados que se generaron en la zona de subducción chilena y que se propagaron hacia la Región del Biobío. Se realizaron simulaciones numéricas de estos tres eventos utilizando el código NEOWAVE. Las condiciones iniciales de los tsunamis de 2010 y 1960 mostraron buenos resultados en la Región del Biobío usando modelos de fallas finitas, mientras que para el evento de 1877 se utilizó un modelo de falla uniforme. Se realizó un análisis espectral de la variación de la superficie libre tanto en aguas profundas, la plataforma continental como la Bahía de Concepción. Se incluyó también un análisis de las alturas máximas de inundación en la Bahía de Concepción y en el Golfo de Arauco, este último con el fin de analizar posibles efectos en la desembocadura del Río Biobío. Los resultados mostraron que los tsunamis de 2010 y 1877 evidenciaron ondas bien definidas de gran periodo al interior de la Bahía de Concepción. Además, en ambos casos se observó que la máxima altura de inundación ocurrió durante la segunda onda. Adicionalmente, la energía espectral se amplificó al interior de la Bahía para una componente periódica entre 90 y 100 min. Para el caso del evento de 1960, también se observó amplificación de la energía espectral pero no fue

tan significativa como en los casos anteriores. Además, la amplificación ocurrió para componentes periódicas más altas y más bajas que 95 min, en particular para 30 y 130 min. Se observó una altura de inundación baja en la costa Este del Golfo de Arauco y zonas de amplificación en ambos costados de la desembocadura del Río Biobío. La sección 3 analiza el efecto del cañón submarino ubicado justo en la entrada norte del Golfo de Arauco frente de la desembocadura del río. Se varió la longitud, ancho y profundidad del cañón submarino así como la longitud de onda del tsunami y se realizaron más de 300 modelaciones numéricas con el modelo TUNAMI. Se pudo concluir que el cañón submarino tiene una gran influencia en la propagación de tsunamis y las variables más importantes son la longitud y ancho del cañón, no así la profundidad. Se observó que el cañón genera una variación espacial en la amplitud del tsunami a lo largo de la costa. Mientras que el runup frente al cañón es siempre menor al caso sin cañón, existen zonas de amplificación de la amplitud de tsunami en la costa a ambos lados del cañón. La sección 3 también incluye un análisis de resonancia de tsunamis en la Bahía de Concepción y se calcularon los periodos naturales mediante Funciones Ortogonales Empíricas. Se encontró que el periodo fundamental es 95 min el cual coincide con las componentes periódicas observadas para los eventos de 2010 y 1877, es decir, los tsunamis excitaron el modo natural de oscilación de la Bahía de Concepción. Se obtuvo que el segundo y tercer modo de oscilar de la Bahía poseen períodos de 37 y 32 min, respectivamente, los cuales se aproximan a las componentes periódicas observadas para el tsunami de 1960. Por lo tanto, la altura de inundación relativamente baja del tsunami de 1960 en la Bahía de Concepción, se debió a que el tsunami excitó frecuencias más altas de oscilación en lugar del periodo fundamental.

En el capítulo 4 se analizó el efecto en la Bahía de Concepción de posibles tsunamis futuros generados en el norte de Chile. Se utilizaron expresiones empíricas del tamaño de la zona de ruptura de un terremoto en función de su magnitud y se definieron eventos hipotéticos de magnitudes entre Mw 8.0 y 8.8. Además, se varió la profundidad focal y nivel de marea para cada evento seleccionado. Posteriormente, se ajustó una función parabólica a la máxima amplitud del tsunami en Talcahuano. De este modo, se construyó el primer modelo de pronóstico de inundación por tsunami en Talcahuano usando eventos pre-modelados. Este modelo de pronóstico utiliza la magnitud del terremoto, la profundidad focal y el nivel de marea para determinar la máxima inundación en Talcahuano. Finalmente, el capítulo 5 presenta las conclusiones de esta investigación y las áreas prioritarias de futuras investigaciones.

Contents

Chapter 1 Introduction

Chile is often referred to as one of the most earthquake prone countries in the world. In fact the country is located along the subduction zone of the Nazca plate beneath the South American Plate. In this area there have been great earthquakes of magnitude over 8, which usually cause changes in coastal morphology and generate devasting tsunamis (Barrientos, 2007).

Earthquake and tsunami records in Chile began with the arrival of Spanish settlements in the middle of sixteen century. Nevertheless, according to ancient Indian Chronicles, in 1513/1515 a severe earthquake occurred and the ocean level showed marked fluctuations (Soloviev and Go,1975). Lomnitz (1970) indentified a total of 32 large earthquakes in a descriptive catalogue of major earthquakes and tsunamis. In this work, only earthquakes of estimated magnitude over 7.5 were considered for the period 1570 to 1953. In addition, at least 10 destructive tsunamis were also identified. However, Lagos (2000) extended this catalogue considering earthquakes of magnitude above 6.0 in the period 1562 to 1997, and a total of 102 tsunamis were identified. Moreover, a classification of these events based on the Imamura e Iida scale was performed. It was possible to observe that 4 events fall within tsunami magnitude 4 category, 10 are tsunami magnitude 3, while 66 events are classified as tsunami magnitude 0.

The largest earthquake ever recorded, the Magnitude 9.5 Valdivia earthquake in 1960, also took place in Chile. The earthquake and tsunami wave were generated in southern Chile, and the rupture area had an estimated length of 1000km (Barrientos and Ward, 1990). The tsunami affected not only the Chilean coast, but also the entire Pacific Ocean coast. Maximum runup of 25m was measured in Chile, while tsunami amplitudes reached 3.1, 3.3, and 1.7m in California, Alaska and New Zeland, respectively (Takahashi, 1961). In addition, very large inundation heights were measured in Japan, namely 4.9, 4.2 and 2.8m, in localities such as Ofunato, Onagawa, and Kamaishi, respectively (Takahashi, 1961). After this event, mitigation measures such as tsunami breakwaters started to be constructed in Kamaishi and Ofunato (Murata et al., 2010), and the Pacific Tsunami Warning Center was implemented in Hawaii.

In 2004, however, another large earthquake tsunami was generated in the Indian Ocean. 12 Countries were affected causing more than 290,000 casualties (Ioualalen et al., 2007). After this event, the attention of tsunami researchers started to focus more on tsunami disaster prevention and education and a greater number of countries got

involved in tsunami research. In addition, tsunami numerical modeling became widely used for tsunami inundation mapping around the world. In a similar manner the 2010 Chile tsunami, generated by a magnitude 8.8 earthquake in central Chile, attracted the attention of researchers due to low number of casualties (only 125) despite the fact that the Chilean Tsunami Warning System did not function properly. Since the tsunami took place during the summer season, investigation revealed that most of the casualties were not people living in coastal zones, but tourists (Fritz et al., 2011). As a matter of fact, a small town called Tirúa (See Figure 1) did not suffer any casualties, despite the largest run up (around 20m) being measured there (Mikami et al., 2011). This place also experienced large inundation height during 1960 tsunami, and therefore people evacuated to higher ground immediately after the earthquake, despite that there was no official evacuation plan in that place.

In March 2011, an earthquake magnitude 9.0 generated the so called *Great Eastern Japan Earthquake and Tsunami,* which devastated large parts of Japan's north-eastern coastline. Japan had a number of coastal protective structures such as dikes and breakwaters; however, the idea that this kind of measures can protect the lives of inhabitants of coastal areas has been abandoned after the event. As a matter of fact, the Kamaishi and Ofunato breakwaters were overflowed and partially destroyed and subsequently hard measures are only considered to be effective in protecting properties against the more frequent but lower magnitude events (Shibayama et al., 2013).

All the previously mentioned events helped researchers to realize that both hard and soft mitigation measures are important. Moreover mitigation measures must consider local geographic, social and economic variables before being proposed. On that ground, it is important to continue carrying out research into areas such as tsunami generation, propagation and impact on the coastline at any specific location. As a matter of fact, the tsunami resonances in bays as well as the effect of submarine canyons on tsunami propagation need to be better understood prior to tsunami counter measures being proposed. In addition, the analysis of possible future tsunamis is also important so that local authorities can include these phenomena in their city planning tools.

1.1. Significance of the study

The simplest definition of Risk is a function of Hazard and Vulnerability (Birkman, 2006). Since the natural hazard depends on physical conditions, which cannot be reduced, the only way to reduce the risk is by means of vulnerability reduction.

According to the World Conference on Disaster Reduction "*the starting point for reducing disaster risk lies in the knowledge of the hazards and the physical, social, economic and environmental vulnerabilities*" (UN, 2005). Therefore, the knowledge of the hazard must be one of the most important tasks prior to risk reduction.

The development of numerical models has been important in understanding tsunami hazards. At the same time, the occurrence of large tsunamis during the last 10 years and the instrumental recording of them, have enormously contributed to the improvement of such numerical models (Murata et al., 210). On that ground, numerical models may be used not only for simulation of past events, but also for hypothetical future scenarios, and thus proper mitigation measures can be proposed.

After the 2010 Chile tsunami, national and regional authorities have been focusing on tsunami mitigation measures. In fact, the Government requested tsunami inundation maps for 46 places along the coast of the Biobio Region before beginning the reconstruction of the affected villages. Some of the proposed countermeasures included concrete walls, embankments and control forests in older developed areas. However, behavior of past and future tsunamis is poorly understood up to now. As a matter of fact, the 2010 Chile tsunami showed to have diverse effects along the coast. While the maximum runup in Dichato (36.54°W 72.94°S) was 9m (Fritz et al., 2011), 40km southwest at the mouth of the Biobio River the runup was less than 2m (Quezada et at., 2010), and 50km southwest from this point, the runup reached up to 8m in Tubul town (Fritz et al., 2011) and 18 m in Llico (Mikami et al., 2011) (See Figure 1). In addition the 1877 Iquique tsunami generated an inundation height of 3m in Talcahuano, despite the tsunami source being located 1,500km north. Therefore, the main contribution of the present work is related to understanding of the tsunami hazard in the Biobio Region, which could improve the risk assessment and subsequently, the tsunami risk reduction.

1.2. Objective and scope of the study

The general objective of the present research is to analyze the effect of bathymetry and coastal morphology on tsunami propagation in coastal areas. The research is focused on tsunami behavior in the areas recently affected by the 2010 Chile Tsunami, namely the Biobio Region.

The specific objectives of the present study are:

- To analyze, by means of numerical simulations, the behavior of past tsunamis in the Biobio Region, mainly in the Bay of Concepcion and the Gulf of Arauco.
- To analyze the effect of local seabed morphology, such as submarine canyons, on tsunami propagation
- To analyze the effect of possible future tsunamis and to develop a tsunami forecast model for Talcahuano (inside the Bay of Concepción).

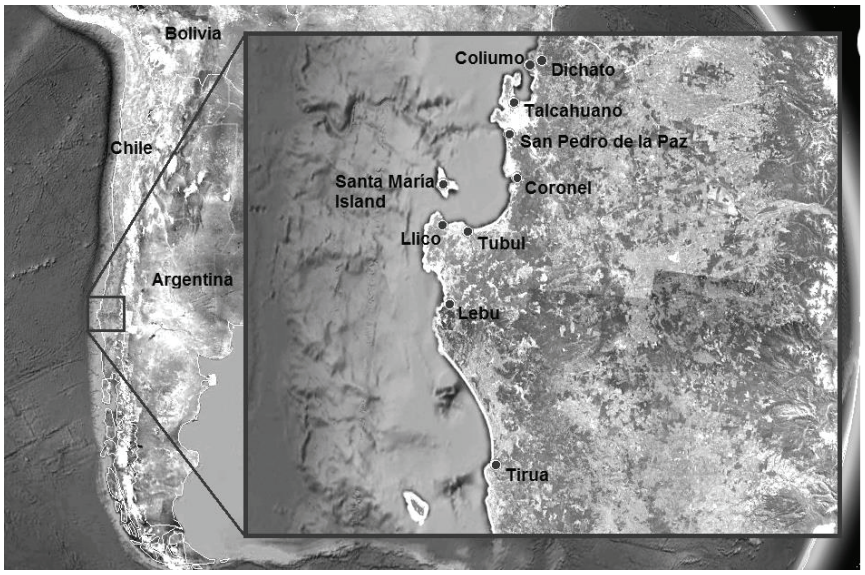

Figure 1. Location of the Biobio Region and some areas affected by the 2010 Chile tsunami

1.3. Organization of Dissertation

The present thesis has been organized in 5 chapters. A brief description of each chapter is given in the following paragraphs.

Chapter 1 presents a general introduction as well as the objectives and scope of the present research. The basic concepts related to generation and propagation of tsunamis are explained in Chapter 2. The tsunami interaction with the coast is also presented in this chapter. Chapter 3 analyzed the behavior of past tsunamis by means of numerical simulation. The spectral analysis is used to analyze the tsunami waveforms and tsunami energy at both the continental shelf and the Bay of Concepcion. In addition, the maximum tsunami inundation maps in the Gulf of Arauco are analyzed to identify the most and least affected areas. Then, typical seabed forms are analyzed in order to compare their influences in the results obtained from the analysis of past tsunamis behavior. The effect of possible future tsunamis is analyzed in chapter 4. In addition a tsunami forecast model for Talcahuano is also developed. Finally Chapter 5 presents the conclusions and presents possible venues for future research.

Chapter 2 Review on Physics of Tsunami

When tsunamis are studied, it is important to distinguish three main stages: the generation, propagation and interaction with the coast. Each of these stages can be studied by means of general principles of mechanics in continuous media with different mathematical approaches (Levin and Nosov, 2009). This chapter describes in a general manner these three stages, however, there is an emphasis in the topics which are more important for the present research.

2.1. Tsunami generation

Tsunamis can be generated by several sources, such as earthquakes, landslides, meteorites and meteorological conditions; however, the present section is focused on earthquake generated tsunamis only. To understand the earthquake-generated tsunami, it is necessary to understand the plate tectonic and the generation of earthquakes, hence the following paragraphs focus in that topic.

The Lithosphere, which is the external layer of the Earth, is broken into several segments or plates that are in motion to one another and change continually in shape and size (Condie, 1997). A schematic map representing the global tectonic is shown in Figure 2. The motion is due to new (oceanic) crust along divergent margins that generates subduction of the other side of the plate into the mantle. The overriding plate is stuck to the subducting plate, therefore, when the latter subducts beneath the mantle, the former gets squeezed. Due to this, the leading edge is dragged down, while an area behind bulges upward. This movement takes decades or centuries and slowly building up stress. An earthquake along a subduction zone happens when the leading edge of the overriding plate breaks and releases large amount of energy. At the same time the energy is released, the leading edge bulges upward and the area behind experiences subsidence. The previously mentioned process can be observed in Figure 3. An example of this phenomenon is the subduction zone of the Nazca plate beneath the South American Plate, where the leading edge is dragged down at a rate of 7-8 cm/year (Barrientos, 2007).

When one plate moves with respect to the other, the earthquake suddenly generates residual deformation of the seabed. This deformation is simultaneously accompanied by a formation at the sea surface of a perturbation similar to the deformation of the seabed (Levin and Nosov, 2009). The perturbation of the sea surface

has an extension similar to the fault area, which could reach hundred of kilometers. Due to the potential energy, the initial deformation of the sea surface falls down and oscillates until the equilibrium is reached. During this process, several tsunami waves are generated and propagated in redial direction from the tsunami source.

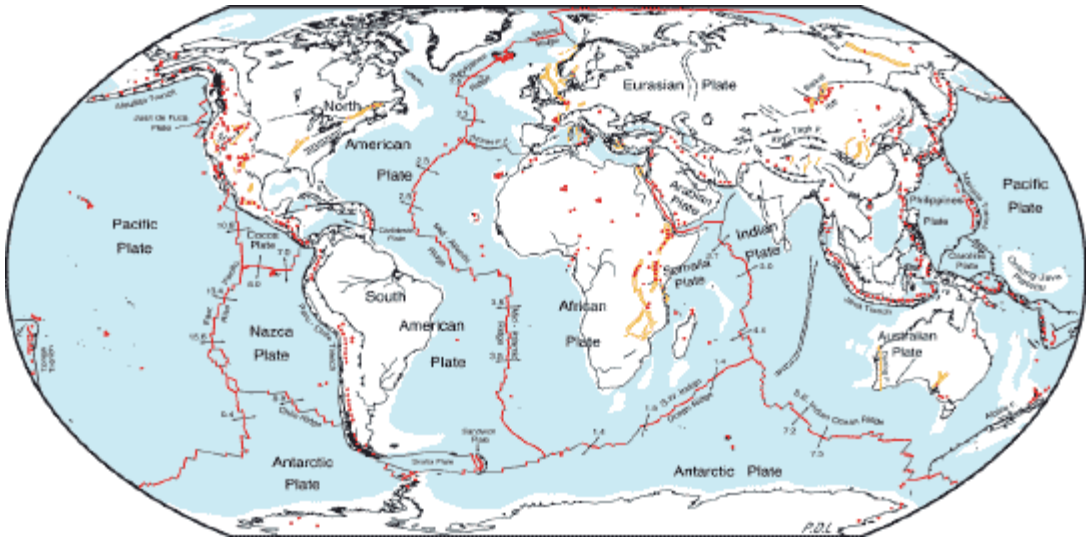

Figure 2. General map of the tectonic plates of the Earth. (Source NASA Observatory, website: http://earthobservatory.nasa.gov/Features/Tectonics/)

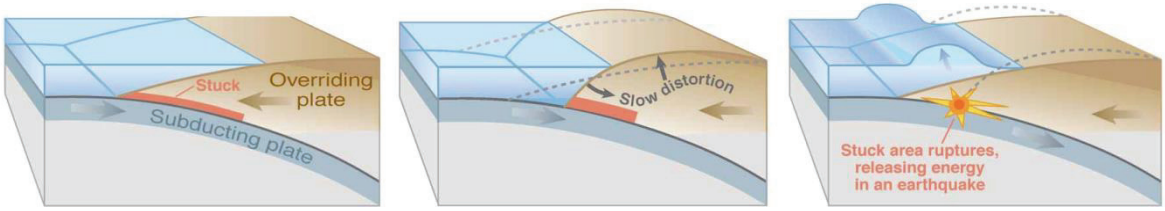

Figure 3. Generation of earthquake tsunami in subduction zones. (source: USGS website: http://pubs.usgs.gov/circ/c1187/)

2.2. Tsunami propagation

Similar to wind waves, tsunami waves experience transformation during tsunami propagation, namely, refraction, diffraction and shoaling. During the propagation the tsunami could experience a decrease in tsunami wave height due to energy losses caused by bottom friction and viscosity, however, this effect is only important for distance larger than 1000 km (Murata et al., 2010). In addition, the decrease in wave height could be also due to radial dispersion. Nevertheless, most of tsunamis are generated by long subduction faults, with a length which is 3 to 10 times the width, subsequently, the decrease of the wave height is not significant. Since tsunamis have

large wave length with respect to the water depth, the tsunami propagation could be analyzed as waves in shallow water (Murata et al., 2010), therefore, the wave celerity depends only on the water depth as given in equation (1), in which g is the acceleration of gravity and h is the water depth.

$$c = \sqrt{gh} \tag{1}$$

The shoaling effect could be defined as the increase of tsunami wave height due to decrease in water depth. This phenomenon is due to the fact that the energy flux remains constant, and the kinetic energy decreases as the water depth decreases, subsequently, the potential energy increases (Kundu, 2007).

The tsunami diffraction occurs when the energy flux is interrupted due to the presence of islands, inlets, artificial structures such as breakwaters or abrupt changes in bathymetry along the tsunami propagation direction, thus the wave moving through the opening fills the available area behind the obstacle. As the tsunami wave front enters a narrow passage from the open sea, dispersion process moves energy from the initially high wave crest sideways thus the wave height decreases. Therefore, the diffraction effect could reduce the tsunami impact in areas behind the obstacles. The wave diffraction is shown in Figure 4.

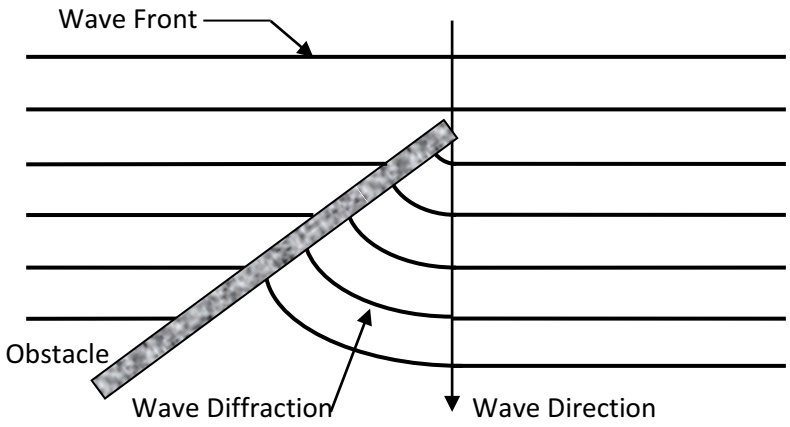

Figure 4. Diffraction of waves fronts due to the presence of an obstacle.

The refraction is a change in tsunami wave direction due to an oblique incidence of the wave front in a sloping bottom. The difference in water depth causes the wave front to rotate toward shallower water. Wave refraction can generate energy concentration areas such as peninsulas and energy attenuation in open areas such as bays, depending

of the bathymetry. However, the latter could also be affected by reflected waves. Since the tsunami wave has large wave length and relative low wave height, the tsunami wave could not break as wind waves does and be reflected (Murata et al., 2010). Reflected waves can propagate to another point of the bay in which the first tsunami wave already arrived, giving the impression of being a second or third tsunami wave. This phenomenon is represented in Figure 5.

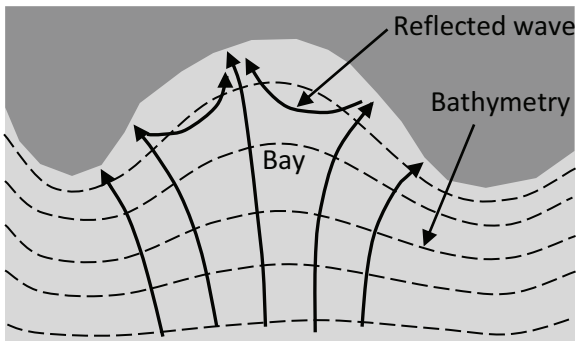

Figure 5. Wave refraction and reflection of tsunami waves in bays.

Tsunami wave reflection can also occur over abrupt changes in bathymetry, such as a large change in water depth over a distance much smaller than the wave length. This kind of changes can be represented as a step (Levin and Nosov, 2009), as seen in Figure 6-(a). Part of the incident wave is transmitted and part is reflected. The transmition coefficient, T, and the reflected coefficient, R, can be computed as a function of the water depth before and after the step, as given in equations (2) and (3) (Levin and Nosov, 2009). Figure 6-(b) shows the variation of both coefficients as a function of the water depth radio H_1/H_2. It is seen that the reflected wave is always smaller than the incident wave, while the transmitted waves increase in height, however, it is never larger than twice the incident wave.

$$R = \frac{\sqrt{H_1/H_2} - 1}{\sqrt{H_1/H_2} + 1} \tag{2}$$

$$T = \frac{2\sqrt{H_1/H_2}}{\sqrt{H_1/H_2} + 1} \tag{3}$$

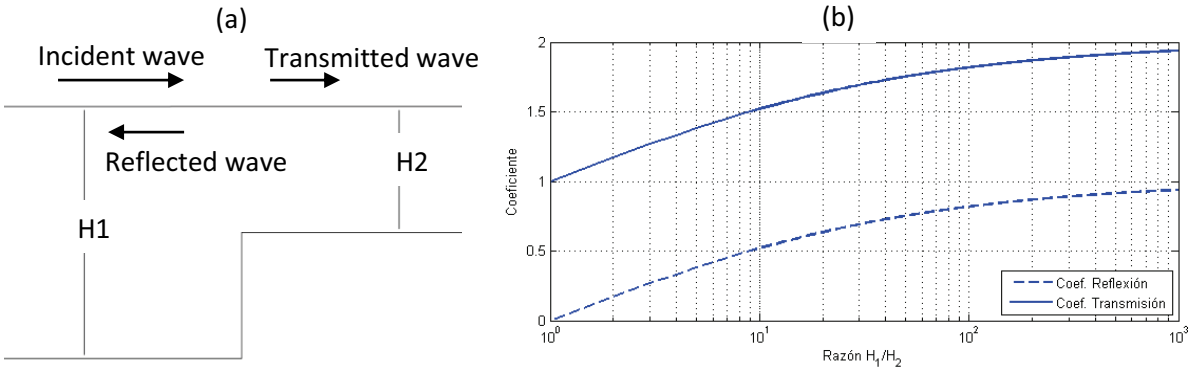

Figure 6. (a) Transmitted and reflected waves over a step. (b) Variation of the transmitted and reflected coefficientes as a function of H_1/H_2 over a step.

Tsunami waves approaching a step in a diagonal direction is analyzed in the work of Mofjeld et al. (2000). They applied the Snell law to compute the transmitted wave as a function of the angle of incidence and the ratio H_1/H_2, as given in equation (4). From this analysis it is found that a transmitted wave changes direction to be more perpendicular to the step when the wave propagates from deep water to shallower water, as seen in Figure 7-(a). Mofjeld et al. (2000) also analyzed the influence of the critical angle of incidence, due to the fact that this angle is important in defining whether the tsunami wave is transmitted over the step or fully reflected. The proposed expression is given in equation (5). Figure 7-(b) shows how the critical angle changes as a function of the ratio H_1/H_2. It is seen that the critical angle decreases rapidly as the ratio increases, which means that the larger the difference in water depth at the step, the smaller the maximum critical angle for the wave being transmitted, otherwise, the wave would be fully reflected. As an example, if the angle of incidence is larger than the critical one, a tsunami wave approaching a submarine canyon could experience reflection at the canyon walls and being propagated as trapped wave to the shore.

$$\varphi_1 = \arcsin\left(\varphi_0 \sqrt{\frac{H_1}{H_2}}\right) \tag{4}$$

$$\varphi_{0\_Crit} = \arcsin\left(\sqrt{\frac{H_2}{H_1}}\right) \tag{5}$$

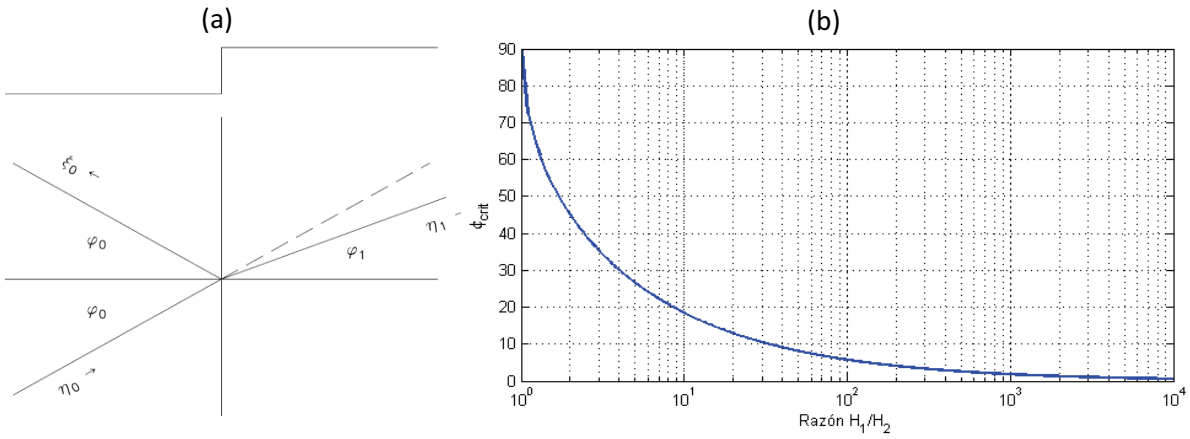

Figure 7. (a) Direction of reflected (φ_0) and transmitted (φ_1) tsunami wave over a step with oblique incident angle. (Mofjeld et al, 2000). (b) Variation of the critial angle of incidence as a function of the ratio H_1/H_2

Other important effect is tsunami resonance, which is an amplification of tsunami inside semi-enclosed basins. This phenomenon occurs when the tsunami period is close to the natural period of the embayment (Murata et al., 2010). In a similar manner, tsunami resonance could take place over continental shelf (Yamazaki and Cheung, 2011). Shelf resonance can generate edges waves that travel trapped along the continental shelf.

2.3. Tsunami interaction with the coast

When a tsunami wave approaches the coast the bathymetry influence tsunami behavior and refraction, diffraction and reflection phenomena could cause both focusing and de-focusing of tsunami energy. In addition, the shoaling effect is more evident, and the tsunami wave height increases from a meter to several meters. Therefore, the tsunami behavior would be highly unpredictable in the coast due to the influence of bathymetry as well as the topography. Similar to wind waves, the tsunami wave breaks when the wave height reaches certain value, however, due to the wave length, the tsunami behavior would be quite different. Mainly two kinds of wave breaking have been indentified based on past observations. The first kind corresponds to a gradual rise of water and fall of water with no water breaking, as it has been observed in steep coasts and long tsunami wave lengths. The second case takes place in milder sloping beaches, thus the tsunami wave breaks offshore and it gives formation of a tsunami bore (Yeh et al., 2005). In addition, another phenomenon can be observed in very shallow coasts where a gently seabed slope continues over long distance, this phenomenon is called solition fission, and take place due to nonlinearity and dispersion effects (Murata et al.,

2010). Once of the tsunami reaches the coast, part of the energy is reflected and dissipated, however, important part would inundate coastal areas with high amount of energy.

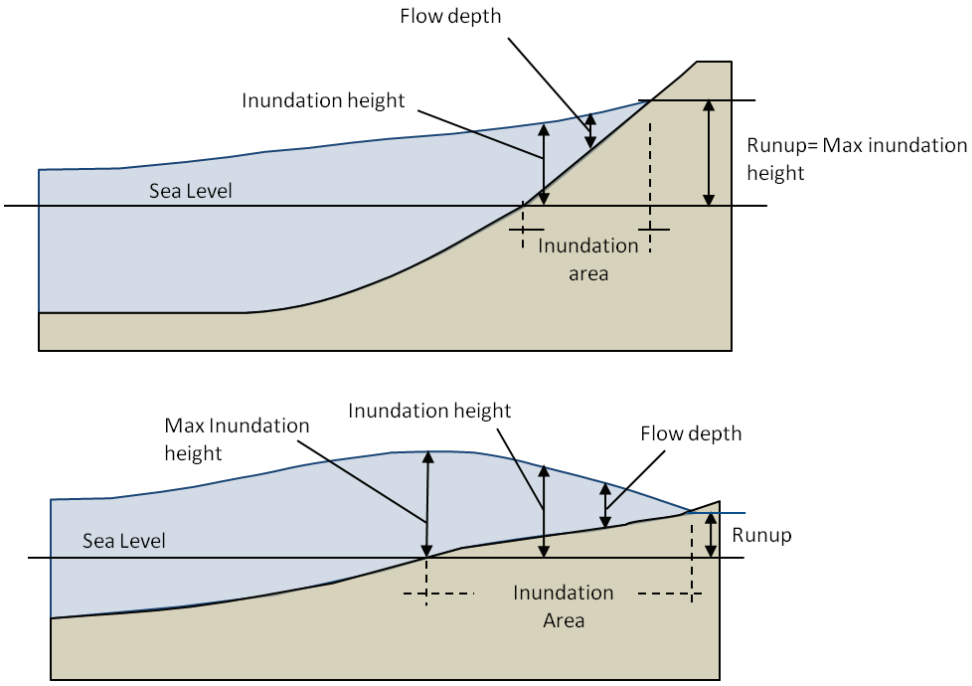

Figure 8. Definition of basic concepts in tsunami inundation for two different types of sloping beaches.

Figure 8, shows the definition of basic terms used in tsunami inundation process. Most of them are defined in UNESCO/IOC (2009). The inundation area corresponds to the tsunami horizontal penetration inland, and it is bounded by the shoreline and the inundation line. The runup is one of the most important concepts, and it is defined as the difference between the ground elevation of inundation line and the sea level at the time of the tsunami. While the Inundation height is the difference between the sea surface and sea level at the time of inundation, subsequently, it changes along the inundation area. Moreover, the runup does not always coincide with the maximum inundation height, as seen in Figure 8. In gently beaches, the maximum inundation height is larger than the runup and it takes place close to or at the coastline, while in steep beaches these variables coincide and could reach high values. The flow depth is defined as the difference between the ground surface elevation and the sea surface during inundation. It also changes along the inundation area. The flow depth is important in determining tsunami damage on properties and individuals.

During the inundation, the tsunami can cause several effects on coastal areas, such as erosion or sand sedimentation along the shore. In addition, coastal facilities can be

greatly damaged due to the tsunami flow. Figure 9 and Figure 10 show effects of the 2010 and 2011 tsunamis in Chile and Japan, respectively. Some effects are the scour around structures, such as roads and coastal facilities, which is caused by the flow during tsunami reseed. In a similar manner, the tsunami-induced forces are able to destroy and remove not only wooden houses but also structures built on reinforced concrete.

Figure 9. Effects of 2010 Chile Tsunami on Biobio Region. Left: Scour at the coastal street at Dichato town. Right: Wooden house washed away by the tsunami and deposited over rocks at Tumbes, inside the Bay of Concepcion.

Figure 10. Effects of 2011 Japan Tsunami. Left: Scour in coastal facilities at Minami Sanriku. Right: Four-story building turned down at Onagawa.

Chapter 3 Behavior of Past Tsunamis

This chapter analyzes the behavior of past tsunamis which have been generated along Chilean coast and propagated to the Biobio Region. Three past tsunamis are selected thus tsunamis from northern, central and southern Chile are included. The analysis is made by means of numerical simulation and spectral analysis of the waveforms of the three selected events. Then, the local morphology of the seabed found at the Gulf of Arauco and the Bay of Concepcion is analyzed, thus the behavior of the past tsunamis can be explained. The main findings in this chapter have been published Aranguiz and Shibayama (2013) and Aranguiz et al (2013).

3.1. The last tsunamis which affected the Biobio Region

Several earthquakes over magnitude 7.5 have been generated in Chile. Figure 11 shows the relevant events since XVIII Century, including the last earthquake and tsunami in 2010, which caused significant inundation inside the Bay of Concepcion. It is possible to see that large events occurred in the XVIII Century as the ones in 1730, 1751 and 1764; However, the records of these event are not well detailed about the effects. The largest event in the XX Century corresponds to the 1960 Earthquake, which had a magnitude 9.5. This earthquake generated a destructive tsunami in Chile as well as in Hawaii and Japan. In addition, there are other three major events in 1906, 1922, and 1943, with estimated moment magnitudes of 8.4, 8.3, and 7.9, respectively (Soloviev and Go, 1975). Even though tidegauges in Hawaii and Japan recorded minimal sea level variation, there is no recorded data of significant variation inside the Bay of Concepcion. However, in the XIX Century there is one event in 1877 in northern Chile with an estimated moment magnitude 8.8. This event caused a large tsunami in northern Chile, and an inundation height of 3m was observed at Talcahuano (Soloviev and Go, 1975). Therefore, the last events which are analyzed in the present chapter are the tsunamis of 1877, 1960 and 2010. These events are colored in red in the Figure 11. It is important to take into account that the rupture zone of the 1877 earthquake has no relevant seismic activity since this event. There is only one event in 2007, which had a magnitude 7.7. Therefore the analysis of the 1877 event is important due to the fact that a similar event could take place in the near future (Chlieh et al., 2011), as it is discussed in next chapter.

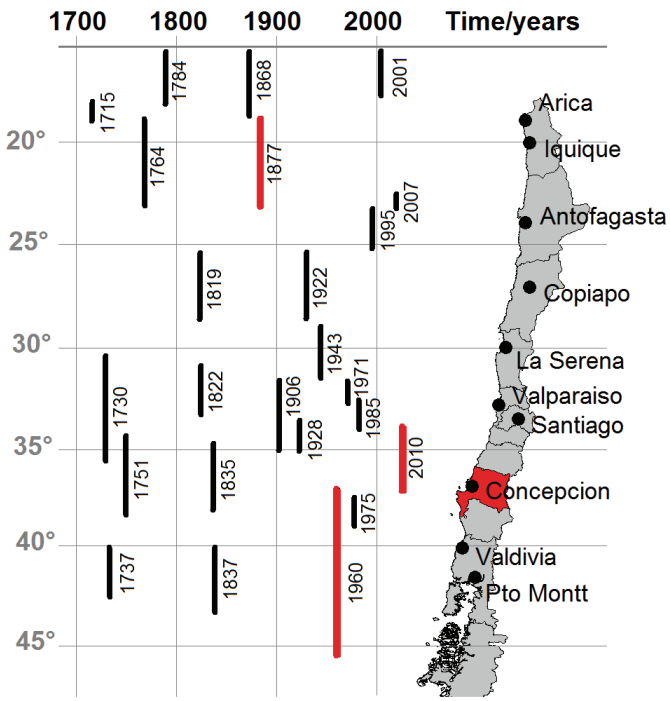

Figure 11. Relevant earthquakes generated in the subduction zone along the Chilean coast. Only events since XVIII Century are indicated. The events in red are the selected earthquakes for the numerical simulations. The Biobio Region is also indicated in a different color.

3.1.1. The 2010 Chile Earthquake and Tsunami

The 2010 earthquake had a moment magnitude 8.8 and a estimated rupture area of 450km by 150km, and it extended from Arauco Peninsula (37°S) in the south to Pichilemu (34°S) in the north with an average slip over 10m (Barrientos, 2010). The hypocenter (where the earthquake began) was found to be at 36.208°S, 72,963°W and at a depth of 32km (Delouis et al., 2011). The parameters such as the strike, dip and rake angles were found to be 15, 18 and 110°, respectively (Delouis et al., 2011). These parameters were estimated based on a series of joint inversions that the best fit to the seismological and geodetic datasets were found. The time needed by the rupture to propagate along the fault was estimated to be 110s (Barrientos, 2010). The earthquake was felt as far as Antofagasta in the north (23.5°S) and Puerto Montt in the south (41.5°S) with a total extension of 2,000km. Figure 12 shows total rupture area of the 2010 Chile earthquake and the aftershocks over M>4.7 (Barrientos, 2010). The contourlines in the left hand side of the Figure represent the total displacement between both the Nazca Plate and South American Plate, and the maximum slip were found to be 12-14m at the northern part of the rupture area. The blue dots represent the aftershocks, while the red one is the location of the epicenter. The right hand side shows the

aftershock activity as a function of the time during 100 days after the main shock. It is seen that most of the aftershocks are concentrated in the first 10 days. It is important to mention that this earthquake could have filled the large slip deficit accumulated during 175 years since the 1835 earthquake (Delouis et al., 2010). Therefore, the probability of a large earthquake in the same zone in the near future is rather low due to the fact that the plates move at a velocity of 6-7 cm/year (Barrientos, 2010).

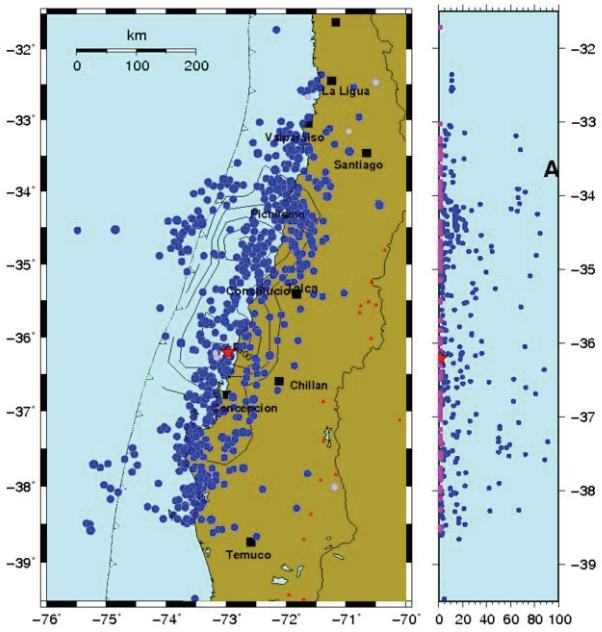

Figure 12. Rupture zone and afterchock of the 2010 Chile Earthquake. Left: Slip distribution and spatial distribution of aftershocks. Right: Temporal distribution of aftershocks (Barrientos, 2010)

The earthquake also generated a large tsunami which caused important damage along Chile's continental coast, in the Juan Fernández Archipelago, and Easter Island. The casualties were calculated to be 521, which includes victim of both the earthquake and tsunami (Fritz et al., 2011). The casualties due to the tsunami only accounts for 124 concentrated in the coastal regions of Maule (69) and Biobío (33), however, victims were also found at Mocha Island (4) and Robinson Crusoe Island (18) (Fritz et al., 2011). The latter is important to be mentioned due to the fact that it is located 600km NW from the 2010 earthquake rupture area, therefore, the quake was not felt and victims were not aware of the tsunami. Moreover, SHOA informed ONEMI that the sea level was normal at 4:13 (local time) and then canceled the tsunami warning at 4:49. At that time, two tsunami waves have already arrived to Robinson Crusoe Island and the third wave was arriving to Constitucion, as reported by the official investigation carried out by the Investigation Police (PDI for its name in Spanish). (http://papeldigital.info/lt/2013/02/07/01/paginas/004.pdf).

After the 2010 Chile tsunami, the author joint the field survey Team from Waseda University. This team was leaded by Professor Tomoya Shibayama. The surveys took place from April 3rd to 8th of 2010 covering mainly the Biobio Region. The survey teams documented tsunami runup, flow depth, inundation height and eyewitnesses interviews (Mikami et al., 2011). Figure 13 shows pictures with typical tsunami traces found during the field survey, such as seaweed in a tree at Coliumo, a water mark in a roof at Dichato and brown vegetation due to seawater at Tirua.

The field survey data were corrected by the tide at the moment of maximum inundation. A significant variation of tsunami impact was observed along the Biobio Region. The maximum inundation height was measured at Coliumo, with 8m, while the maximum runup was 20m at Tirua and 18m at Llico in the southern shore of the Gulf of Arauco. Inside the Bay of Concepcion, an inundation height of 5.4m and 6.4m in Penco and Talcahuano were measured, respectively. A more complete field survey was carried out by Fritz et al. (2011). This work included the Maule Region as well as the Robinson Crusoe and Eastern Islands. It was measured a localized runup of 29m at Constitución, and 20m at Tirua. Variable runup heights within a 5-15m range were observed between Constitución and Punta Morguilla some 300km south. In few significant cases the runup decreased below 5m near Cobquecura (the epicentral area) and the east coast inside the Bay of Concepción and the Gulf of Arauco (Fritz et al., 2011). For example, a runup of 3.7m was measured at Tomé and 3.0m at Colcura. In addition, seawater surged hundred meters into rivers in Coliumo, Lebu, and Tirua (Vargas et al, 2011). However, field surveys carried out by the author in April 2010 showed that no inundation was recorded at the 2km wide Biobio River and the inundation height was less than 2m along the coast of San Pedro de la Paz, which also coincides with the observations reported by other researchers (see for example Quezada et at. (2010) and Fritz et al. (2011)).

Figure 14 shows representative inundation heights and runup obtained from field survays along the Biobio Region. The figure also shows the bathymetry thus the Biobío submarine canyon can be observed. From this Figure, it is possible to see that large runups were measured at the southern shore of the Gulf of Arauco, with 8.4 and 13.4m measured in Tubul and Llico, respectively (Fritz et al., 2011). In a similar manner, the southern shore of the Bay of Concepcion experiences inundation heights of 6.7m in Talcahuano and 6.5m in Penco (Fritz et al., 2011), which are in good agreement with the measurement of the Waseda Team Survey. The low runup in the eastern shore of the

Gulf of Arauco as well as the large runup at the southern shore of the Bay of Concepcion will be analyzed in the following sections

Figure 13. Tsunami traces found during field survey after 2010 Chile tsunami in the Biobio Region. (a)Seaweed in a tree at Coliumo, (b) Water mark in the roof of a house at Dichato (c) Brown vegetation due to large runup at Tirua.

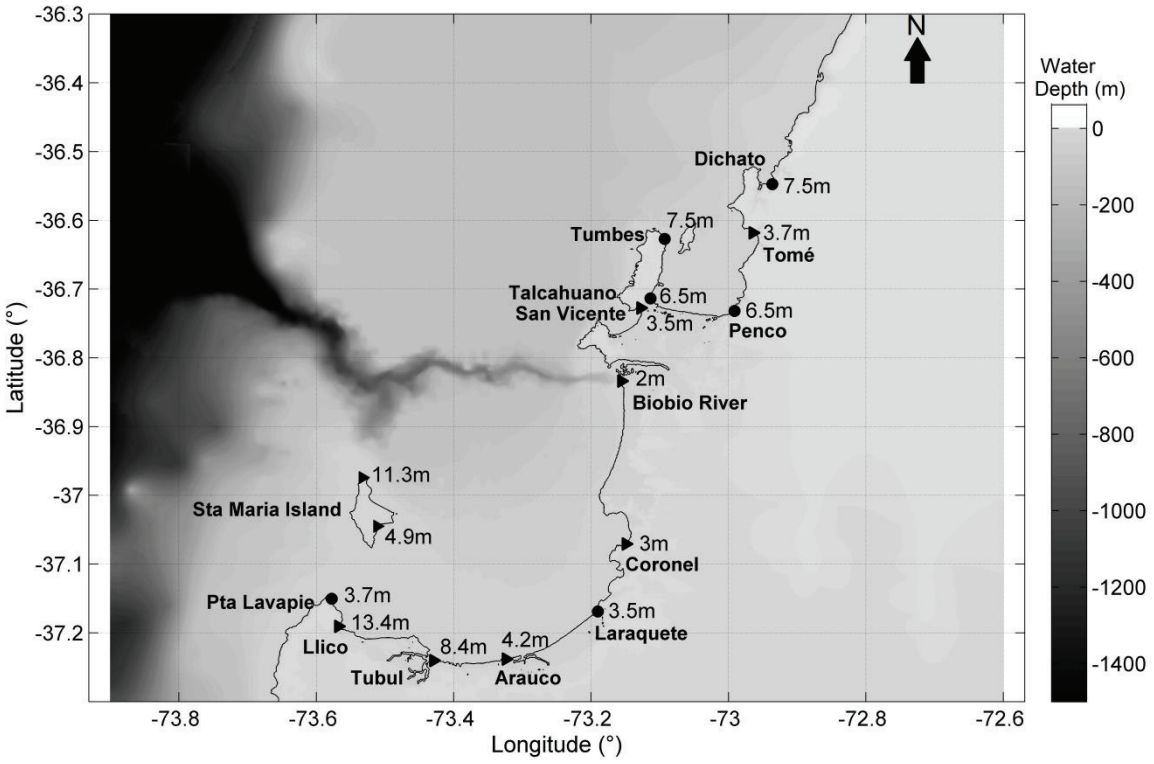

Figure 14. Representative results of tsunami field survey in the Biobio Region. Circles represent tsunami inundation heights, and triangles are the runup (Mikami et al., 2011, Fritz et al., 2011)

3.1.2. The 1877 Iquique tsunami

The 1877 earthquake and tsunami affected Chile, Peru and many coastal areas around the Pacific Ocean. The rupture zone would have been extended for approximately 500km, from 50km south of Arica (18,45°S) to 50km north of Antofagasta (23,65°S) (Madariaga, 1998). There were no instrumental records in Chile during the 1877 Iquique tsunami, while some tsunami observation can be found in Soloviev and Go (1975) and Vidal-Gormaz (1878). The 1877 Iquique occurred at 20:20 local time on May 9, and the resulting tsunami was noted as sea level rise at Iquique 20-30min later during diurnal half tide. An unusual movement of water was observed at 23:00 on May 9 at Valparaiso with approximate 1m maximum amplitude. The flood and ebb tides lasted 15 minutes during the next two days (Soloviev and Go, 1975). The water began to slowly recede from Talcahuano at 23:00-24:00 on May 9 (3.5- 4.5 hours after the earthquake), and the sea level dropped 1.2m below the regular low tide mark, i.e 1.7-1.8m below mean sea level at 0:30 on May 10. At about 2:30 on May 10, the water rose at Talcahuano 3m above the usual level. Tsunami inundated the port area, and destroyed and washed out the roadbed of the railway. The rise in sea level was

followed by a drop of similar magnitude (>2m). The sea level oscillations continued, but were less noticeable (Soloviev and Go, 1975). The oscillation in sea level began at 0:00 on May 10 at Tome, with a 70-cm sea level rise, while it was observed at 500m from the river mouth. A 75-cm and 60-cm sea level rise are also noted at 2:00 and 6:00 on May 10, respectively. The city of Pisco (13.71S, 76.20W), in Perú, experienced slight damage due to the tsunami, and a maximum inundation of 3m was reported (Okal et al., 2006; Soloviev & Go, 1975). A strong wave occurred at 1:45, and a second large wave took place at 3:00 in phase with the diurnal flood tide (Soloviev & Go, 1975).

A classical tidal harmonic analysis was applied at Valparaiso and Talcahuano using T_TIDE (Pawlowicz, 2002) in order to compare the observed inundation height in the results from the numerical simulations. The tidal prediction was adjusted using two tide gauge records at Iquique (20.20°S, 70.16°W) and Constitucion (35.53°S, 72.42°W) during the event on May 9 and 10 of 1877. Tide records at Iquique and Constitucion were obtained from the Sea Level Station Monitoring Facilities (http://www.ioc-sealevelmonitoring.org/). Soloviev and Go (1975) described that "at Iquique, the first rise of water was noted 20-30 minutes after the earthquake (20:40-20:50 local time) during the diurnal half tide". Vidal-Gormaz (1878) also describes that the high tide at Constitucion should have taken place at 11:00 local time on May 10th ("*Un tercer flujo, bastante grande, se verificó a las 5h A.M. del 10, en circunstancias que la pleamar de ese día debía tener lugar a las 11 de la mañana*"). Since the current tidal record and prediction use UTC time, the date and time must be converted to local time to be compared with observations at the time of the 1877 tsunami. However, the first official time in Chile was set in 1894 (http://www.horaoficial.cl/horaof.htm). Therefore, tidal prediction was adjusted using the local observations at Iquique and Constitucion, and the adjustment of UTC-2 results in a good agreement with local observations. Figure 15 shows the tidal variation on May 9 and 10 of 1877 at Iquique and Consitucion. The black arrows show the earthquake origin time at Iquique and the high tide at Constitucion, respectively.

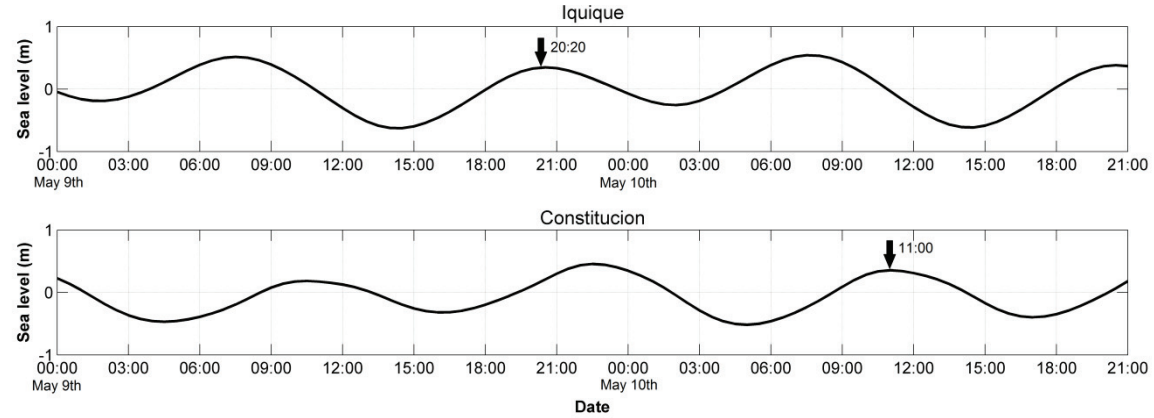

Figure 15. Tidal variation on May 9-10th of 1877 at Iquique and Constitucion.

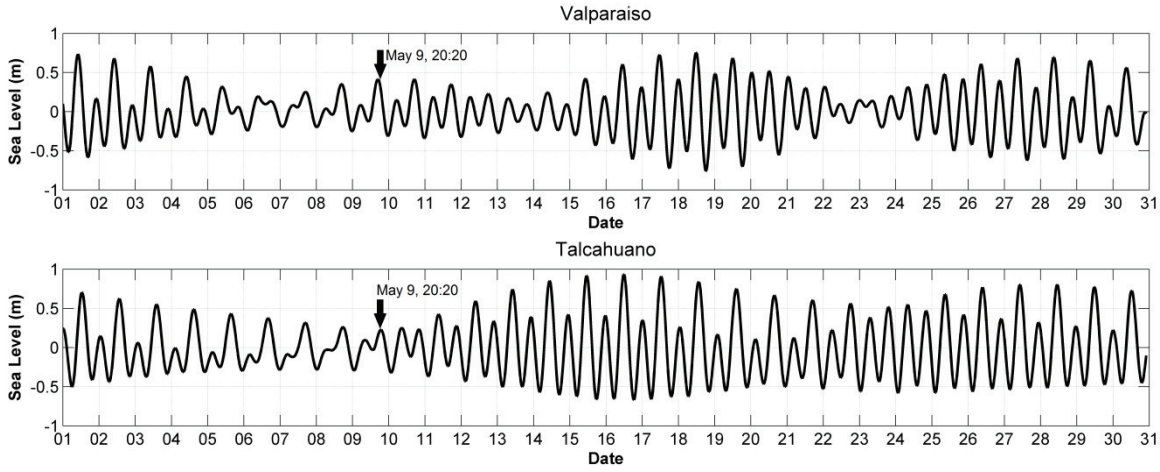

Figure 16. Predicted tides at Valparaiso and Talcahuano during May 1877.

The same analysis can be carried out for Talcahuano and Valparaiso in order to estimate the tidal variation during the 1877 tsunami. The adjusted results are shown in Figure 16 . The most important feature here is that the tsunami occurred during the neap tides, which corresponds to the low high tide with a tidal range of ± 50 cm. In addition, the largest wave hit Talcahuano at 2:30 on May 10 (Soloviev and Go, 1975) during the low tide (-0.3m). Therefore, the maximum sea surface elevation from the numerical model at Talcahuano (set to the mean water level) must consider the low tide at the moment of maximum inundation when compared with local observation.

3.1.3. The 1960 Valdivia earthquake and tsunami

On May 22nd of 1960 at 15:11 local time (19:11 UTC) the largest earthquake ever recorded took place in southern Chile. The earthquake had a surface-wave magnitude 8.5 and a moment magnitude 9.5 (Barrientos and Ward, 1990). However, the 1960

earthquake is defined as a sequence of several moderate and strong shocks with three major earthquakes within 33hrs, thus the first major shock took place on May 21st at 10:02 UTC with a magnitude 8.3, the second shock occurred on May 22nd at 18:55 UTC with magnitude 7.8, while the main shock consisted of two subevents of magnitude 8.3 at 19:10 and 19:11 UTC (Duda, 1963). The duration of the main shock is estimated to be 5min (www2.udec.cl/gema/Terr_sigloXX/21y22_5_1960.html). The rupture area of this event extended from Arauco Peninsula in the north (37°S) to Taitao Peninsula in the south (46°S) and significant changes in land were observed along 1000 km long and 200 km wide (Barrientos and Ward, 1990).

The 1960 event generated a large tsunami that affected the entire Pacific Ocean, including Hawaii, Japan and New Zeeland. As a matter of fact, an inundation height larger than 3 m was measured in Hawaii and 4.2 m and 4.9 m in the Japanese cities of Onagawa and Ofunato, respectively (Takahashi, 1961). Some values of Inundation heights measured in Chile are listed in Table 1. Similar to the 2010 Chile tsunami, it is possible to see that the 1960 event also caused diverse effects along the Chilean Coast. In fact, Dichato experienced large inundation height similar to 2010 event, however, the southern shore of the Bay of Concepcion (Penco and Talcahuano) had inundation heights of 3 m. The eastern shore of the Gulf of Arauco also experienced low inundation heights, as seen in Coronel and Lota.

Table 1. Inundation heights along Chilean Coast due to 1960 tsunami (Takahashi, 1961)

Locality	Latitude	Inundation height (m)
Constitucion	**35.33°S**	2.4
Dichato Bay	**36.54°S**	3.5~7
Tome	**36.62°S**	2.0
Penco	**36.73°S**	2.0~2.5
Talcahuano	**36.71°**	3.0
Coronel	**37.03°S**	2.0
Lota	**37.10°S**	2.0~3.0
Tirua	**38.34°S**	4.0~5.0
Mocha Island	**38.57°S**	20~25
Corral	**39.89°S**	8.8~10
Ancud	**41.87°S**	6.0~8.0

Figure 17 shows the tidal variation at Talcahuano during May of 1960. The vertical blue lines indicate the 16:00 and 20:00 local time on May 22nd, which correspond to the period where the maximum tsunami amplitudes were recorded at Talcahuano. It is possible to see that during this time period, the tide level changed from -0.3m to +0.4m only. Therefore, the analysis in the following sections did not consider the tidal variation, and the numerical simulation assumed the mean water level.

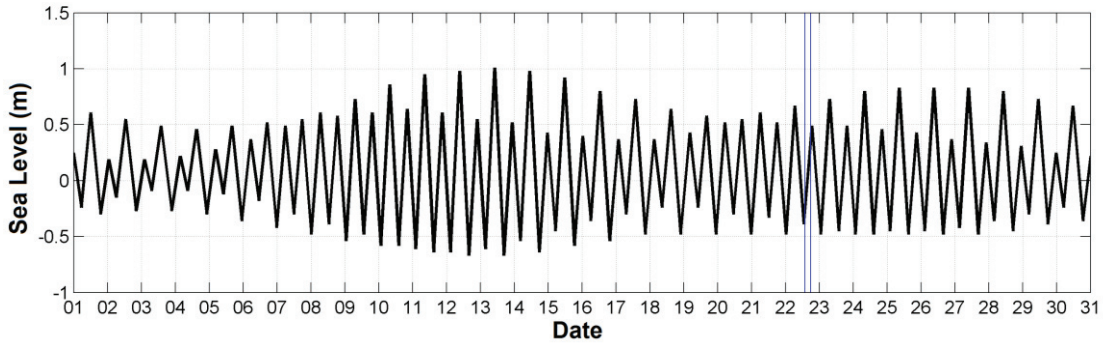

Figure 17. Tidal prediction at Talcahuano during May 1960 (Hydrographic and Oceanographic Service of the Chilean Navy, SHOA)

3.2.Numerical Simulation of Past Tsunamis

3.2.1. Numerical model and model set up

The present study utilizes the dispersive wave model NEOWAVE (Non-hydrostatic Evolution of Ocean WAVEs) for tsunami numerical analysis (Yamazaki et al., 2009, 2011). NEOWAVE is the two-dimensional, depth-integrated model describes dispersive waves though the non-hydrostatic pressure. The semi-implicit, staggered finite difference model implements in a two-way nested-grids in spherical coordinate system. The initial condition for tsunami modeling in this study is the static sea surface deformation, which is assumed to be identical to vertical component of the sea floor displacement. The planar fault model of Okada (1985) provides seafloor displacement from the fault parameters given in Figure 18. (Xo,Yo) are the x and y coordinates of the down-left corner of the rupture area, d_c is the focal depth, W is the width of the rupture area, L is the length of the rupture area, D is the slip of the fault, and θ, δ and λ are the strike, rake and dip angles, respectively.

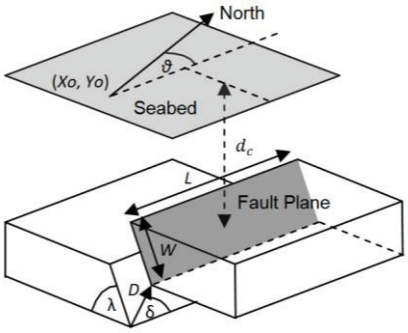

Figure 18. Seismic parameters used in the Okada (1985) formulation to generate the tsunami initial condition.

The model uses a Manning's coefficient n = 0.025 describing the ocean bottom. The computation covers 10 hours of elapsed time with output time intervals of 1min. Four levels of nested grids is setup to model the tsunami from generation to the study area. The grid 1 is the southeast Pacific Ocean at 2-arcmin (~3,600m) to cover the tsunami generation. Two different sizes of grids 1 were defined according to the scenario. The first one covers latitudes from 12° S to 41°S, thus the 1877 tsunami can be generated and propagated. This grid was also used for the 2010 event. The second grid is defined in order to analyze the 1960 earthquake and tsunami, therefore, it covers latitudes 32°S to 48°S. Both grids are shown in Figure 19. The Figure also shows the 9 tide gauges used to analyze the tsunami behavior. Tide gauges 1 to 6 are used in the case of the 1877 tsunami. Gauges 6 and 7 are used in the analysis of 2010 tsunami, while gauges 6, 8 and 9 were utilized in the 1960 event. The common gauge 6 is defined at the entrance of the Bay of Concepcion. The grid 2 at 30-arcsec (~900m) and the grid 3 at 6-arcsec (~180m) describe wave transformation over the continental shelf and slope along the Chilean coast as well as the Gulf of Arauco. The grid 4 at 1-arcsec (~30m) is used to model inundation and tide gauge at the Bay of Concepción. Grids 2, 3 and 4 are the same for modeling the three selected scenarios. The 3 grid are shown in Figure 20. The location of gauges 3, 5 and 9 can be appreciated in Figure 20(a), while gauge 6 can be better seen in Figure 20(b). 3 additional tide gauges were defined inside the Bay of Concepcion, namely Tome, Penco and Talcahuano, as seen in Figure 20(c). The grids 1 and 2 are generated from GEBCO 08, and the grids 3 and 4 are built from nautical charts and different topography sources. The topography of the higher resolution grids the Bay of Concepcion and the Eastern shore of the Gulf of Arauco, are obtained from LIDAR data with 2.5m resolution.

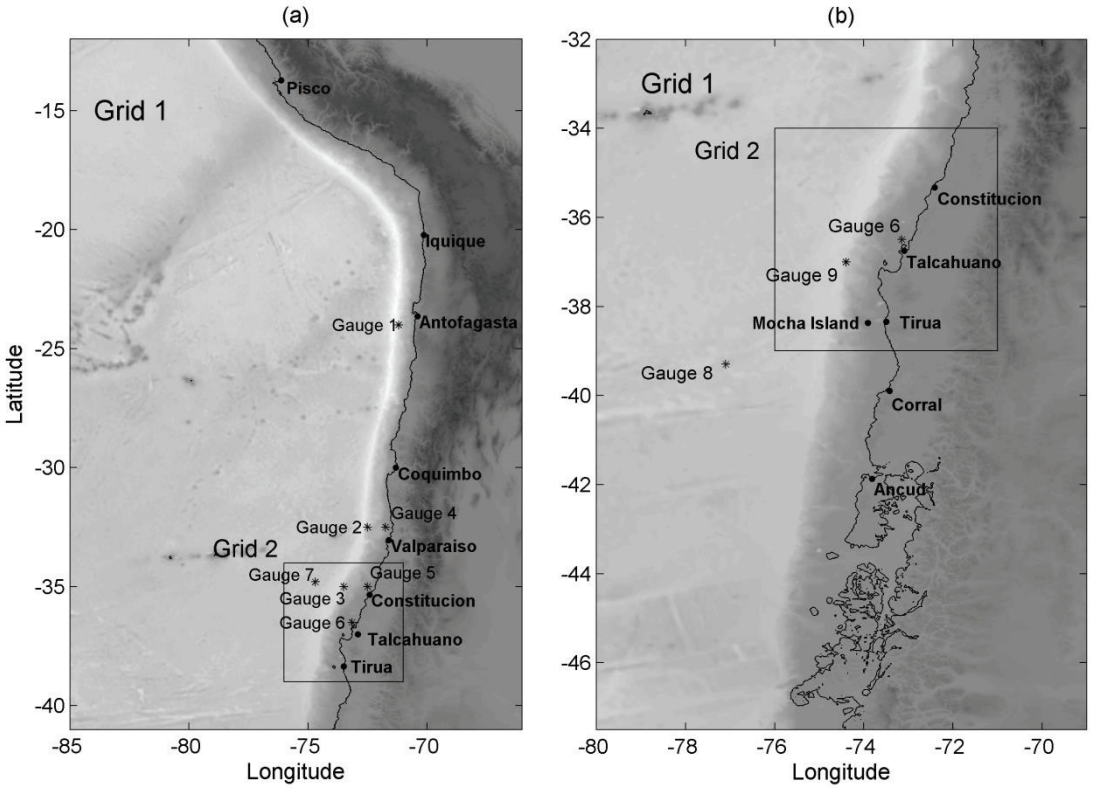

Figure 19. Grids of level 1 used in the numerical simulations. (a) Grid 1 used in simulation of both 2010 and 1877 events. (b) Grid 1 used for 1960 event. The tidegauges are indicated with asterisks in each grid.

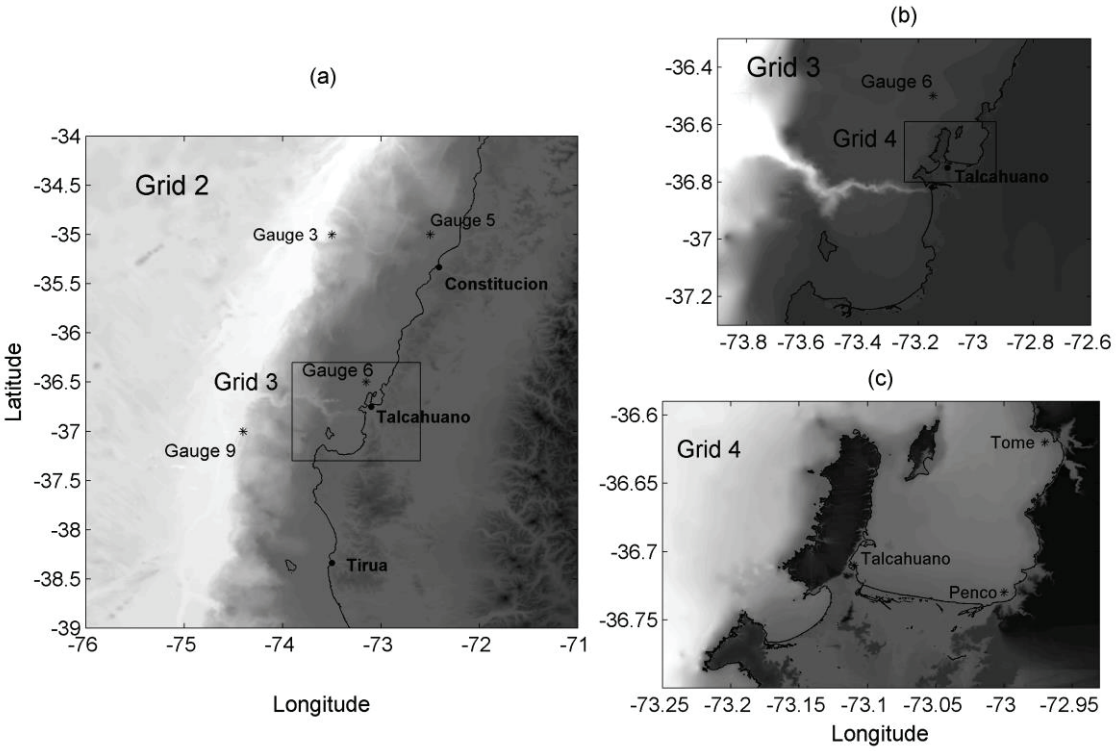

Figure 20. Common grid used in the numerical simulations. (a) Grids 2 with the locations of tide gauges 3, 5, 6 and. 9. (b) Grid 3 with the location of tidegauge 6 at the entrance of the Bay of Concepcion. (c) Grid 4, the tidegauges at Tome, Penco and Talcahuano are indicated.

3.2.2. Tsunami initial conditions

a. 2010 Concepcion tsunami.

Two fault models were tested in order to define the 2010 tsunami initial condition. The first one is a Uniform Fault Plane (UFP). The size of the rupture area and slip are obtained from Barrientos (2010), while the parameters such as strike, dip and rake angles are given by Delouis et al. (2010). The initial condition is built using the Okada (1985) formulation. The other tsunami source corresponds to the USGS Finite Fault Model (FFM). This fault model estimated the fault parameters and rupture sequence over a 540km by 200km region with 180 subfaults of 30km by 20km each (G. Hayes,http://earthquake.usgs.gov/earthquakes/eqinthenews/2010/us2010tfan/finite_fault.php, 2010). The initial sea surface deformation is built by means of superposition of the 180 subfaults, and each fault is calculated using the Okada (1985) formulation. The USGS finite fault model of the 2010 Chile tsunami has been validated with DART buoys by Yamazaki and Cheung (2011) using NEOWAVE. They considered two nested grids of 2 arcmin (4,000m) resolution and 0.5 arcmin (~1,000m) resolution. They analyzed the recorded data at buoys DART 32412, 51406, 32411 y 43412. The model reproduced the dominant processes and show good agreement of the amplitude, phase, and frequency content with the measurements.

Figure 21 shows waveforms at Talcahuano obtained with both UFP and FFM. In addition data from the Talcahuano tide gauge are plotted in the same Figure in order to compare simulated and recorded data. Even though the Talcahuano tide gauge collapsed with the second tsunami wave, it is possible to see that both models show similar results. However, the simulated tsunami waves after the tidegauge collapsed are in good agreement with observed tsunami waves reported later (Larrañaga, 2010). This result is also in good agreement with historical records of past tsunamis too, such as the events of 1657, 1730 and 1835, where the second tsunami wave was identified as the largest one (Soloviev and Go, 1975; Lomnitz, 1970, Gil, 1945). Since the Uniform Fault Planar model shows to have a larger first wave and a bit smaller second tsunami wave, the following analysis used the FFM only.

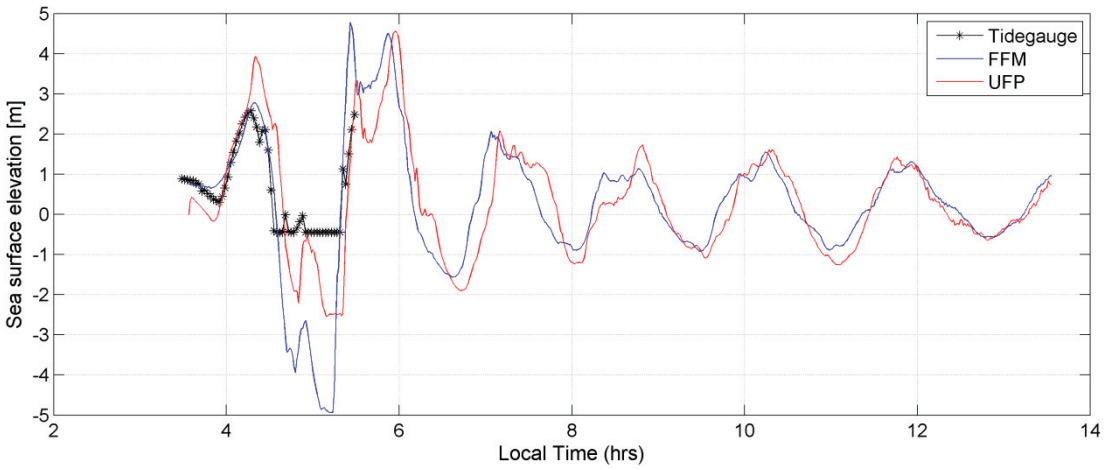

Figure 21. Waveforms at Talcahuano with two fault models, The measurements of Talcahuano tidegauge are also shown.

b. 1877 Iquique Tsunami

This section describes the fault models for the 1877 earthquake used in the present study. It is known that the fault orientation and focal depth often have significant effects on the tsunami modeling results. Therefore, sensitivity tests of these factors were conducted. For comparison purposes, all modeling results in this section have a tide level set to be mean water level. As the tide prediction at Talcahuano was low tide with 0.3m below MWL, the maximum tsunami amplitude must consider this effect in order to be compared with historical records. The validation of the tsunami source parameters were performed considering tsunami records in Talcahuano and Valparaiso at the southern side of the tsunami source, while the northern side included the city of Pisco, Perú, The nested grids of the latter were built from GEBCO data base only.

The seismic parameters of the Arica-Tocopilla source region can be estimated based on recent seismic activity. To do this, the focal mechanisms of the 1995 Antofagasta earthquake as well as the 2001 Arequipa earthquake were analyzed. From these focal mechanisms, it is possible to estimate the rupture and Wadati-Benioff planes of each earthquake (Aránguiz and Belmonte, 2012). In a similar manner, analysis of the focal mechanisms related to seismic activity between 1960 and 1995 in this region allows the estimation of seismic parameters (Belmonte, 1997, cited in Aránguiz and Belmonte, 2012). Based on the previous analysis, the 1877 Iquique earthquake ruptured an approximately 420km long and 130km wide fault with strike, dip and rake angles of $\varphi = 0°$, $\lambda = 19°$ and $\delta = 100°$, respectively (Aránguiz and Belmonte, 2012). The total seismic moment released is $M_0 = 2.1x10^{22}$J, equivalent to $M_w = 8.8$ with a slip of $D = 12$m.

i. Fault orientation effects on tsunami modeling

First, the effects of fault orientation and associated slip distribution using three fault models are examined. Model 1 uses the single fault and Model 2 uses three subfaults to better describe the Arica bend shown in Figure 22 and Table 1. The use of mutiple subfaults was demonstrated to give good results in modeling of the 2004 Indian Ocean tsunami (Grilli et al, 2007). Both Model 1 and Model 2 use the uniform slip of 12m. In addition, a Model 3 was considered, which utilizes the same subfaults of Model 2, but assign 8.5m, 17m, and 8.5m slip to Subfault 1, 2, and 3, respectively. All fault models assume constant focal depth of 30km and have the same total seismic moment equivalent to Mw=8,8 with $\mu = 3 \times 10^{10}$Pa.

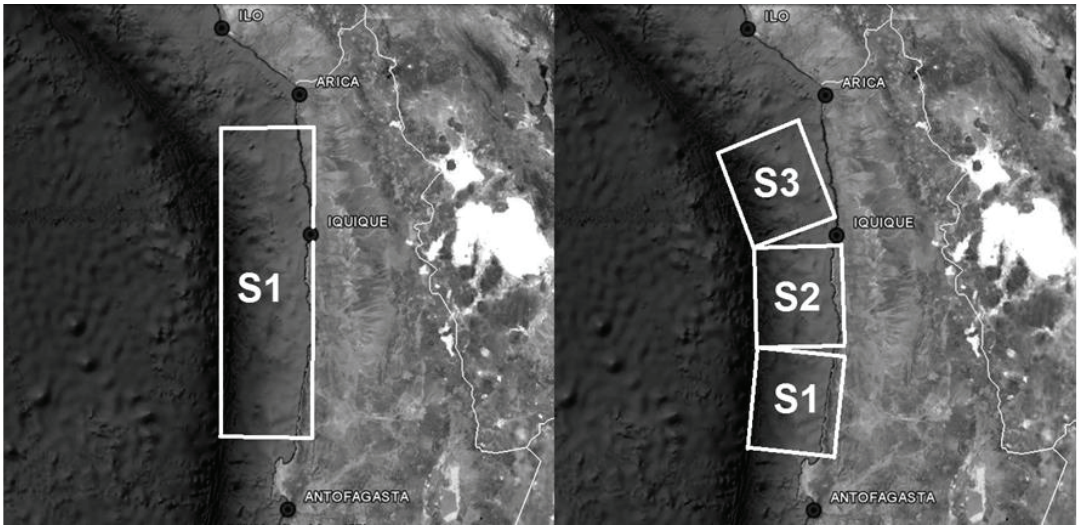

Figure 22. Location of the rupture segment S1 of the single fault (Model 1) and rupture segments S1-S3 of the multiple subfaults (Model 2 and 3) given in Table 2 for the 1877 Iquique earthquake

Table 2. Primary source parameters used for Okada's (1985) source segments S1-S3 corresponding to Model 1, 2 and 3 of the 1877 Iquique earthquake.

	Model 1	*Model 2 and 3*		
Parameter	*S1*	*S1*	*S2*	*S3*
X0 (long)	-71,31	-71,31	-71,19	-71,25
Y0 (Lat)	-22,89	-22,89	-21,66	-20,40
Focal depth (km)	30	30	30	30
Upper side depth (km)	8.8	8.8	8.8	8.8
$\boldsymbol{\phi}$ (deg)	0	5	355	335
$\boldsymbol{\lambda}$(deg)	19	19	19	19
$\boldsymbol{\delta}$ (deg)	100	100	90	70
L (km)	420	140	140	140
W (km)	130	130	130	130

Figure 23 shows the computed waveforms at Pisco, Valparaiso and Talcahuano obtained for the three fault models. The computed results from three fault models show very similar waveforms, thus the fault orientation and slip variation has minor influence on tsunami propagation, at least for the first 5 waves at Valparaiso and the whole 10 hours of elapsed time at Pisco and Talcahuano. In the case of Pisco, the maximum tsunami wave amplitude was computed to be 2.5m. Since numerical simulations considered mean sea level, and the inundation took place in phase with the diurnal flood tide (Soloviev and Go, 1975), it is possible to conclude that the computed results are in good agreement with tsunami records. Moreover, the Model 1 provides an envelope of the sea surface variation, which gives conservative values of maximum inundation height in Talcahuano. Therefore, the analysis of the rest of this paper utilizes a single fault model based on the Mode1 1.

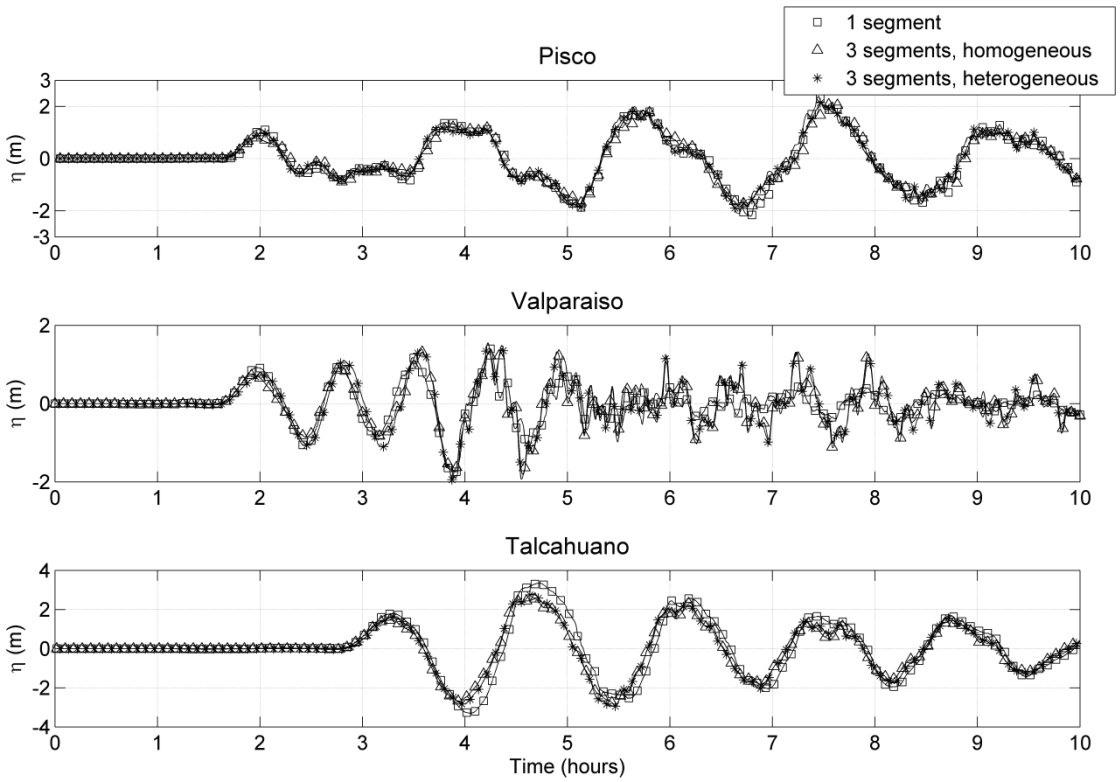

Figure 23. Computed waveforms at Pisco, Valparaiso and Talcahuano tide gauges for three different source models.

ii. Fault location effects on tsunami modeling

Numerical analysis in the previous section showed that the fault orientation has a minor effect of tsunami propagation toward both north and south of the tsunami source. In this section, the effect of the location of the PFM (Model 1) as a function of focal depth is analyzed. Table 2 shows adjusted parameters in Model 1 due to change of fault

location and depth used in this sensitivity test. The analysis is carried out for locations at the southern side of the tsunami source only, i.e. Valparaiso en Talcahuano.

Table 3. Location of tsunami sources for 6 different focal depths. The coordinates x_0 and y_0 indicate the down-left corner of each rupture segment.

Fault	x_0	y_0	*Focal depth(km)*	*Upper side depth (km)*
1	-71.14	-22.75	25	3.8
2	-71.00	-22.75	30	8.8
3	-70.87	-22.75	35	13.8
4	-70.73	-22.75	40	18.8
5	-70.59	-22.75	45	23.8
6	-70.45	-22.75	50	28.8

Figure 24 shows comparisons of computed waveforms at Valparaiso and Talcahuano with six different focal depths (or fault locations). The first four waves in the computed results with different depths at Valparaiso have similar waveforms. Especially the first two waves show very minor effect of the focal depth. The third and forth waves show increase of amplitude as the focal depth decreases. However, the maximum sea surface elevation shifts from the fourth wave for shallower earthquakes to the third wave for deeper earthquakes. The computed waveforms with different depth at Talcahuano tide gauge looks almost identical, so that over all the focal depth variation has almost no influence on computed waveform. On the other hand, the focal depth shows interesting effects on the maximum amplitude. The second wave amplitude is always largest in all computed results, and increases with increase of the focal depth up to 40km depth. But the computed amplitude at the second wave starts to decrease with further deep focal depth shown in computed results with depth of 45 and 50km.

Comparing the computed waveform at Talcahuano tide gauge with observation, the sea level starts rising around 3 hours elapsed time, then decreases and reached the minimum level 4 hours later (12:20 local time). In addition, the maximum sea surface elevation takes place always during the second tsunami wave. Therefore, the tsunami wave observed at 2:30 (6 hours and 10min after the earthquake) at Talcahuano (Soloviev and Go, 1975) would correspond to the third wave actually. Even though most of the observations imply a retreat of sea level prior to the first tsunami wave (Soloviev and Go, 1975), this behavior is not observed in the computed waveform. However, the tide gauges at Arica, Iquique and Antofagasta (located in the rupture zone

of 1877 earthquake) during the 2010 Chile tsunami in Central Chile indicate that the sea did not retreat prior to the first tsunami wave (Fritz et al., 2012). Therefore, it is possible to conclude that the first tsunami wave during 1877 tsunami was not clearly observed because of its low amplitude and the darkness, and people noticed the tsunami when water recede from the coast before the arrival of the second wave. As a matter of fact, the observation at Lota states how "the ocean advanced a little and then retreated far from shore" (Soloviev and Go, 1975), i.e. there was a first wave before the retreatment of the sea, which is in good agreement with the computed waveforms obtained for Valparaiso and Talcahuano.

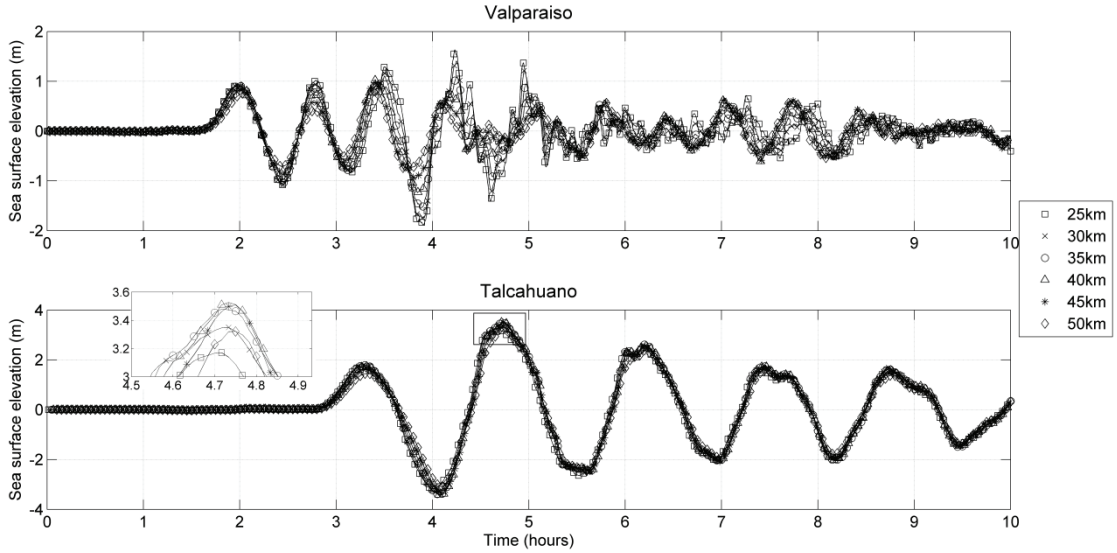

Figure 24. Computed waveforms at Valparaiso and Talcahuano tide gauges for 6 different focal depths.

The maximum tsunami amplitude at Valparaiso and Talcahuano corresponding to a focal depth of 30km were found to be 1.35 and 3.4m respectively, as seen in Figure 25. Since the numerical simulation considered the mean water level, the correction with the low tide of -0.3m gives tsunami amplitudes of 1.05 and 3.1m at Valparaiso and Talcahuano, respectively, which is in good agreement with the local observations. Deeper focal depths give lower tsunami amplitude at Valparaiso. In the case of Talcahuano, the tsunami amplitude increases as the focal depth increases up to 40km, and then decreases again. Therefore, model 1 with a focal depth of 30km is considered to be the best representation of the 1877 Iquique tsunami. Nevertheless, the tsunami behavior inside the Bay of Concepcion is further investigated in this chapter, due to the parabolic variation as a function of the focal depth.

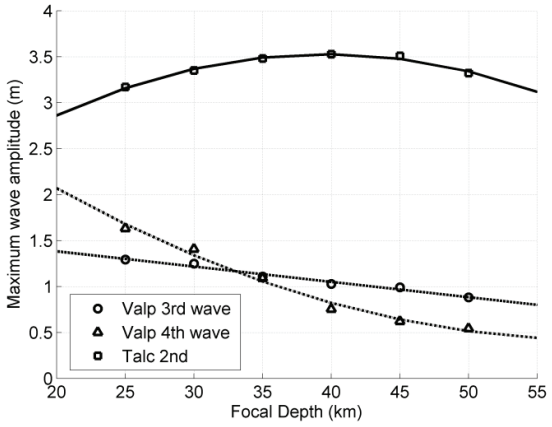

Figure 25. Maximum tsunami amplitude due to 1877 Iquique tsunami at Valparaiso and Talcahuano as a function of the focal depth.

c. 1960 Valdivia Tsunami

The source parameters of the 1960 earthquake have been proposed by several authors, see for example Kanamori and Cipar (1974), Cifuentes (1989) and Barrientos and Ward (1990). Numerical simulations of the 1960 tsunami have used Planar Fault Models (PFM) only. For example, Liu et al. (1995) simulated the 1960 tsunami in order to study the effect on Hawaii island. They used the homogeneous rupture model proposed by Kanamori and Cipar (1974). This model considered a rupture length of L=800km, a width of W=200km, a slip of D=24m and a focal depth of 53km. In a similar manner, Heinrich et al. (1996) simulated the same event in order to analyze the tsunami impact on French Polynesia. They studied 6 uniform tsunami sources including the one proposed by Kanamori and Cipar (1974) plus 5 possible combinations given by Cifuentes (1989). The model proposed by Cifuentes (1989) with a length L=920km, a width of W=120km and a slip of 32m gave the best results in terms of arrival time and maximum amplitudes. With regards to near-field tsunamis, Lagos and Gutiérrez (2005) reconstructed the maximum inundation by the 1960 tsunami in Maullín (41.62°S, 73.6°W). They used UPF model proposed by Barrientos and Ward (1990).

Barrientos and Ward (1990) proposed two different models, the first one is a uniform plane fault or planar fault model (PFM) and the second one is a variable slip planar model of finite fault model (FFM). The PFM considered a rupture size of L=850 m, W=130 m and an average slip of 17 m, while the other parameters are a strike, dip and rake angles of 7°, 20° and 105°, respectively. The FFM considered 600 subfaults in 900km long and 150km wide. The maximum slip exceeded 40 m at the northern part of the earthquake source. In both cases, vertical deformations and seismic data were used

to calibrate the models. The uplift predicted by both the PFM and FFM models are in good agreement with field measurements.

The present section analyzed both rupture models proposed by Barrientos and Ward (1990). Since the 1960 event consisted in a sequence of 3 shocks in 33 hours, the earthquake rupture models reproduced the vertical deformation generated by all of them independently of the initiation time. Subsequently, the tsunami source model could differ from the earthquake model, due to the fact that the main shock is the most important in the 1960 tsunami. On that ground, a 5-segment rupture model based on the FFM given by Barrientos and Ward (1990) is proposed. This proposed model considered the main event, with subevents at 15:10 and 15:11, on May 22nd only. Therefore, the events on May 21st are not considered. Table 4 shows the source segments S1-S5 corresponding to the proposed FFM of the 1960 tsunami. The other parameters such as the strike, dip and rake angles are 7°, 20° and 105°, respectively.

Table 4. Primary source parameters used for Okada's (1985) source segments S1-S5 corresponding to 1960 tsunami.

Parámetro	S1	S2	S3	S4	S5
X0 (Lon)	75.154	75.246	75.337	75.521	76.014
Y0 (Lat)	39.60	40.20	40.80	42.00	45.00
Focal Depth (km)	30	30	30	30	30
L (km)	95	67	67	133	335
W (km)	130	130	130	130	130
D (m)	20	10	25	12	5

Figure 26 shows the initial sea surface deformation for both the PFM and the FFM of the 1960 tsunami. The PFM and the FFM were validated with tsunami records at Talcahuano, Tirúa, Corral and Ancud in the work of Aránguiz (2013). In general, both rupture models gave similar behavior in all places and the maximum tsunami amplitudes are in good agreement with tsunami records. However, the PFM overestimates the amplitude of the first tsunami wave at Talcahuano and underestimates the tsunami arrival time, i.e. the tsunami arrives earlier. It is obvious since the PFM considered the whole rupture area, therefore, the northern border of the tsunami source is closer to the Bay of Concepción. In addition, the FFM gave a better adjustment to the tide record at Talcahuano, mainly the arrival time and amplitude of the first tsunami wave.

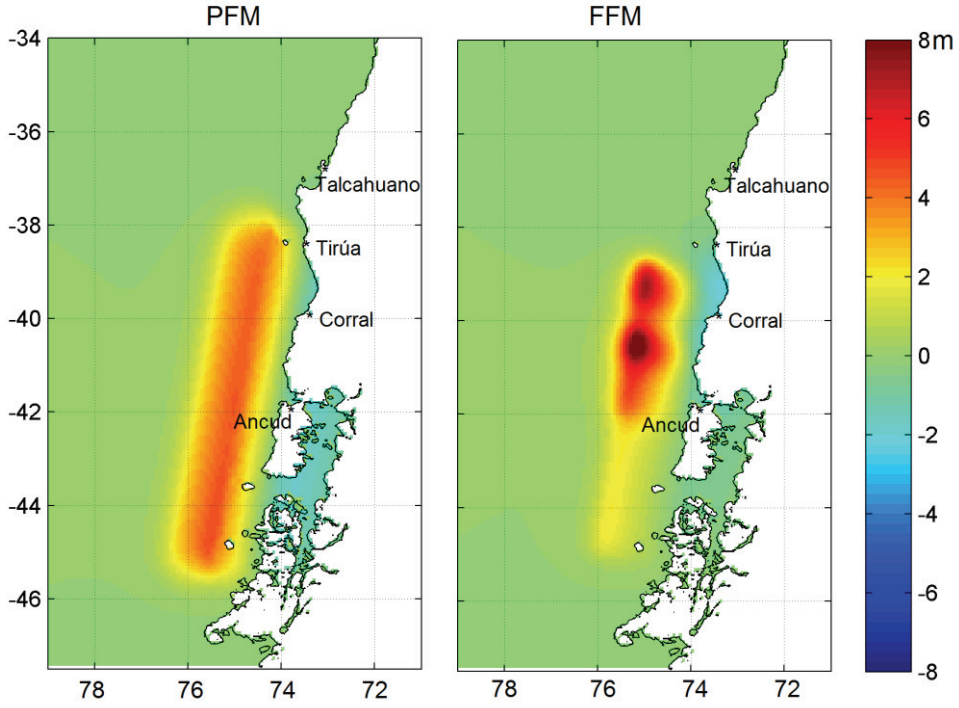

Figure 26. Tsunami initial condition for the 1960 tsunami considering the Planar Fault Model (left) and Finite Fault Model (right).

3.2.3. Results and spectral analysis

a. Behavior of the 2010 tsunami

Figure 27 shows a snapshot of the computed sea surface elevation propagation of the 2010 tsunami every 10 min during the first 20 min. The left hand side frame shows the initial sea surface elevation given by the FFM. The tide Gauges 6 and 7 are also shown in the Figure. It is seen how the bathymetry influences the tsunami propagation, thus tsunami waves arrive earlier at Consitucion, due to deep water, and later at Bay of Concepcion and Talcahuano, due to wider continental shelf. Figure 28 shows the wavesforms and energy spectra at gauges 7 and 6. The former is located at deep water, and recorded the tsunami waves propagating toward the Pacfic Ocean, while the latter is located over the continental shelf close to the entrance of the Bay of Concepcion at a water depth of 60 m. In Figure 28, it is possible to see that the spectral amplitude at Gauge 7 shows to have 3 distinct periodic components and several small peaks at shorter periodic components. There is a large bandwidth between 130 and 200 min, with peak around 170 min, however, the largest spectral amplitude corresponds to a periodic component of 85 min. Comparing the spectral amplitude of Gauge 7 with Gauge 6, the spectral amplitude increased in all periodic component, however, the spectral amplitude

between 70 and 110 min is amplified more than the other components with a maximum spectral amplitude at around 90 min. In addition, the first resonant mode over the continental shelf has a narrower bandwidth at around a periodic component of 130 min. The shorter component at 28 and 42 min are still present but with lower spectral amplitudes. Figure 29 shows the maximum inundation heights in the Gulf of Arauco and the Bay of Concepcion. The contourlines of a water depth 50, 200 500 and 1000 m are also plotted in order to see the location of the Biobio Submarine Canyon. It is seen that the inundation heights are in good agreement with the field measurements shown in Figure 14, i.e. large inundations at the southern shore of the Bay of Concepcion and low inundation at the eastern shore of the Gulf of Arauco. In order to analyze the tsunami behavior inside the Bay of Concepcion, Figure 30 shows the timeseries and amplitude spectra at three location inside the Bay, namely, Tome, Penco and Talcahuano. It is seen that the amplitude spectra is significantly amplified inside the Bay for the three locations, and the maximum amplitude take place for a periodic component at around 90 min, which is almost the same as the one obtained at the continental shelf. Therefore, the tsunami behavior inside the Bay of Concepcion is strongly influence bay the shelf resonance in front of the Bay.

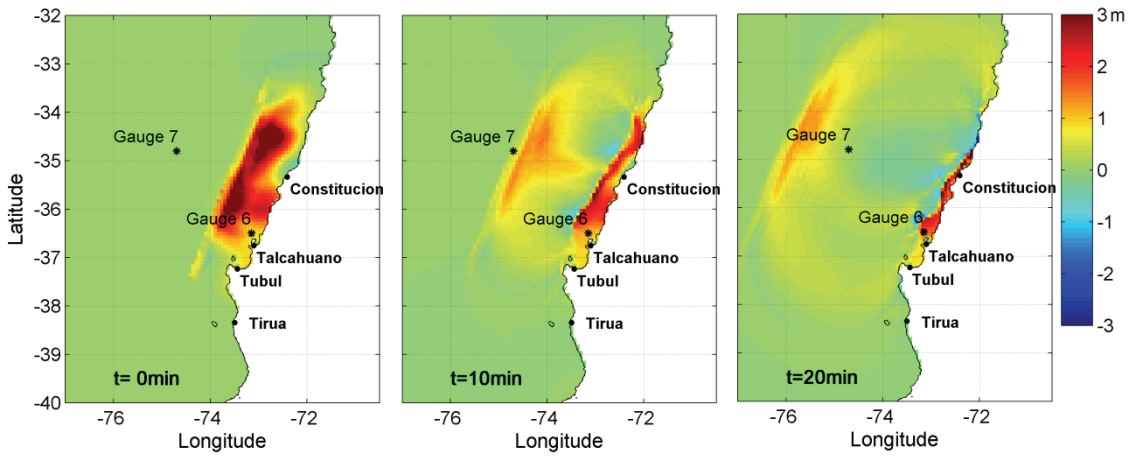

Figure 27. Snapshot 2010 Chile tsunami with FFM of the initial sea surface perturbation

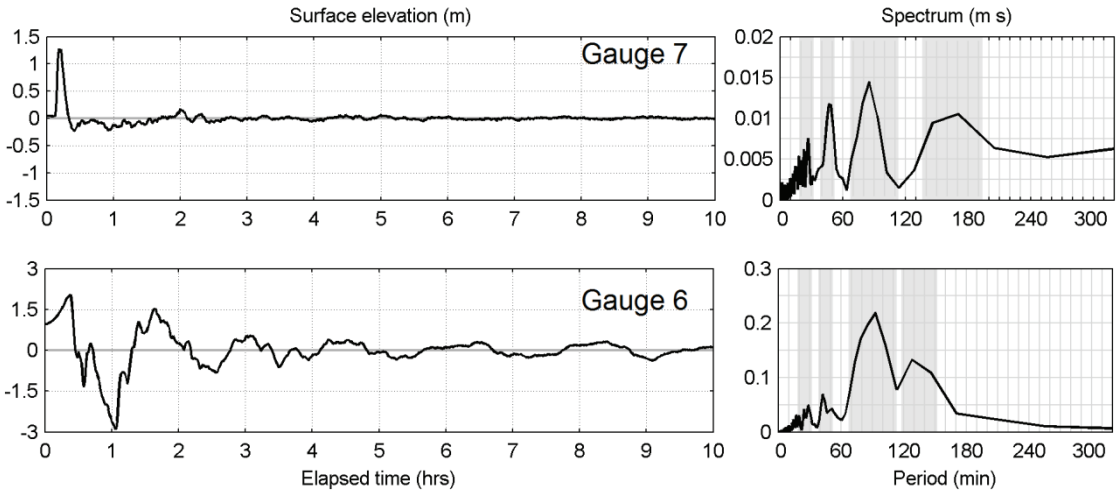

Figure 28. Waveforms and spectral amplitude at Gauges 7 and 6 due to 2010 Chile tsunami

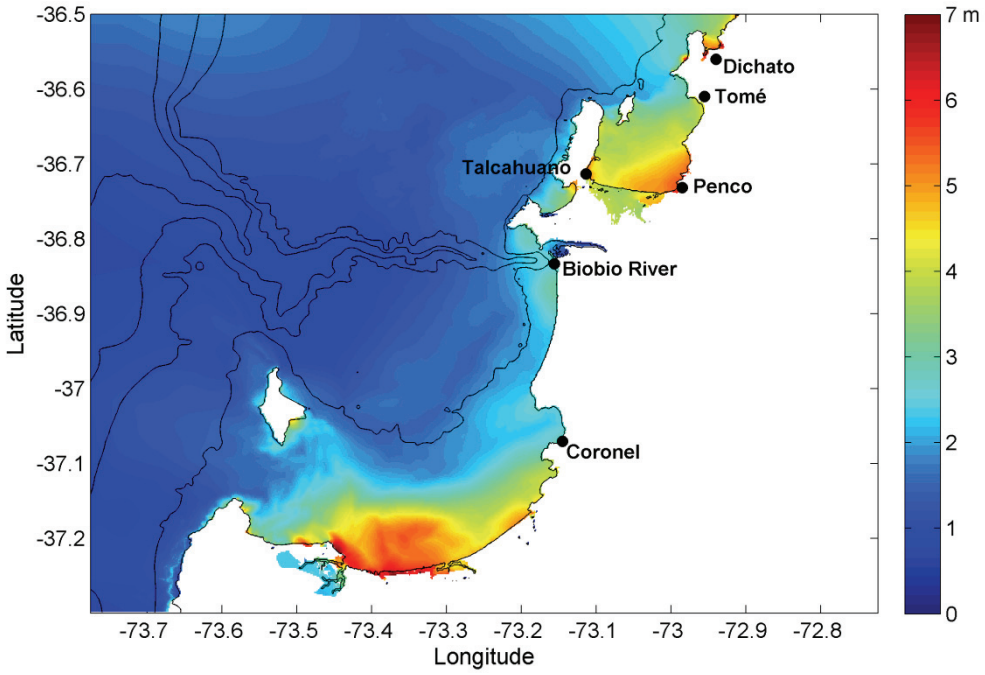

Figure 29. Inundation heights at the eastern shore of the Gulf of Arauco and the Bay of Concepción obtained from simulation of the 2010 Chile tsunami with FFM.

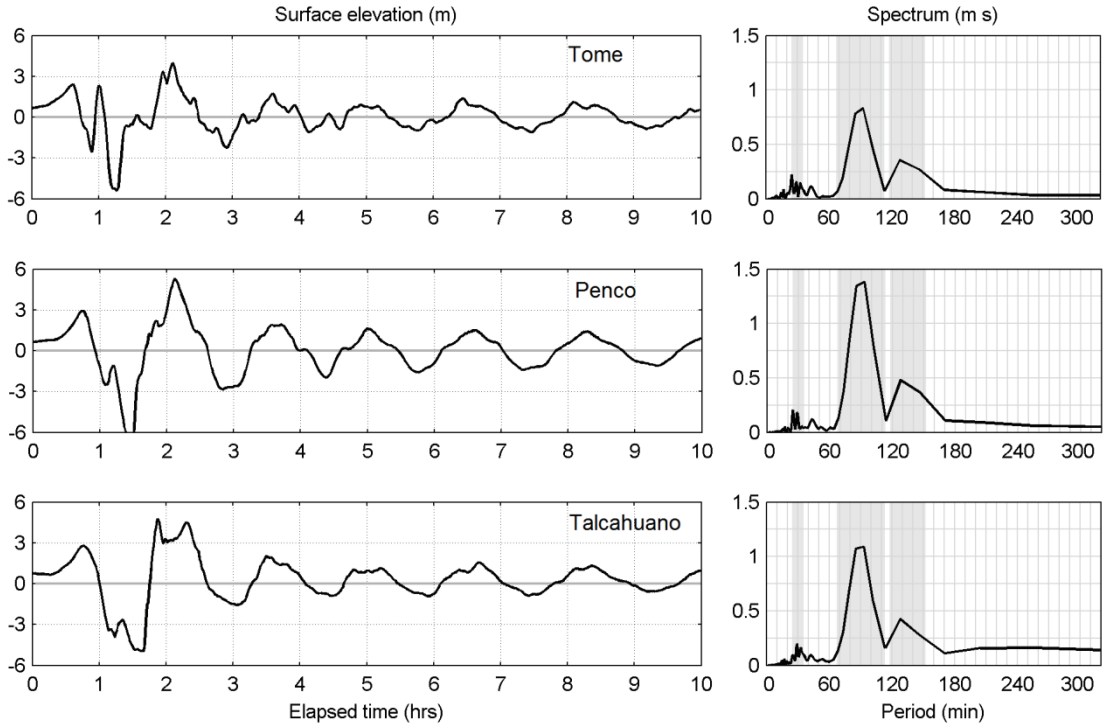

Figure 30. Tsunami waveforms and spectral amplitude at three locations inside the Bay of Concepcion for the computed 2010 Chile tsunami

b. Behavior of the 1877 Tsunami

Figure 31 shows two snapshots of the computed sea surface elevation with a focal depth of 30 km. The main tsunami wave propagates away from the rupture with radial direction. After 30 min, the first tsunami wave hits the coast and a large ebb is generated. After 90 min the generation of edge waves can be observed. These waves propagate as a trapped wave along the continental shelf in a north-south direction.

Figure 32 shows the time series and amplitude spectra of the computed surface elevation at experimental water level stations, Gauges 1 to 6, and for a focal depth of 30 km. Gauge 1 is located south end of the initial deformation to analyze the initial tsunami wave propagating toward south. Gauge 2 and 4 are located off Valparaiso at 5000 m and 200 m water depth, respectively. Similarly Gauge 3 at 5000m depth and Gauge 5 at 200 m depth are located off Constitucion. Gauge 6 at 60 m depth is located in front of the entrance of the Bay of Concepcion. The spectral amplitude at Gauge 1 shows the first resonance mode with a large bandwidth between 65 min and 160 min periods with peak around 113 min, and two distinct short periodic components around 46 min and 58 min. Comparing the spectral amplitude at Gauge 1 with other gauges, the primary oscillation mode with a bandwidth from 65 min and 115 min are observed at gauges 2~6. Gauge 6

also show larger spectral amplitude between 65 min are 115 min, but it additionally has large amplitude up to 160min. Note that the oscillation mode with large bandwidth between 65 min and 160 min periods at Gauge 6 is consistent with Gauge 1. The primary large spectral distribution between 65 min and 115 min at Gauge 2 ~ 6 are due to resonance over the continental shelf and slope. Gauge 4, 5, and 6 over relatively shallow and flat continental shelf has larger spectral amplitude in this longer periodic components, and Gauge 2 and 3 over the steep continental slop has smaller amplitudes which corresponds to the spectral analysis in Yamazaki and Cheung (2011). The increase of spectral amplitude over large bandwidth from 65 min to 160 min is only observed at Gauge 6 because the continental shelf are wider in front of the Bay of Concepcion than shelves around Gauge 4 and 5.

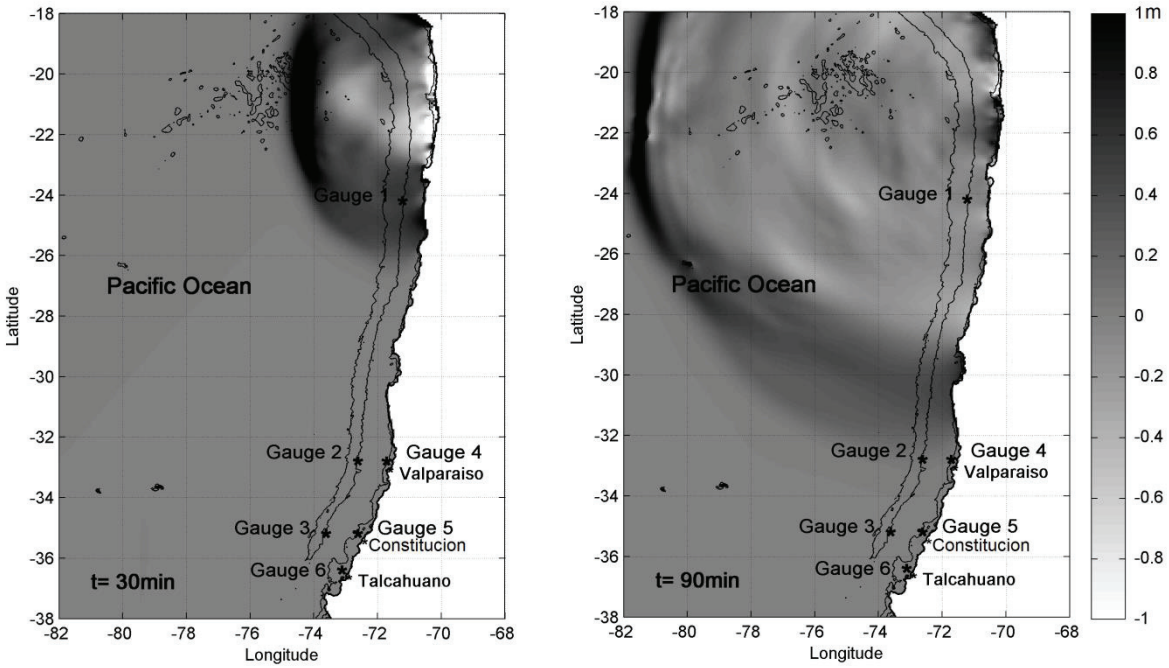

Figure 31. Snapshot of surface elevation during propagation of the 1877 Iquique tsunami.

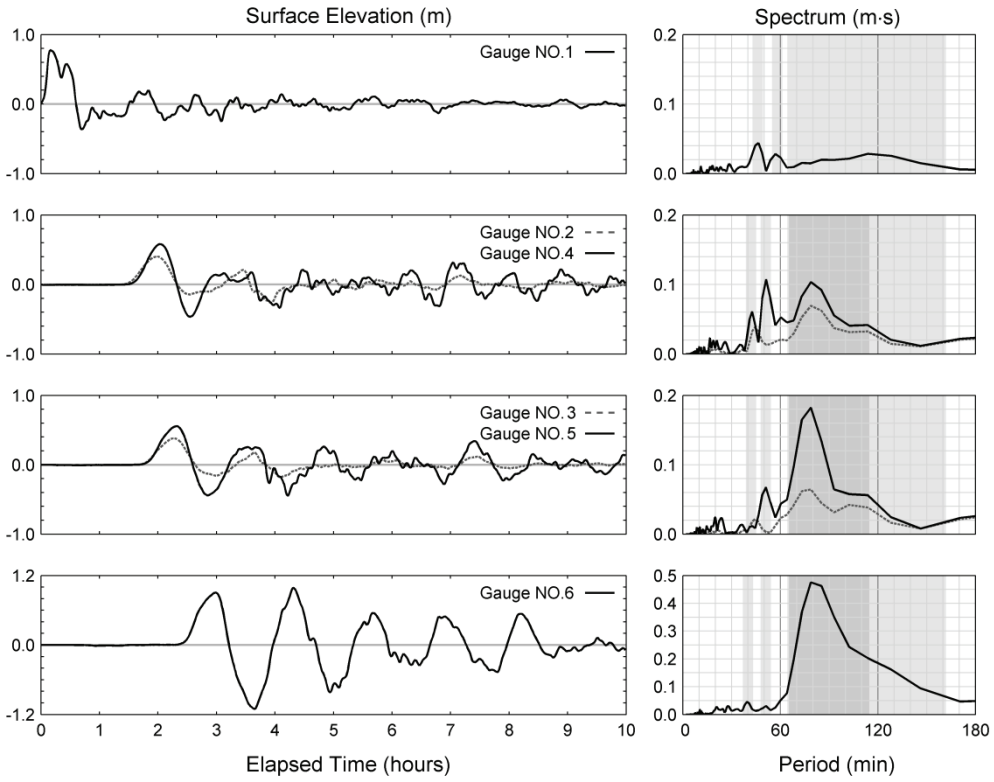

Figure 32. Time series of surface elevation and spectrums of tsunami waves at all gauges for a focal depth of 30km.

Figure 33, Figure 34, Figure 35 and Figure 36 show the computed waveforms at the experimental Gauges 1~6 with three different focal depths to investigate the effects of focal depths on tsunami amplitude using spectral analysis, as was observed in Figure 25. The computed results at Gauge 1 with three focal depths in Figure 33 show different waveforms which are consistent with the initial deformation from the formulation of Okada (1985), i.e. the shallower the earthquake, the higher the initial sea surface perturbation. The computed waveform with 30 km focal depth has two distinct initial peaks. The computed results with the 40 km depth also show two peaks, even they are not clear as the ones with the 30 km depth. Then the 50 km result only has one peak. From the spectral analysis of the initial tsunami wave in Figure 33, it is seen that there are short periodic components and they show linear variation in spectral amplitude with focal depth. The ~35 min periodic component's spectral amplitude increases and ~46min component decreases with increase of focal depth. But, the wide range of longer periodic components from 65 min around 160 min periods increases the spectral amplitude from 30 km to 40 km focal depth, but decreases at 50 km depth. The short periodic waves with linear variation and the longer periodic components with maximum spectral amplitude at the 40 km focal depth are consistent with all gauges. Shallower earthquakes generate short periodic components, but their spectral amplitudes decrease

as the tsunami wave propagated along the coast. Hence, the maximum tsunami amplitude at Gauge 6 is due to the increase of spectral amplitude of the large bandwidth between 65 min and 160 min. The maximum spectral amplitude is obtained for a periodic component around 85 min, which is also close to the resonant component found at Gauge 6 during the 2010 tsunami.

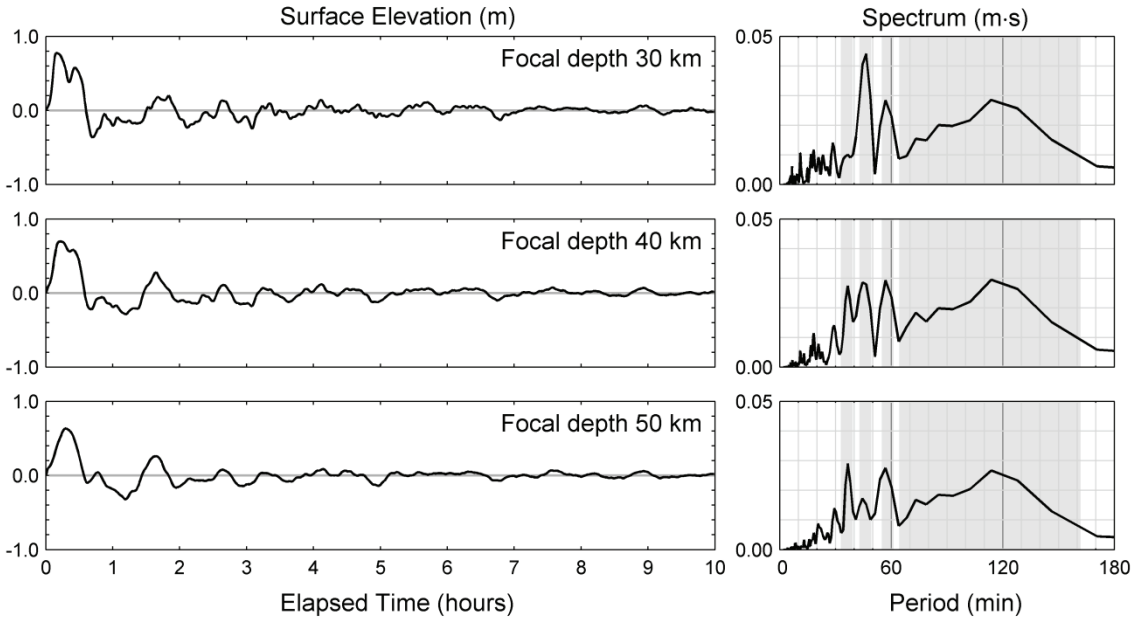

Figure 33. Time series of surface elevation and spectrums of tsunami waves at gauge 1 at water depth of 5000m.

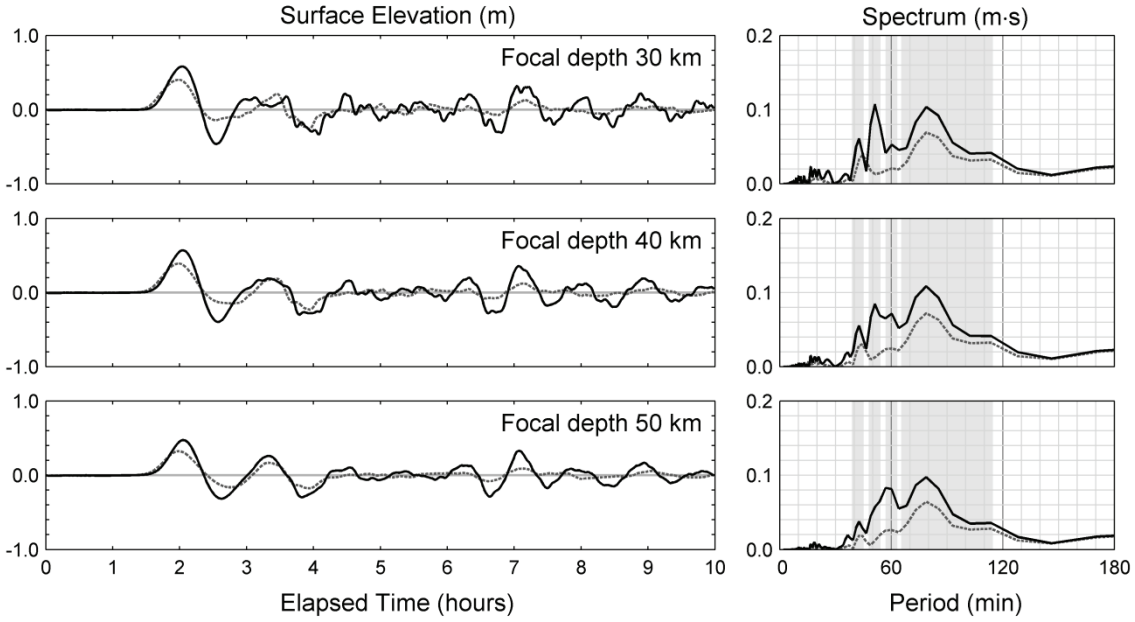

Figure 34. Time series of surface elevation and spectrums of tsunami waves at gauge 2 and 4 at a water depth of 5000m (dotted line) and 200m (continuous line), respectively.

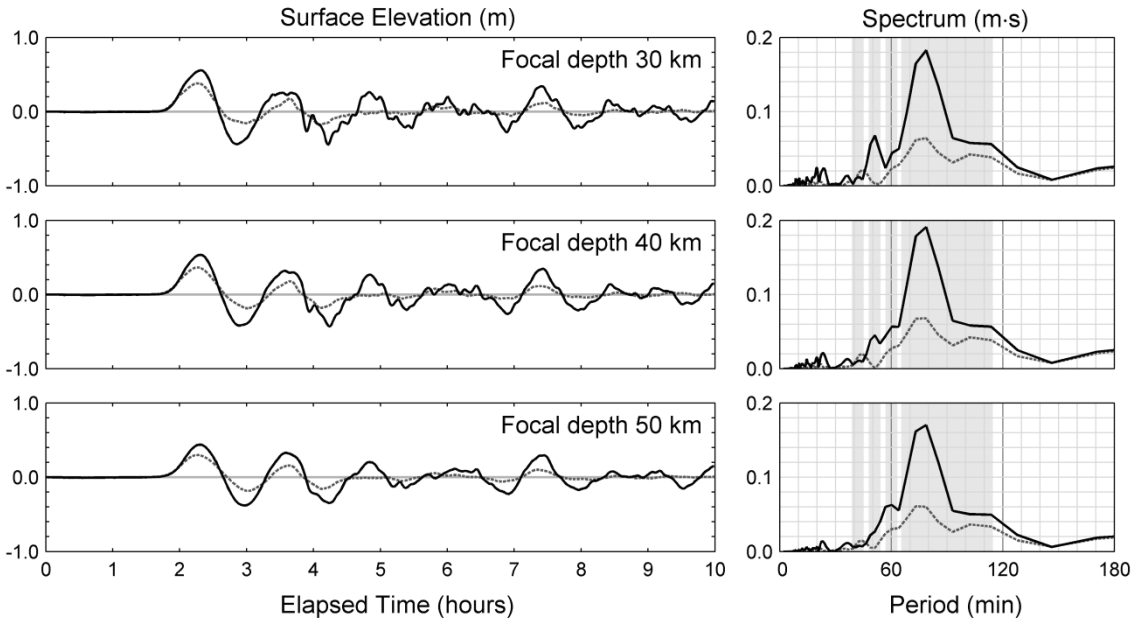

Figure 35. Time series of surface elevation and spectrums of tsunami waves at gauge 3 and 5 at a water depth of 5000m (dotted line) and 200m (continuous line), respectively.

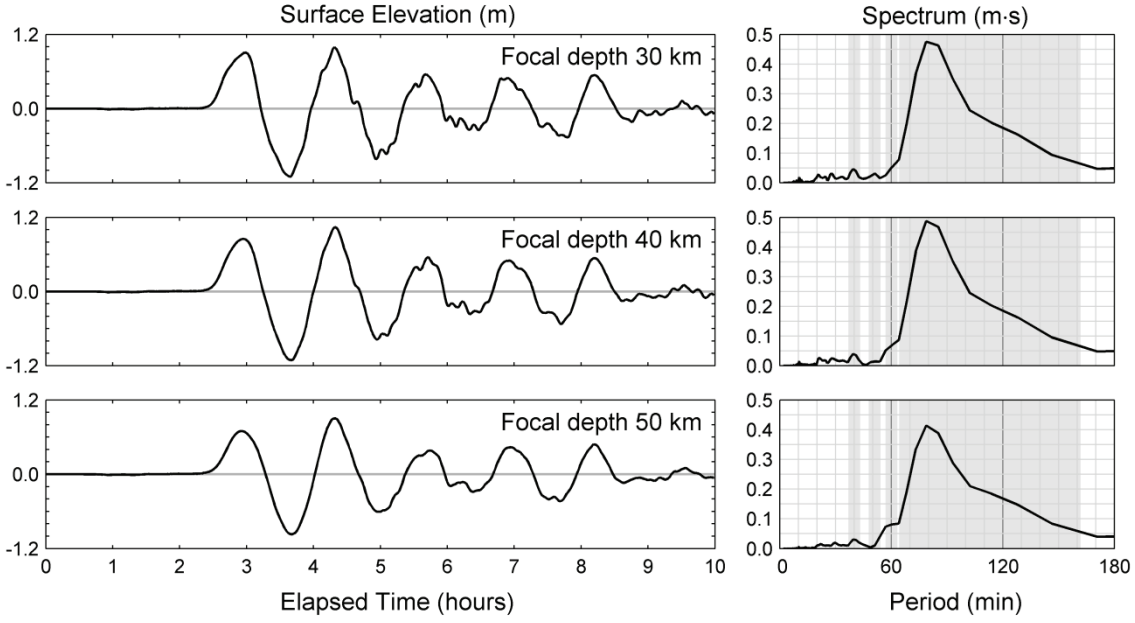

Figure 36. Time series of surface elevation and spectrums of tsunami waves at gauge 6 at a water depth of 60m just north of the Bay of Concepcion.

Figure 37 shows the inundation heights in the Gulf of Arauco and the Bay of Concepcion. The contour lines at 50, 200, 500 and 1000 m water depth are also shown in the Figure. While Dichato and the southern shore of the Gulf of Arauco did not experience large inundation, as in the 2010 tsunami (See Figure 29), the Bay of Concepcion showed to have significant tsunami amplification. In addition, the eastern

shore of the Gulf did not experience inundation, especially at the river mouth, just front of the submarine Canyon. This behavior is analyzed in the following section.

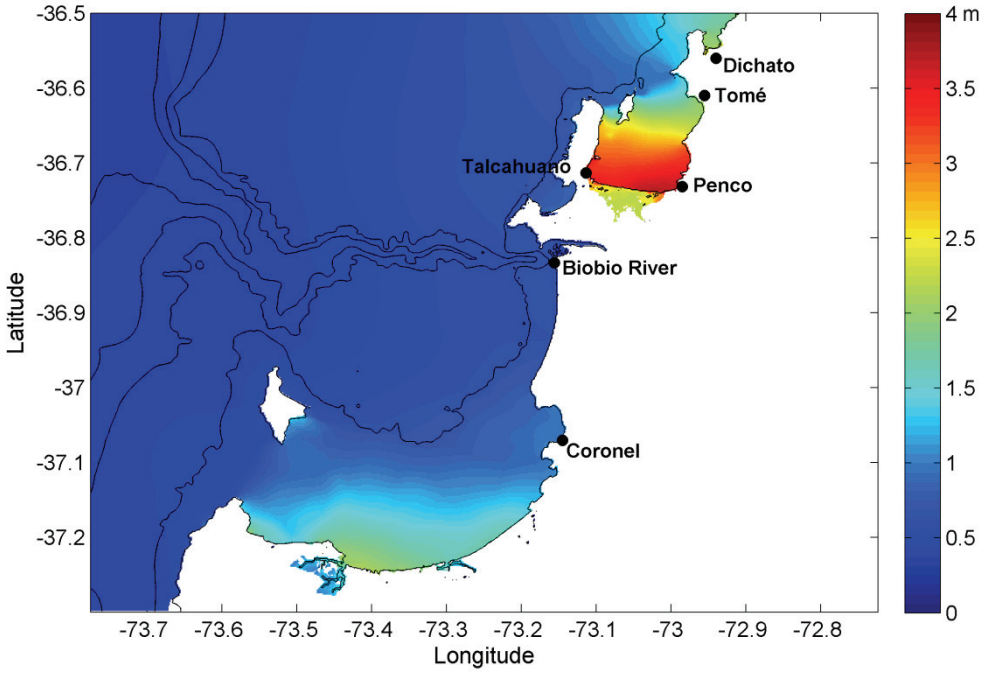

Figure 37. Inundation heights at the eastern shore of the Gulf of Arauco and the Bay of Concepción obtained from simulation of the 1877 Iquique tsunami with a focal depth of 30 km.

Figure 38 shows the waveforms and the spectral amplitudes at Tome, Penco and Talcahuano. Comparing the spectral amplitudes at Penco and Talcahuano with Gauge 6 in Figure 32, the spectral amplitude is significantly amplified. In addition, the large bandwidth is still present and the maximum amplitude is obtained at 90 min. Now, comparing also the computed tsunami at Talcahuano and Valparaiso, it is seen that the former show larger tsunami amplitude than the latter, as seen in Figure 24, regardless of fault orientation and focal depth, even though Talcahuano is located further away from the source. In addition, the secondary wave is the largest among all sensitivity tests. The significant tsunami amplification with the largest secondary wave was also observed during the 2010 tsunami, as seen in Figure 28. This indicates Talcahuano always experiences significant tsunami amplification with maximum amplitude at the secondary wave from both near-field and far-field tsunamis from the North. Yamazaki and Cheung (2011) found the fundamental mode of oscillation occurs in the Bay of Concepcion with a well defined node near its entrance around 64, 73, 79, and 93min periods for the 2010 Chile tsunami, and concluded coupling between embayment

oscillations with large-scale shelf resonance caused localized impacts and belated arrivals of largest wave at Talcahuano. This phenomenon is analyzed in detail in following sections.

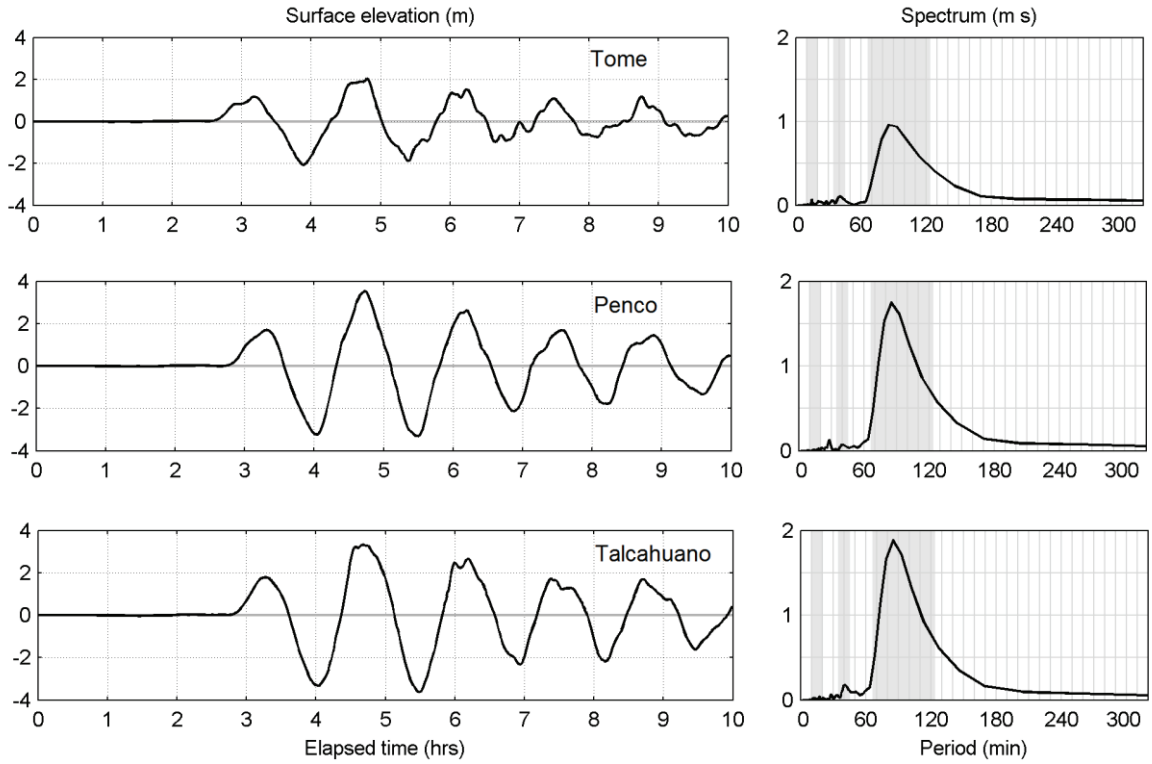

Figure 38. Tsunami waveforms and spectral amplitude at three locations inside the Bay of Concepcion with 1877 Chile tsunami

c. Behavior of the 1960 tsunami

Figure 39 shows a snapshot of the first 30 min of the computed tsunami with the PFM. The tide Gauges 6, 8 and 9 are also shown in the Figure. As in previous cases, the Gauge 6 is used to analyze the tsunami behavior over the continental shelf, while Gauges 8 and 9 are located in deep water. The seabed morphology influences the tsunami propagation, thus a large tsunami wave is observed at Mocha Island, Tirua, Corral and Ancud. This computed behavior is on good agreement with field measurements given in Table 1. The tsunami wave forms and spectral amplitudes at Gauges 6, 8 and 9 are given in Figure 40. It is seen that Gauge 8 shows to have two main periodic components, one at around a period of 80 min, and a large bandwidth from 120 to 300 min. These periodic components were also observed at Gauge 7 in the case of 2010 Tsunami, as shown in Figure 28. In a similar manner, as the computed

1960 tsunami propagated toward the Gulf of Arauco, the first resonance mode concentrated the spectral energy between 100 and 180 min with a peak at around 130 min. In addition the spectral amplitude is strongly amplified. On the contrary, the periodic components between 50 and 80 min are not largely amplified as the previous case, and the spectral amplitude is relatively low. Moreover, an even shorter periodic component between 30 and 40 min is also amplified as the tsunami approaches the Bay of Concepcion.

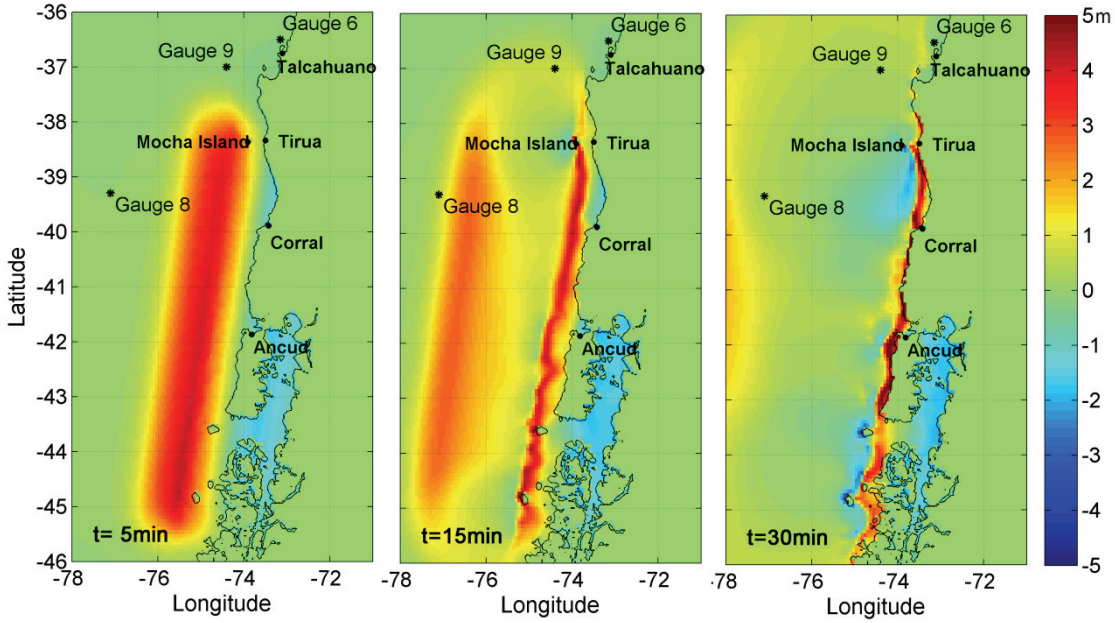

Figure 39. Snapshot of 1960 tsunami with a slip of 15 m

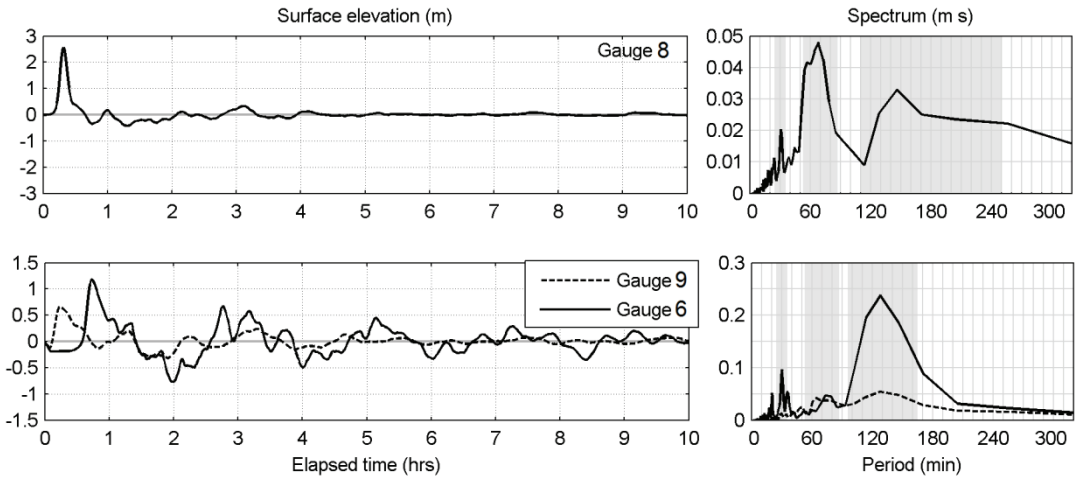

Figure 40. Waveforms and spectral amplitude at Gauges 6, 8 and 9 due to 1960 tsunami

Now, Figure 41 shows the maximum inundation heights from the computed 1960 tsunami with both the PFM and the FFM. The maximum inundation at Dichato, Tome, Talcahuano and Coronel, agree well with measurement given in Table 1. In addition, the river mouth experienced an inundation height less than 2 m. Figure 42 shows the waveforms and spectral amplitudes of the same selected three location inside the Bay of Concepcion, namely, Tome, Penco and Talcahuano. It is observed that the spectral bandwidth between 100 and 180 min periods is amplified in a similar proportion as in the case of the 2010 tsunami, however, a new component tends to grow at around 90 min, which was not significant at the entrance of the Bay. Therefore, this periodic component could be related to natural oscillation modes of the Bay. In addition, a short periodic component around 30 min is also amplified inside the Bay, and can reach a spectral amplitude comparable with the first resonant component at 130 min, despite the spectral amplitude outside the Bay was not significantly larger. Therefore, the computed 1960 tsunami showed to have more important resonant components at 30 and 130 min than at 90 min as the previous cases.

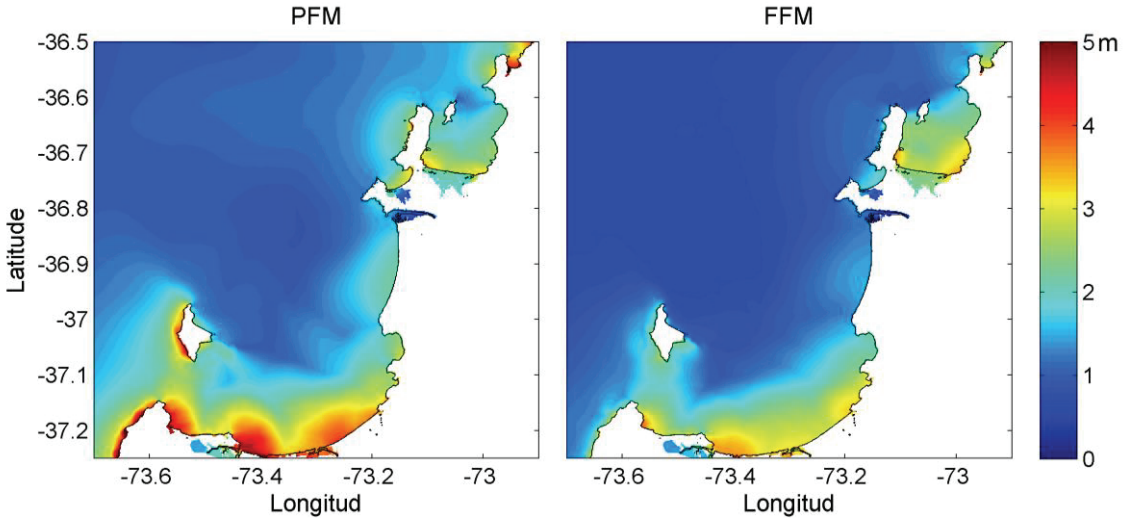

Figure 41. Inundation heights at the eastern shore of the Gulf of Arauco and the Bay of Concepción obtained from simulation of the 1960 tsunami with an average slip on 15m

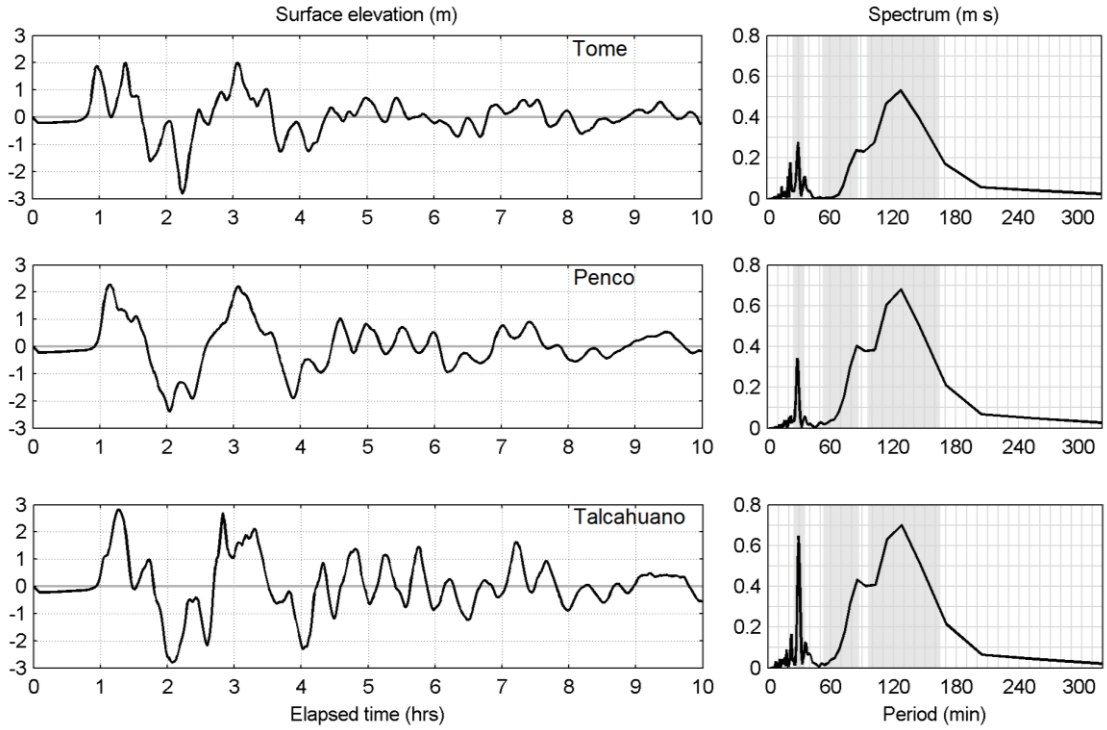

Figure 42. Tsunami waveforms and spectral amplitude at three locations inside the Bay of Concepcion for computed the 1960 tsunami

3.3.Seabed morphology and behavior of past tsunamis

The results obtained in the previous section indicated that tsunamis can behave differently depending on the tsunami sources. However, it was also observed that some patterns are repeated independently of the sources. As a matter of fact, the southern shore as well as the eastern shore of the Gulf of Arauco behaved in the same way independently of the tsunami scenario. While the former experienced always a significant inundation height the latter had the lowest inundation. Preliminary results on that behavior can be found in Aranguiz (2012), where near field tsunamis were simulated using the TUNAMI code. In this work, the effect of the submarine canyon showed to be the most important reason for such a behavior. The effect of the susbmarine canyon is analyzed in detail in the present chapter.

On the other hand, the Bay of Concepcion experienced always the largest inundation height at the southern shore of the Bay independently of the tsunami source. It was expectable that the 2010 tsunami generated large inundations inside the Bay, due to the proximity of the source. However, the computed 1960 tsunami generated lower inundations heights than the tsunami from northern Chile, despite the location of the tsunami source. As mentioned earlier, it was believed that the diffraction and refraction

processes due to the presence of Tumbes peninsula helped to decrease the tsunami wave amplitude inside the Bay de Concepcion. However, the inundation in Dichato is extremely high for a north oriented bay, similar to the Bay of Concepcion (see Figure 41). On the contrary, the computed 1877 tsunami from the north generated low inundation heights in Dichato and large inundation in the Bay of Concepcion, as seen in Figure 37. In addition, the spectral amplitudes at the Gauges 6, over the continental shelf, showed significant amplification in some periodic components only (See Figure 28, Figure 32, and Figure 40), which could be related to the tsunami behavior inside the Bay of Concepcion. Therefore, the tsunami resonance and the natural oscillation modes of the Bay are analyzed in detail in the present section

3.3.1. Tsunami Resonance in the Bay of Concepcion

The resonance phenomenon in bays and harbors has been studied for many years, due to the fact that wave amplification is important for safe ship mooring, anchoring conditions, and wave run-up. The first approaches consider mathematical solutions for oscillations of bays of simple geometries as well as arbitrary shape and variable depth (Olsen and Hwang, 1971; Loomis, 1973). Analytical solutions for normal modes and frequencies in semi-enclosed basins are given in Rabinovich (2009).

In present years, the tsunami amplification within semi-enclosed basins has also become an important topic. Understanding the tsunami wave energy transference from the open ocean into a basin and the tsunami behavior within the basin is important in tsunami risk reduction, thus countermeasures should take into account which parts of the basin would experience the greatest amplitudes. The tsunami resonance has been studied by means of both analytical and numerical approached. Ferraras (1978) made the first preliminary analysis of the tsunami resonance in the Bay of Concepcion. He analyzed three tsunami records and compared the normalized energy density spectra with theoretical expressions for a rectangular semi-enclosed basin. Sandoval et al., (1993) analyzed the resonance in the Gulf of California (Mexico) using analytical long-wave solutions for a rectangular basin of constant and variable depth. Henry and Murty (1995) used a two-dimensional model in a finite elements framework to study the tsunami amplification due to resonance in the Alberti Inlet. Recent works have used more sophisticated methods to find the resonance modes by solving the equations for its eigenfunctions. Sobey (2006) used a normal mode decomposition by means of a Sturm-Liouville problem and typical eigenmode solution for spatially varied basins in one and

two spatial dimensions are given. The tsunami resonance in Palma de Majorca was studied by Vela et al. (2010) in which a numerical model based on the Mild Slope Equation was used. Since the model solves elliptic form of the equation for linear waves, permits to include reflective, absorbing and partial absorbing boundary conditions. Belloti et al. (2012) proposed a new method for modal analysis of semi-enclosed basins which solves the shallow water equation with an approximate radiation condition at the boundary. On the other hand, the use of the Empirical Orthogonal Funtion has been applied by Tolkova and Power (2011) for obtaining natural oscillatory modes of bays. This method analyses the sea surface variation obtained from numerical simulations of tsunami into the bay. They concluded that the EOF solution appears to be more accurate than numerical solutions resulting from the classical eigenvalue-problem approaches or theoretical estimates.

Another important point to have in mind is the influence of the open ocean in open bays, such that the fundamental period spreads outside the bay for another length of the bay. As an example, the seiching from tsunami at Poverty Bay in the Northern Island of New Zeland is dominated by the shelf resonance rather than the bay's own oscillation (Tolkova and Power, 2011). In a similar manner (Roeber et al., 2010), analyzed the 2009 Samoa tsunami around Tutuila island, and found that large runup were due to tsunami wave amplification caused by resonance in shelf and embayment configurations. Moreover, the 2010 Chile tsunami showed further amplification at Talcahuano inside the Bay of Concepcion, which results from resonance over the wide continental shelf in front of the Bay of Concepcion coupling with embayment oscillations inside the Bay (Yamazaki and Cheung, 2011). The fundamental modes of oscillation in the Bay of Concepcion with a well defined node near its entrance were found to be around 64, 73, 79, and 93min periods for the 2010 Chile tsunami (Yamazaki and Cheung, 2011) and they concluded coupling between embayment oscillations with large-scale shelf resonance caused localized impacts and belated arrivals of largest wave at Talcahuano.

The present section studies the tsunami resonance within the Bay of Concepcion. The results in this section are contrasted with results given by the numerical simulation of past tsunamis.

a. The study area

The Bay of Concepcion is a semi-enclose basin of 11km in width and 14km in length. The maximum water depth at the entrance is 40m. Historical records show that

the Bay has been affected by several tsunamis, as a matter of fact, in 1570, 1657, 1730 and 1751 destructive earthquakes and tsunamis hit the city of Concepción. At that time, Concepción was located at what is today Penco. Local authorities decided to move the whole city to a higher place. Three alternatives were proposed to the neighbors, and they decided to move to a place between the Biobio and Andalién Rivers called *Valle de la Mocha*. Therefore, it could be said that the first mitigation measure was taken in 1751 as a retreat strategy, and the neighbor participated actively on that. Since Concepcion was then far from shore, the new port of Talcahuano was founded in 1764. In addition, Penco started to be repopulated from 1822 to 1843. Nevertheless, another large earthquake and tsunami occurred in 1835, which inundated the recently founded port of Talcahuano and the repopulating town of Penco. The maximum runup in Talcahuano was estimated to be 9m, while 4m was observed at Tome (Soloviev and Go, 1975).

Similar situation happened in 2010, where the maximum inundation height and runup reached 7 and 8m in Talcahuano, respectively, while Tomé experience a runup less than 4m (Fritz et al., 2011). Both the 2010 and 1835 tsunamis are near field tsunamis generated in the same seismic zone. In addition, the 2011 Japan tsunami generated a tsunami wave amplitude of 2m in Talcahuano (http://www.ioc-sealevelmonitoring.org/) which was not high enough to inundate the lower areas.

Yamazaki and Cheung (2011) concluded that the large tsunami inundation height observed in the southern shore of the Bay of Concepcion, was due to shelf resonance coupling with embayment oscillations inside the Bay. Ferraras (1978) estimated the natural periods of the bay by means of empirical expressions and assuming a rectangular basin (L=14.6km and W=11.7km) with a mean water depth of 25m. The periods were computed to be 15, 27 and 111min. If the varying water depth is now considered, and the same values of length and width are used, mathematical formulations given by Rabinovich (2009) give values of the natural periods as 13, 21 and 64 min. None of the previous computation considered the island at the entrance of the Bay. Therefore, more accurate method should be applied.

b. Natural oscillatory modes of Bay of Concepcion

In this subsection, the natural oscillation modes of the Bay of Concepcion will be computed by means of Empirical Orthogonal Functions (EOF). The EOF method is used for analyzing the variability of a single field, finds spatial patterns of variability, as well as the time variation and gives an idea of the weight of each pattern (Björnsson and

Venegas, 1997). Since the EOFs represent an orthogonal basis of the space shapes in which the data variance is concentrated in few functions, the shapes of these normal modes could represent an orthogonal basis for a semi-enclosed basin space. In addition, a tsunami could excite few lowest modes, therefore, these normal modes could be isolated as EOFs of the seasurface elevation data generated by different tsunami scenarios (Tolkova and Power (2011).

The Empirical Orthogonal Function (EOF) analysis decomposes a space-time data set $s = (\mathbf{r}, t)$ into a set of space patterns and time-dependent coefficients as follows

$$S(\mathbf{r}, t) = \sum_{i=1}^{m} f_i(\mathbf{r}) p_i(t) \tag{6}$$

In which $f_i(\mathbf{r})$ is the i-th EOF and $p_i(t)$ is the i-th Principal Componet (PC) . The vector $\mathbf{r}$ represents the spatial domain and it has a length of n_s, while t is the time with a timeseries length of n_t. The EOFs are the normalized eigenvectors of the $n_s \times n_s$ Hermitian Matrix $R = S^T S$, also called the covariance matrix of S. The eigenvectors are found by solving the following eigenvalue problem

$$RC = C\Delta \tag{7}$$

Where Δ is a diagonal matrix containing the eignvalues λ_i of R. The column vector f_i of the matrix C are the eigenvectors corresponding to the eigenvalue λ_i, i.e. the EOF_i. The eigenvectors can be rearranged as a map and ordered according to the size of the eigenvalue, thus the EOF_1 is the eigenvector associated with the biggest eigenvector.

The EOF method cannot separate two oscillating system whose normal modes are not mutually orthogonal. Therefore, the shelf resonance must be excluded from the numerical solution. To do this, Tolkova and Power (2011) proposed to use a numerical domain excluding the continental shelf and generates initial free surface deformations within the semi-enclosed basin only, thus the internal normal modes of the bay are excited during a tsunami event. In addition, several tsunami scenarios are used and the data are concatenated in order to have longer timeseries, due to the fact that normal oscillatory modes do not depend on the scenario. Figure 43(a) shows the Bay of Concepcion and the location of the 6 scenarios. The initial deformation was in the shape

of a round Gaussian hump, as proposed by Tolkova and Power, (2011), given by the following expression

$$\eta = ae^{-r^2/2\sigma^2} \tag{8}$$

Three set of values of a and σ, were tested in order to analyze the influence of the initial deformation. All cases used a value a =1 m, while σ took three values such as 5 2.5 and 1.5 km, in order to analyze the effect of the initial condition on excitation of natural oscillation modes. An example of the initial seasurface deformation corresponding to a =1 m and $\sigma = 2.5$ km is shown in Figure 43(b). For simplicity, the six scenarios were simulated with TUNAMI model for 10hours, and a resolution of 3 arcsec was used. The TUNAMI model uses Shallow Water equations with bottom friction in the higher resolution grids (Imamura et al., 2006). The timeseries of the six events were concatenated skipping the first 30min of elapsed time, thus the timeseries do not include the more energetic traveling wave.

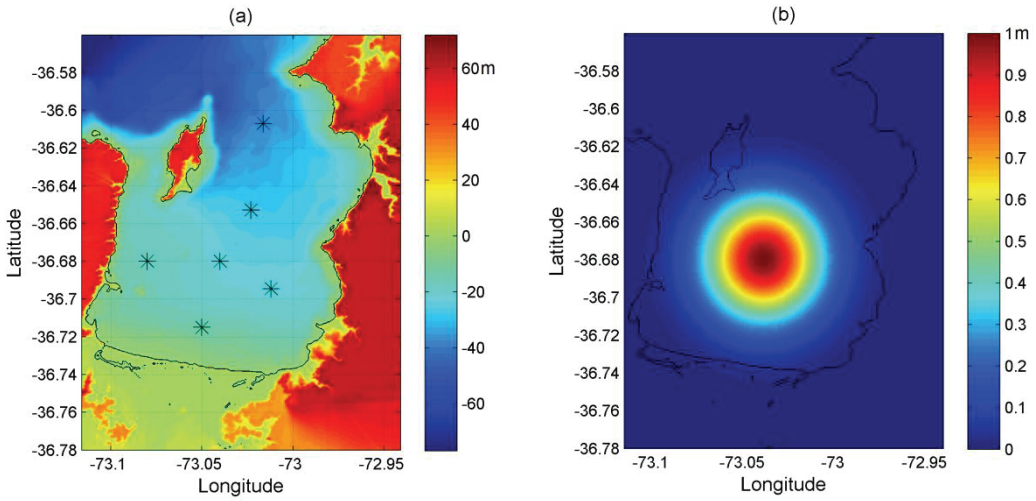

Figure 43. Application of the EOFs method to the Bay of Concepcion. (a) The Bay of Concepcion area, where the asterisks show the origin of 6 events used to derive the EOFs. (b) Example of an initial sea surface perturbation inside the Bay.

Figure 44 to Figure 46 show the set of 6 EOFs corresponding to each set of initial conditions. The colors represent normalized EOF amplitudes relative to the maximum amplitude in each mode. It is seen that in the first set of initial conditions ($\sigma = 5$ km) the 80% of the total variance corresponds to the fundamental oscillation mode. In addition, the first and second modes involve the 90% of the total variance. However, as the size of the initial condition decreases, the total variance of the fundamental mode also decreases. Thus, smaller initial conditions excite higher frequency modes rather

than the fundamental mode. As an example, the sixth oscillation mode in Figure 44, which represents only 1% of the total variance, shifts to the third mode as the σ parameter change from 5 to 2.5 km (Figure 45). Moreover, this oscillation mode changes to the second mode when $\sigma = 1.5$ km, with a total variance of 17%. Therefore, the tsunami amplification inside the Bay of Concepción is highly dependent on the tsunami wave length which excites the Bay. Nevertheless, in all cases the first mode dominates the EOF sequence. This mode oscillates along the bay and it is expectable that the shelf resonance influences this behavior too.

Figure 47 shows the power spectra of each Principal Component corresponding to the first set of initial conditions ($\sigma = 5$ km) . The period of the first along-the-bay-mode was computed to be T=95 min. However, the first EOF also contains minor mixture of other modes with longer periodic components (T=120 and 160 min) It is observed that the period of this first mode is higher than the value computed by means of formulations given by Rabinovich (2009), but smaller than values computed by Ferraras (1978). The second EOF is dominated by a mode with a period T=37 min, which is an across-the-bay mode. The third, fourth, fifth and sixth modes have periods of T=32, 25, 18, and 21 min, respectively.

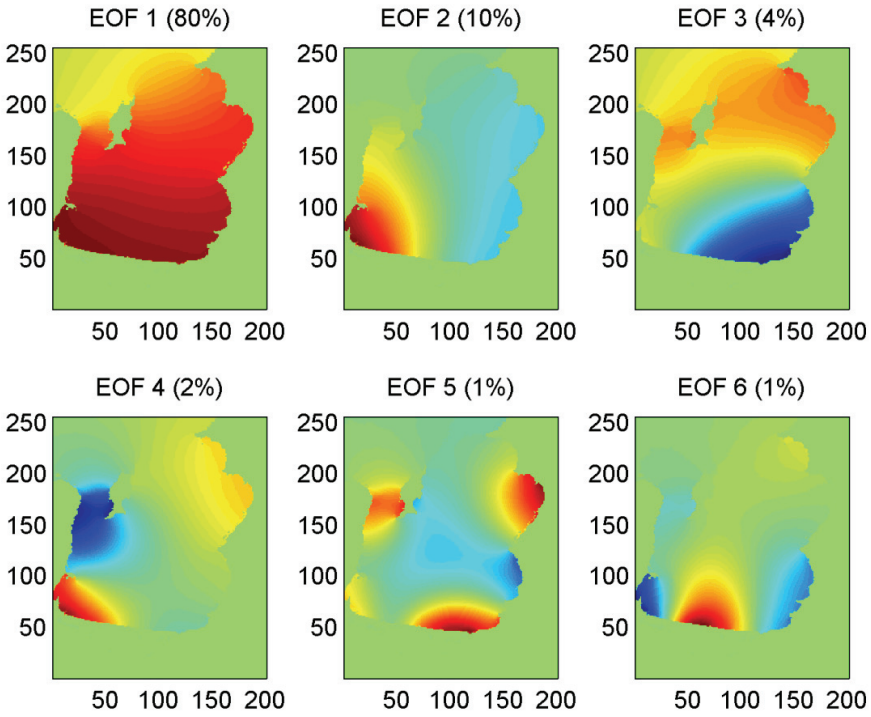

Figure 44. First to sixth EOFs of concatenated timeseries of the first set of six events ($a = 1$m $\sigma = 5$ km). Percentages of total 6-event variance explained by each EOF are shown in the plot

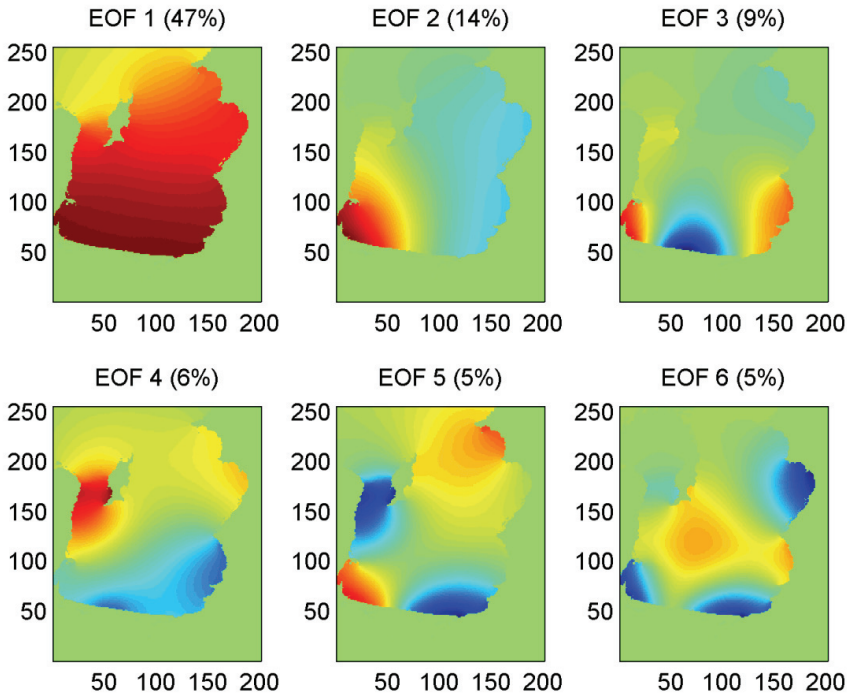

Figure 45. First to sixth EOFs of concatenated timeseries of the first set of six events ($a = 1$m $\sigma = 2.5\ km$). Percentages of total 6-event variance explained by each EOF are shown in the plot.

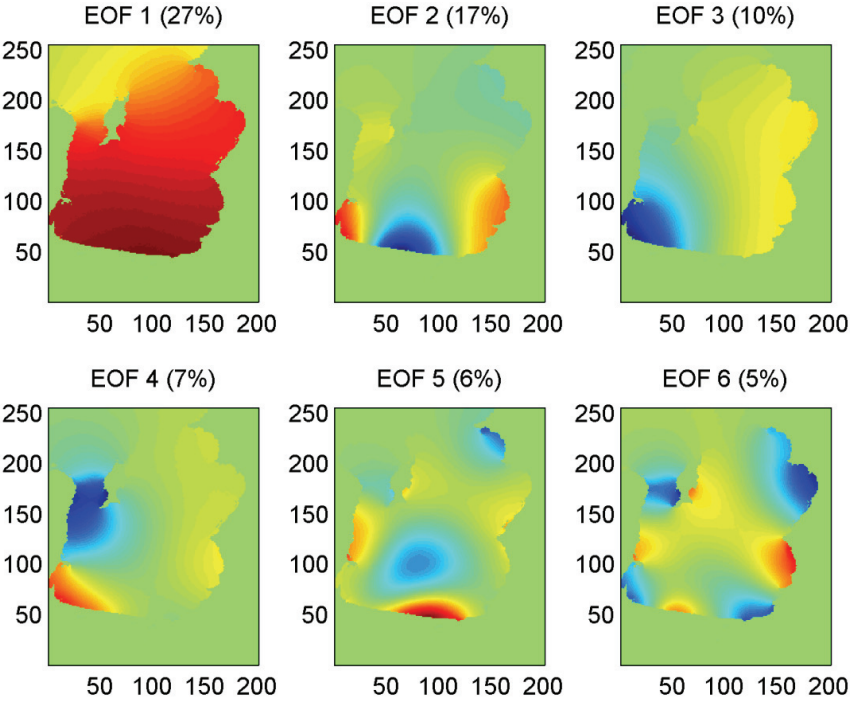

Figure 46. First to sixth EOFs of concatenated timeseries of the second set of six events ($a = 1$m $\sigma = 1.5\ km$). Percentages of total 6-event variance explained by each EOF are shown in the plot.

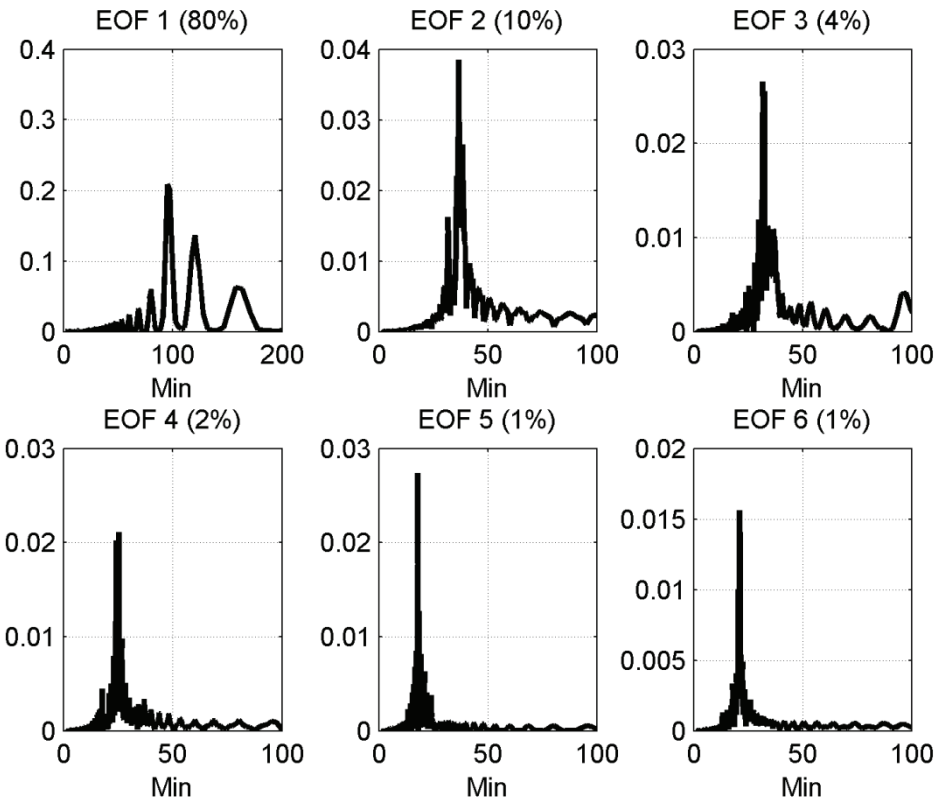

Figure 47. Power spectra of the 6 Principal Components corresponding to the 6 local events of the first set of initial conditions ($a = 1$m, $\sigma = 5\ km$).

c. Discussion

Comparing the natural oscillation modes of the Bay with the spectra computed from each scenario in the previous section, it is possible to conclude that the large tsunami amplification inside the Bay was due to excitation of natural modes. The results of both 2010 and 1877 tsunamis showed to have significant amplification at a period around 90 min with a large bandwidth, which coincides with the fundamental mode of the Bay (95 min), thus coupling between bay oscillations and large-scale shelf resonance is generated. On the contrary, the 1960 tsunami excited the second and third oscillation modes rather than the fundamental mode. It is also possible to see that the superposition of the first to the third normal modes would generate large amplitudes at Talcahuano and Penco. Therefore, large tsunami amplitudes reported at Penco and Talcahuano in past tsunami (Soloviev and Go, 1975) can be explained not only due to coupling between shelf resonance and bay oscillations, but also due to the internal normal modes of the Bay by them self. Moreover, the tsunami behavior at Dichato, inside the Bay of Coliumo could be explained based on the same analysis. The 2010 and 1960 tsunami generated large inundation because the tsunami waves excited the natural

oscillation modes, while the 1877 event did not. Therefore, further research using the EOFs in Bay of Coliumo are recommended.

3.3.2. Tsunami Propagation over Submarine Canyons

This section is part of a journal paper already published (Aranguiz and Shibayama, 2013).

Submarine canyons are narrow underwater valleys, with a typical "V" shape and very steep walls. The formation of this kind of channels is related to rivers and variations in sea water levels during different geological periods. Nowadays, submarine canyons perform an important role for sediment transport from coast to deep water (Canals et al, 2006).

Recent tsunamis of 2010 and 2004 in Chile and Indian Ocean, respectively, have shown that tsunami propagation could be affected by the presence of submarine canyons. Aranguiz (2011, 2012) studied the effect of Biobio submarine canyon located in Central Chile. In his work, several historical events were analyzed, and found that the submarine canyon which is located just in front of the 2-km-wide Biobio River can influence tsunami propagation, as tsunami waves could be caused to refract and change direction. Due to this, the tsunami would not impact directly on the coastline just in front of the canyon, reducing the inundation height compared to adjacent regions, as was observed during the field survey after 2010 Chile tsunami (See section 3.1.1). In a similar manner, other areas adjacent to submarine canyons throughout the world have shown similar behavior. The Port of San Antonio (also in Chile), a harbor located in front of another submarine canyon with similar characteristic to that of the Biobio Canyon, was not greatly affected by the 2010 tsunami. Local authorities reported a surge of only 2m inside the harbor, and 1m flow depth of water was observed at the container terminal located at the southern part of the harbor (Concejo Municipal, 2010). Elsewhere, Divyalakshmi et al. (2011) studied the effect of submarine canyons at the South East coast of India for the 2004 Indian Ocean Tsunami, and found that the presence of submarine canyon reduces wave height leeward of the canyon.

Tsunami propagating through submarine canyons has also been studied by Jinadasa (2008) and Ioualalen et al. (2007), who analyzed the effect of 2004 Indian Ocean Tsunami in Sri Lanka and Bangladesh, respectively. The former found that the maximum inundation occurred just in front of submarine canyons. In a similar manner, the latter found that the waves were amplified near the coast. In addition, Didenkulova

and Pelinovsky (2011) studied shoaling and run up in U-shaped bays, such as for the case of tsunami propagating in fjords and rias. They founded that weak reflection provides significant shoaling effect in these kinds of bays, and subsequently, significant run up effects can be observed.

The behavior of tsunami waves propagating over submarine canyons could be also influenced by other abrupt changes in bathymetry, such as those caused by the continental slope. Goring (1979) studied tsunami wave transformation on the continental slope based on a series of steps and described the wave reflection of tsunami waves onto a slope as a function of the length of the slope. Levin and Nosov (2009) proposed an expression for the reflection coefficients of waves on steps and rectangular obstacles. In a similar manner, Pelinovsky et al. (2010) studied the propagation of a solitary wave over a rectangular obstacle. In addition, Mofjeld et al. (2000) analyzed the non-normal incidence of a tsunami wave on a vertical escarpment, and defined the critical incident angle beyond which the incident wave can be completely reflected.

Despite all these studies, the behavior of tsunami waves over a canyon remains poorly understood and characterized. The purpose of this chapter is to examine the behavior of tsunami waves propagating over the Biobio submarine canyon by means of numerical simulations. The main task is to define the most important variables which influence the behavior of the tsunami. To do this, an idealized bathymetry was assumed, and thus the effect of the canyon can be isolated from other kind of effects. This bathymetry is based on the typical Chilean continental shelf and continental slope. Firstly a brief description of the study area is presented and then the numerical experiment set up is described. Next, the results of nearly 300 numerical simulations are discussed for several wave lengths, canyon widths, lengths and depths. The results were then also compared with tsunami behavior in other submarine canyons where either numerical simulations or field surveys are available. Through these results, it is possible to explain not only what typically happens in the area of Biobio but also improve the understanding of tsunami transmission over submarine canyons in other areas of the world.

a. Study area

The Biobio Canyon is located at the northern entrance of the Gulf of Arauco, just in front of the 2-km wide Biobio River. Figure 48(a) shows the location and shape of the canyon and Figure 48(b) shows two cross sections of the continental shelf, one at the northern side of the canyon and the other at the southern side. Both cases show that the

slope is almost uniform at both the trench and the continental shelf. The latter is estimated to have a width of 50 to 60km.

The canyon starts only 2km away from the river mouth and zigzags irregularly in an East-West direction along the continental shelf, with the end of the canyon (at the edge of the continental slope) being semi-circular in appearance. The canyon is characterized by having steep walls which practically divide the continental shelf into two parts. The length of the canyon is in the order of 130km, with a maximum width of 8.1km and a minimum of 3.2km. Sediments from the river and long shore currents formed a flat sandy area from San Pedro de la Paz to Bay of Coronel (Quezada, 2000). This area has also a series of dune systems parallel to the coastline, which reach a maximum ground elevation of 8m. However, behind the dunes the ground elevation is 5m in average, and there are some developed areas which are below 4m close to the Biobio River.

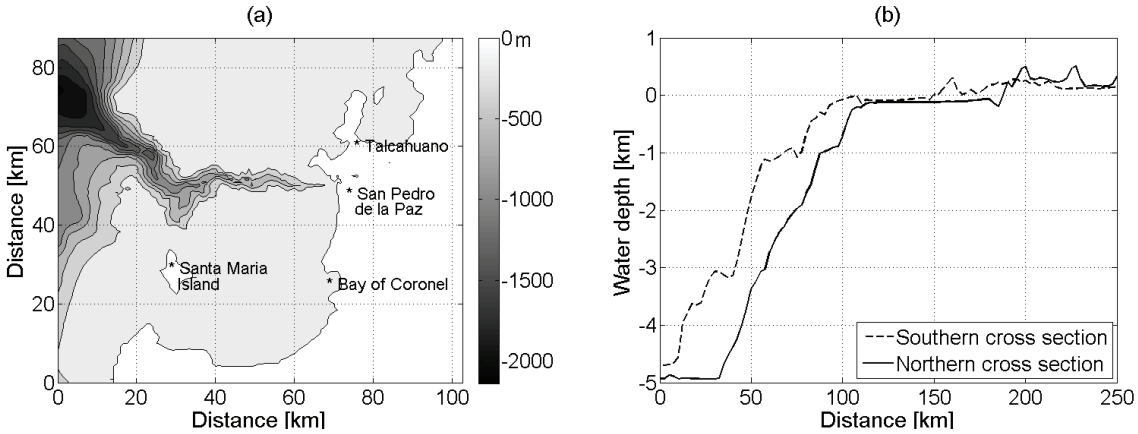

Figure 48. Bathymetry in the Gulf of Arauco and Biobio Canyon. (a) Plan view with contour lines every 200m.(b) Cross sections of the continental shelf (north and south sections of the canyon)

Figure 49 shows two pictures of the coastal zone between San Pedro de la Paz and Bay of Coronel. These pictures were taken on March 11th of 2010, approximately 7km south from the river mouth. It is possible to see that no traces of tsunami damage can be observed, and the fence and small house in the left hand side picture are intact. According to testimonies of people living at a 15-story building, located nearby to where these pictures were taken, the tsunami waves propagated in a north-south direction. This is in good agreement with the results given in Aranguiz (2011).

Figure 49. Pictures of the coastal zone between San Pedro de la Paz and Coronel Bay after the 2010 Chile tsunami.

b. Idealized Bathymetry

The analysis made in this work includes both the simulation of the tsunami source, its propagation and inundation. Due to the number of simulations, the numerical simulations in this chapter were carried out using the Tohoku University's Numerical Analysis Model for Investigation of Near-field tsunami (TUNAMI-N) code, which uses shallow water theory integrated in the vertical and the bottom friction is expressed as a function of Manning's roughness (Imamura et al., 2006). For this particular case a Manning's coefficient of $n = 0.025$ was selected, a typical value for a sandy bottom. The run up and inundation was calculated based on a moving boundary condition (Imamura et al., 2006). The use of this model is chosen over other models based on the water depth considered at the canyon and the trench. In addition, sensitivity tests showed that differences between NLSW and Bousinesq are negligible when long waves do not break, and differences in run up reach up to 10% when they break (Lynett, 2007)

The tsunami scenario utilized in this work was based on the 2010 Chile tsunami. As mentioned earlier, the rupture zone of this earthquake was 450 km in length and 150 km in width (Barrientos, 2010). The strike, dip and rake angles are defined as 15°, 18° and 110°, respectively (Deluois et al, 2010). A constant slip of 10m was assumed along the entire rupture zone in order to have a Mw=8.8 event. Subsequently, the depth and slip were modified such that the same initial wave height was obtained but different wave lengths were produced ($L_w = 188$, 230 and 290km). The initial free surface elevation was assumed to be equal to the seabed deformation given by the Okada (1985) formulation. Figure 50 shows the three scenarios simulated later in this chapter. The wave length here is defined as the length of the positive sea surface elevation, i.e. from the point where the sea surface is zero at the left side, and the point where the sea surface changes from positive to negative.

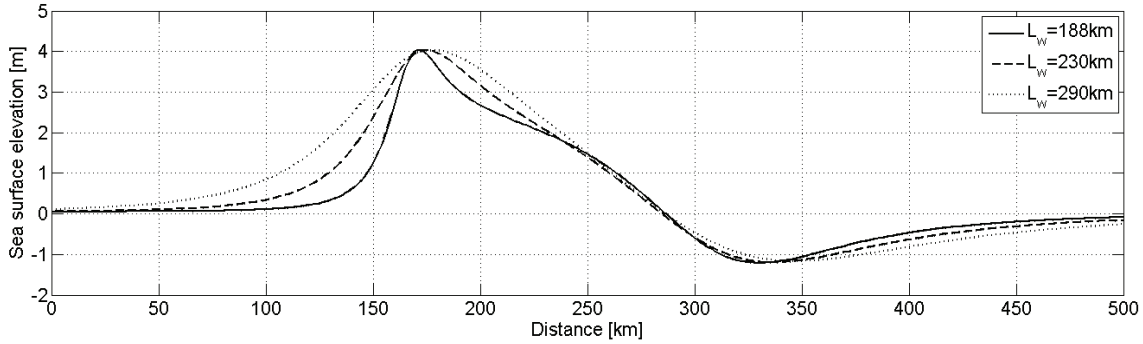

Figure 50. Initial condition of the three scenarios considered in the analysis

The numerical simulations were carried out over an idealized bathymetry based on the real bathymetry showed in Figure 48. The slope of the trench was defined to be 1/10 with a maximum water depth of 5,000m, while the slope of continental shelf was 1/410. The water depth at the transition point between the continental shelf and the continental slope was defined as h_0 =150m. The beach slope was modeled on typical beach profiles in the study area, which have slopes of around 1/200. Three canyon lengths were analyzed, namely L =20, 40 and 60km. In a similar manner, the Canyon width, B, was varied from 3 to 75km and the canyon depth, h, was also given a range of values from 100 to 1,850m. An example of the idealized bathymetry is shown in Figure 51. It shows the canyon variables used in the calculation as well as the trench, shelf and beach. The numerical simulations used four nested grids of 27, 9, 3 and 1" resolution. The location of these grids was selected mainly based on the Courant number, due to the fact that large water depths in the canyon give very large Courant numbers, especially for higher resolution grids. In order to analyze the time series and tsunami arrival time, a working gauge was defined at the coastline just in front of the canyon, i.e. at the river mouth.

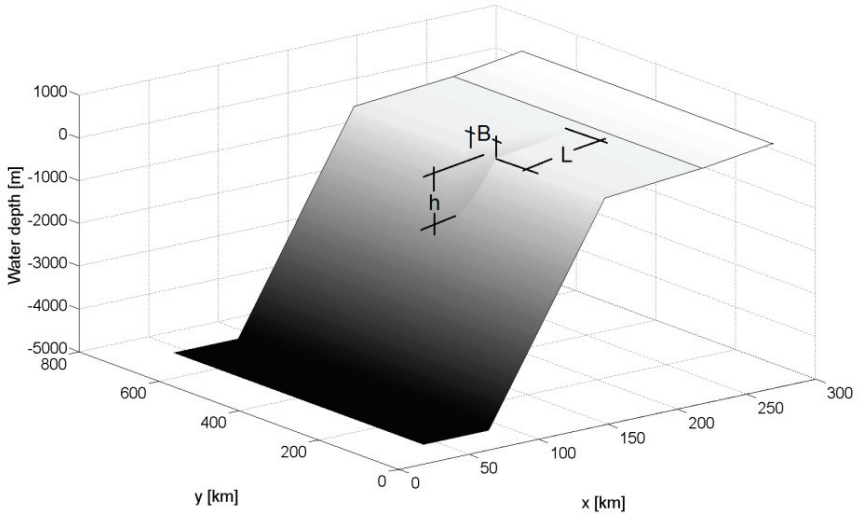

Figure 51. Idealized bathymetry of the Canyon and variables which define the size of the canyon.

The analysis in the following section is focused on runup and arrival time. All values obtained from the simulation with the presence of a canyon, are compared with the runup and arrival time without the canyon. Additionally, in order to better understand the effect of canyon width and canyon depth as well as tsunami wave length, a bathymetry with only half the canyon was considered, as shown in Figure 52. The main purpose of this bathymetry is to analyze the influence of an abrupt change in water depth on a tsunami wave front.

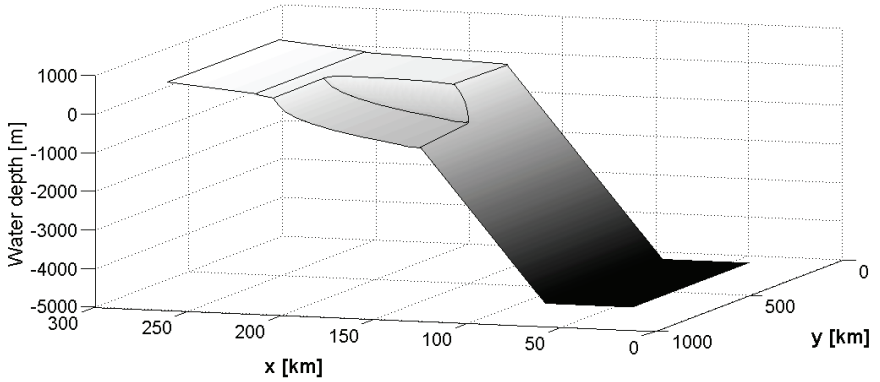

Figure 52. Idealized bathymetry with half of the canyon.

c. Effects of the Submarine Canyon on the runup

In this section the effect of the size of the submarine canyon is quantitatively assessed. As mentioned above, three tsunami wave lengths were tested for different lengths, widths and depths of the idealized canyon. In order to better visualize the

influence of the canyon, the results are presented as a function of the runup normalized by the runup without the canyon. Then, the influence that different widths and depths of the canyon can have on the runup is analyzed in detail, thus allowing for a relationship between the wave length and canyon width to be defined. Subsequently, the effect of the canyon on the wave amplitude along the coastline is also presented. Finally, other submarine canyons throughout the world are analyzed and compared with the present study case.

i. Effect on tsunami runup

Figure 53 shows the variation of the relative runup as a function of the canyon width, B, for several values of the canyon depth, h. These plots correspond to the case of a tsunami wave length $L_w = 230$km. These results are plotted for three different canyon lengths, namely, L =20, 40, and 60km. In general, it is possible to see that the runup is very sensitive to the canyon width. As B increases from zero (no canyon), the normalized runup decreases rapidly and reaches a minimum. Then, as B increases again the relative runup also increases but with a milder slope. This minimum value depends on the canyon depth and canyon length, the larger the length and depth, the lower the relative runup, and the smaller the width where the minimum runup is found. It is important to notice that the runup is also very sensitive to the canyon length. For instance, a wave propagating over a canyon with a depth of 200m and a length of 20km produces no effect on the runup. In other words, the tsunami wave does not feel at all the changes in the bathymetry. However, the same tsunami wave propagating over a canyon with a length of 60km and equal depth (200m) would have its runup reduced by up to 60% if the canyon width is 20km.

Therefore, it is possible to say that no matter the size of the canyon, the run-up in an area just in front of this canyon is always equal or lower than in the case without the canyon, i.e. the canyon does not increase the tsunami wave amplitude in a point located in front of the canyon. Nevertheless, It is important to take into account that the idealized bathymetry (V:H=1:10), gives a low reflection coefficient at the continental slope (Dereck, 1978). Steeper continental slopes would have higher reflection coefficients and lower transmitted waves, thus, part of the tsunami energy would be reflected and the rest would enter the canyon with no significant variation.

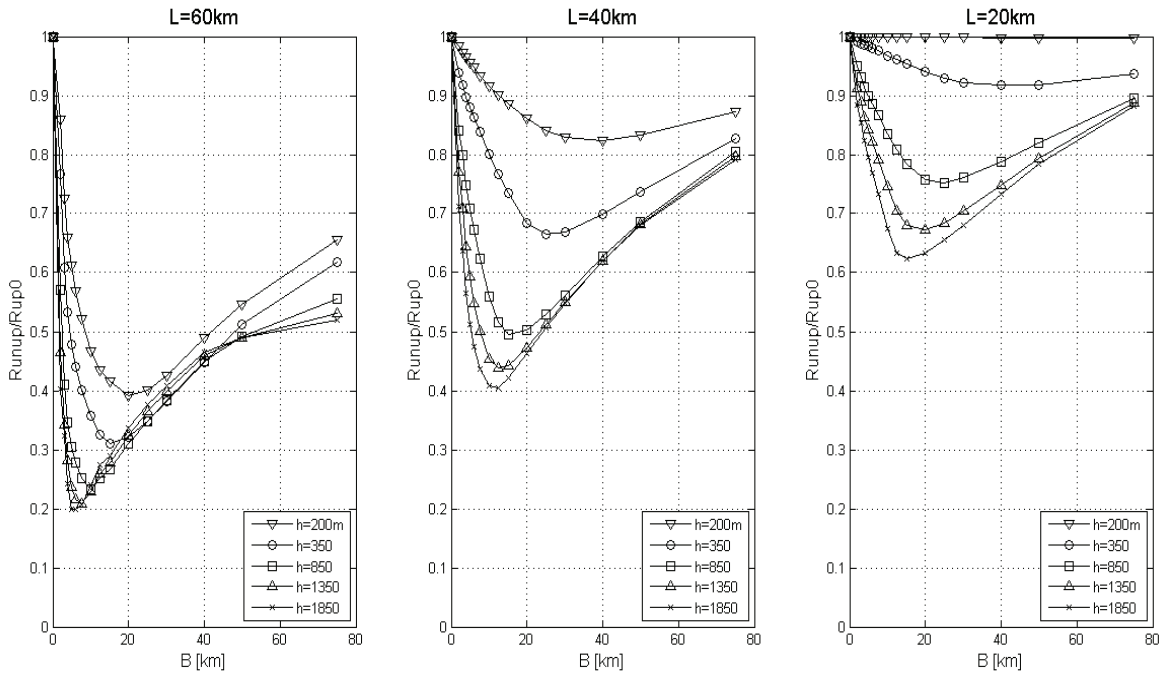

Figure 53. Normalized run up as a function of the canyon width and canyon depth. For three values of canyon length.

The previously described phenomenon can be explained as follows: the wave front suffers the shoaling effect as it approaches the continental shelf (Murata et al., 2010) and it experiences a diffraction process, similar to an incident wave in a submerged breakwater gap when enters the canyon (GIOC, 2000). In order to understand better what happens, the evolution in time of a wave front propagating over the bathymetry shown in Figure 53 should be considered. Figure 54 shows a tsunami wave front propagating from deep water to the continental shelf. In this case, the initial tsunami wave length was L_w =188m. The continental shelf was divided into two parts: the upper part ends at a water depth of 500m (canyon depth h=350m), while the lower part ends at a water depth of 150m. The x and y coordinates are normalized by the Tsunami wave length in order to analyze the influence of this. Ten minutes after the tsunami starts (T=10 min) the wave front is located at the water depth of 500m approximately, and there is no influence of any bathymetric feature on the wave front. However, ten minutes later (T=20 min) the wave front is affected by diffraction (such as a semi-infinite submerged breakwater) and refraction processes. The wave front divides into two main parts due to the different water depths and, subsequently different wave celerity. The wave front in the vicinity of the step changes its direction due to the diffraction-refraction process, and attempts to approach the canyon edge at a normal

angle. According to Mofjeld et al. (2000), the direction of the transmitted wave could be determined based on the incident angle and the refraction causes the transmitted wave to turn more normal. Now, if the same wave front propagates over a continental shelf which ends at a water depth of 1500m (a canyon depth of 1350m) in the upper part, a similar behavior can be observed (see Figure 55). However, the two wave fronts separate faster than in the previous case, and the incident angle of the wave in the deeper side would become more normal to the canyon edge, and thus the diffraction-transmission-refraction process would be enhanced. Therefore, a perpendicular-to-the-coast bathymetry change has two main effects on a wave front: (1) Diffraction process changes the wave direction in the vicinity of the canyon edge and (2) transfer of wave energy is in the form of a transmission-refraction process, thus a wave front propagates in a diagonal direction to the beach. Furthermore, it is possible to see that the longer the canyon length and deeper the canyon depth, the lower the wave amplitude within the canyon, as shown in Figure 53.

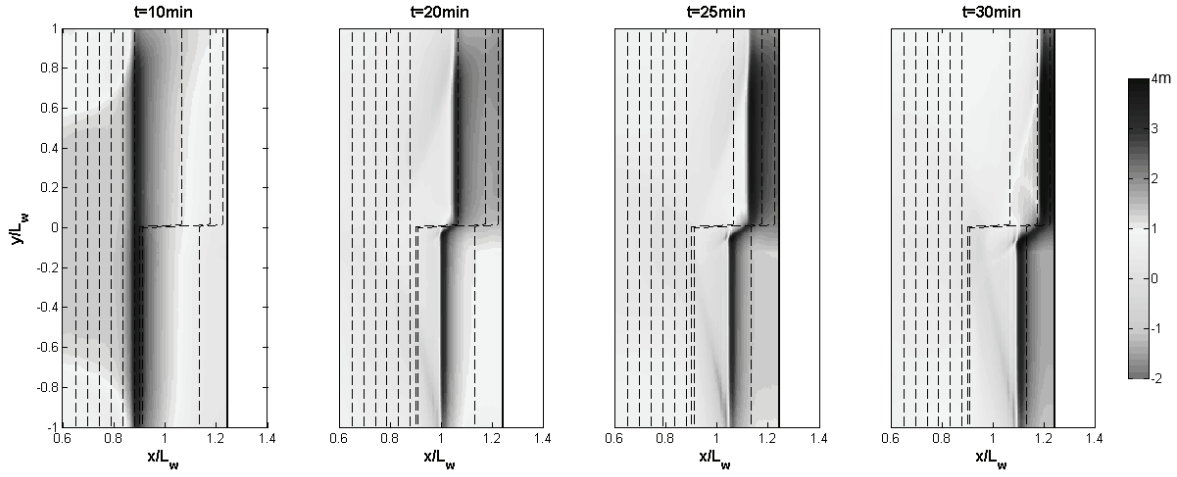

Figure 54. Snap shot of a wave front propagating over an abrupt bathymetry change perpendicular to the coast. The upper part of the bathymetry has a water depth of 500m (canyon depth of h=350m) at the transition point from the continental slope to the continental shelf, while the lower part has a water depth of 150m at the same point.

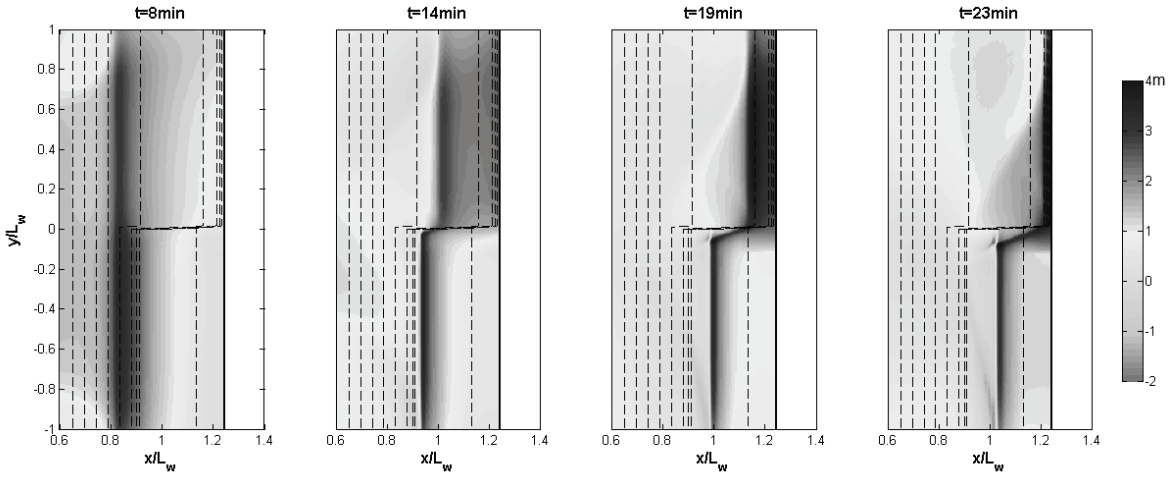

Figure 55. Snap shot of a wave front propagating over an abrupt bathymetry change perpendicular to the coast. The upper part of the bathymetry has a water depth of 1500m (canyon depth of h=1350m) at the transition point from the continental slope to the continental shelf, while the lower part has a water depth of 150m at the same point.

Now, the wave fronts shown in Figure 54 and Figure 55 can be plotted in the way in which a person at the beach would see them approaching the coast, thus showing the evolution of the wave front at each side of the step. Figure 56 shows the evolution in time of these wave fronts for two different values of h. The figure includes wave fronts of a tsunami wave length of both $L_w = 188$m and 290m. The zero in the horizontal axis represents the location of the change in bathymetry. The negative side corresponds to the shallower water, while the positive direction represents the deeper part of the continental shelf. In both sides of the figure, the wave front at the right hand side increases faster in height due to the shoaling effect and wave celerity. It does not mean the wave amplitude that will reach the coastline will be higher, but rather that the wave front at left hand side travels slower, as seen in Figure 54 and Figure 55. The most important feature of Figure 56 is the transition between the left and right sides of the wave front. For time T=10 min and T=8 min for the case of 500 and 1500m water depth, respectively, there is no significant shoaling effect. However, 10 minutes later in the first case (T=20 min), and 6 minutes in the second case (T=14 min), there is a small change in the vicinity of the step: the left side increases and the right side decreases, but beyond this area the wave fronts remain the same. As a matter of fact, this area corresponds to the wave front being affected by the diffraction-transmission-refraction process described above. The decrease in the wave amplitude is due to the diffraction process and enlargement of the wave front, while the increase is due to the shoaling process after refraction of the transmitted wave. In fact, the transmission coefficient can be as large as twice the incident wave (Levin and Nosov, 2009). The most important

issue here is that the influence area due to diffraction is related to the tsunami wave length. Actually, this area is limited by $(x/L_w) < 0.1$, and beyond this distance the step has minor effect on the wave front. On that ground, the width of a submarine canyon will be quite important for the wave amplitude within the canyon: The narrower the canyon, the lower the wave amplitude. On the contrary, if the canyon width is too large ($B > 0.1L_w$) the wave amplitude decreases in the vicinity of the canyon edge but increases in the inner part of the canyon, and subsequently, the wave approaching the coast will be also higher. This is the reason why the plots in Figure 53 shows to have a minimum relative runup for a certain value of canyon width, and then increases as B increases too.

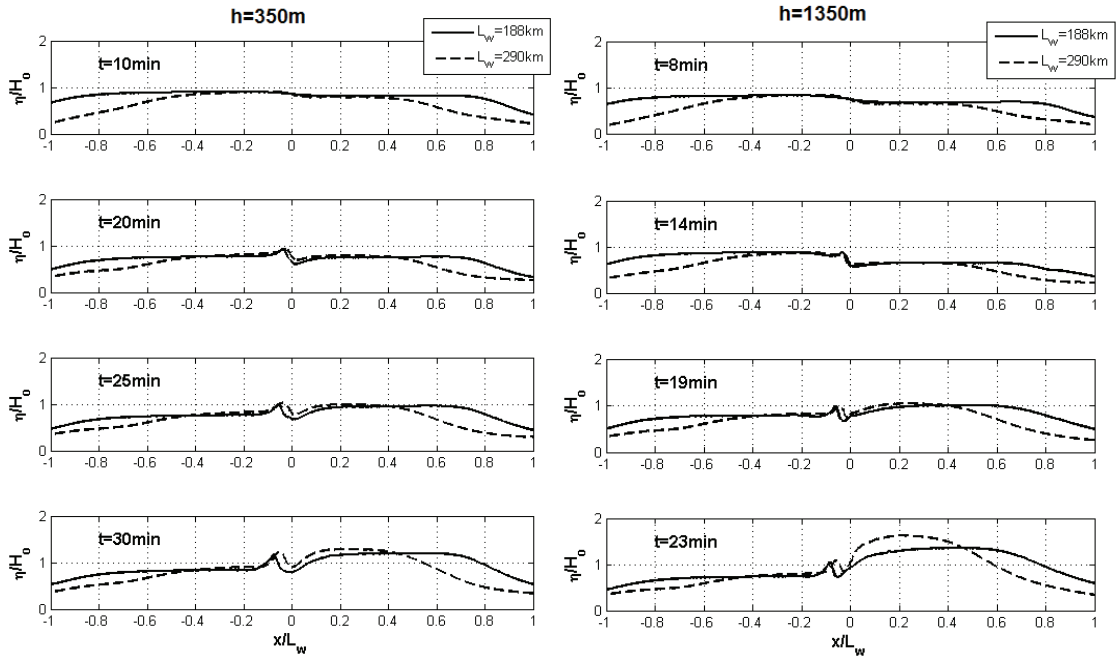

Figure 56. Evolution of the wave fronts over a bathymetry change parallel to the wave direction

Figure 57 shows the influence of the wave length on tsunami propagation and runup for the bathymetry shown in Figure 51. This analysis is done for three different tsunami wave lengths and two canyon depths, namely h =350 and 1350m. The left hand side corresponds to the case of a canyon length L =40km, while the right hand side to a canyon length of 60km. It is possible to see that normalized runup depends not only on depth and the length, but also on wave length. Larger wave lengths have lower reduction coefficient mainly at shallower canyons. When longer wave lengths interact with shallower water, the shoaling process results in higher wave amplitudes, as seen in Figure 56, due to the fact that the wave amplitude is proportional to the fourth power of the wave length. However, the wave celerity is the same, thus the diffraction-

transmission-refraction process does not decrease the wave height at the same rate. In addition, short canyons do not allow enough transfer of wave energy so that the waves inside the canyon can decrease in amplitude. On the other hand, deep canyons reduce the shoaling effect; subsequently, the wave height inside the canyon is much lower than in the previous case. Moreover, the wave front inside the canyon propagates faster such that the wave amplitude decreases at an even higher rate. Furthermore, a long canyon allows more wave refraction and thus all curves almost collapse into a single curve, as seen in Figure 57.

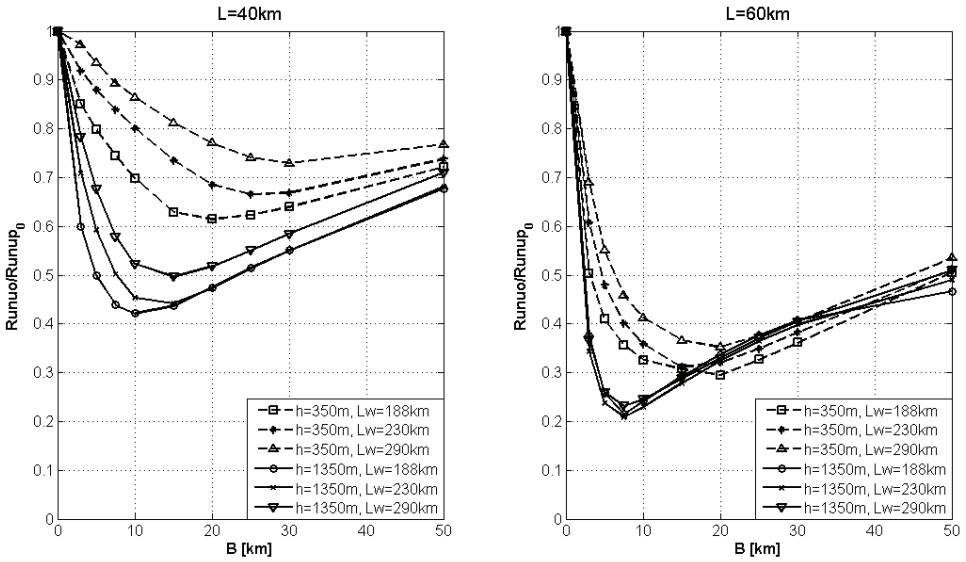

Figure 57. Normalized runup as a function of the canyon width for several tsunami wave lengths and two different canyon depths.

ii. Effect along the coastline

Up to now, the effect of a submarine canyon has been described only for a point located just front of the canyon. Since the tsunami wave starts to diffract when it enters the canyon, and then refracts propagating away from the canyon, as seen in Figure 55, the influence of the canyon on the incident tsunami wave along the coastline will be felt differently. Figure 58 shows the maximum amplification factor of the sea surface elevation due to the presence of the canyon for a canyon of width $B = 10\text{km}$, and height $h = 1350\text{m}$. This factor is calculated with respect to the maximum sea surface elevation obtained for the bathymetry without the canyon. Thus, a factor of 1 represents no change, while a factor of 2 would represent an amplification of 100% in the wave amplitude. The left hand side corresponds to a canyon with a length of 40km while the right hand side shows a canyon with a length of 60km. In addition, the upper part is for

a wave length of L_w =188km and the lower part for wave length L_w =290km. The x and y distances have been normalized by the width of continental shelf, W_0. The figure shows that the wave diffraction and refraction due to the canyon generate concentration zones in the coastline at each side of the canyon. In addition, the size of this area depends on neither the canyon length nor the wave length, but the width of the continental shelf. In fact, the figure shows that the maximum wave amplitude takes place at approximately half the width of the continental shelf from the center of the canyon. In all cases the wave amplitude in front of the canyon is reduced, and it increases as one moves away from the canyon.

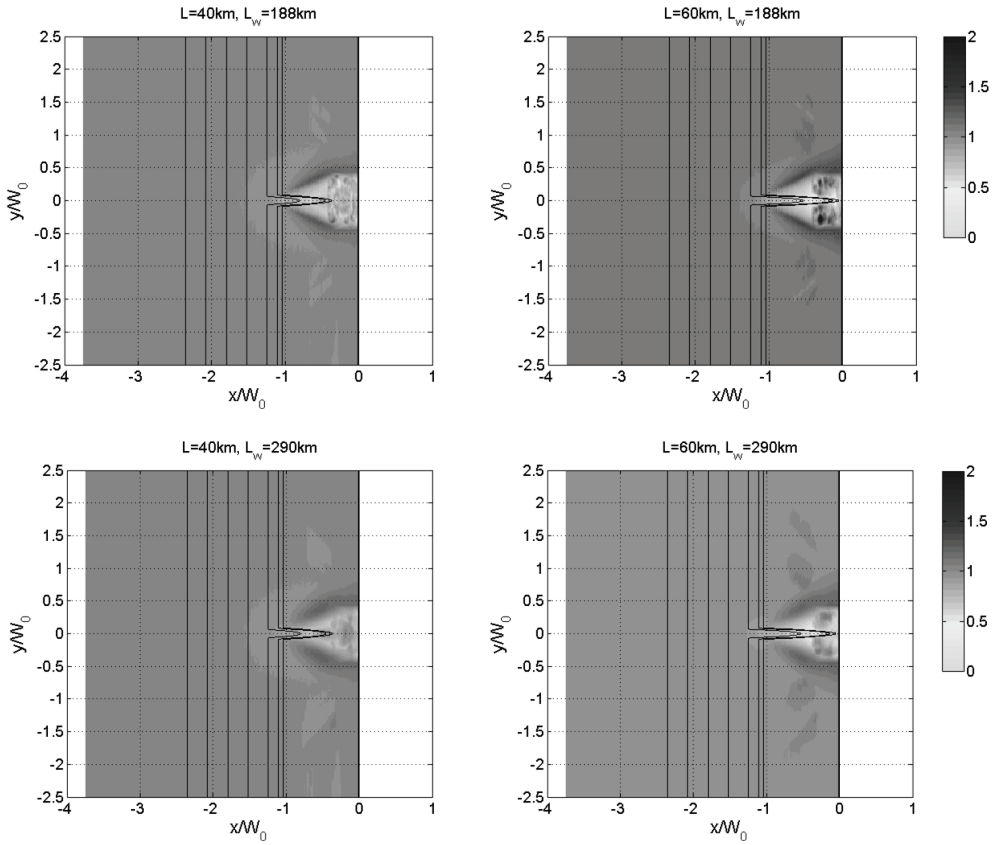

Figure 58. Amplification factor of the sea surface elevation with respect to the case of no submarine canyon.

However, it is important to note that the wave length has an effect on both the maximum and minimum wave amplitudes along the coast. Actually, a short wave length generates higher wave amplitude at the concentration zone but lower wave amplitude in front of the canyon. As explained earlier, tsunamis with shorter wave lengths are more affected by submarine canyons (see Figure 57) and have lower relative runup in front of the canyon. In addition, the effect of the canyon length, and the distance between the canyon end and to the beach is also important, due to the fact that the wave amplitude in

front of the shorter canyon (longer distance to the coast) is higher than in the case of a longer canyon, as the shoaling process can increase the wave amplitude when leaving the canyon.

iii. Effect on tsunami arrival time

Another important aspect of tsunami propagation is the arrival time. Figure 59 shows the time series of a gauge located at the coastline just front of the end of the canyon. The upper frame corresponds to a canyon depth of 200m (at a total water depth of 350m) while the lower frame is for a canyon depth of 1350m. In both graphs the case without canyon ($B = 0$) is plotted for comparison. As expected, the tsunami wave does not decrease the celerity within the canyon, therefore, tsunami waves arrive earlier than in the case without a canyon. It is interesting that the wider the canyon the faster the tsunami wave propagation, and this fact is more evident for deeper canyons. As described in previous sections, the wave front within the canyon is affected by the diffraction-refraction processes, and the most important effects are in the vicinity of canyon edges ($x < 0.1L_w$). Therefore, with large values of canyon width the wave front in the inner part of the canyon propagates without significantly being affected by this process.

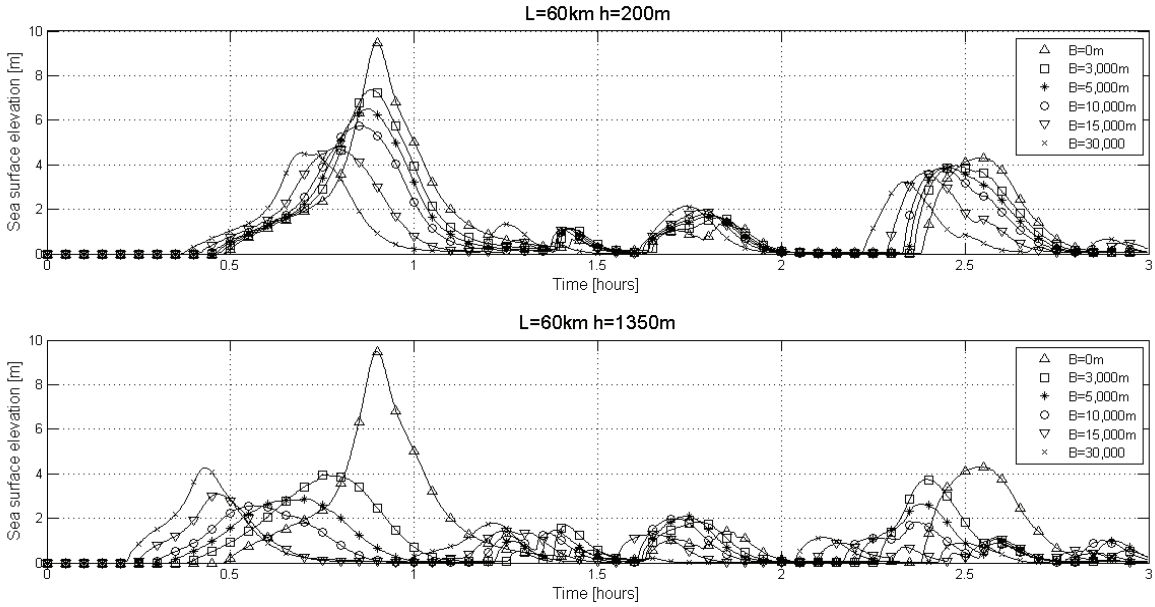

Figure 59. Time series of the sea surface elevation at the coastline in front of the canyon for a canyon length of 60km.

Figure 60 shows the time series for a canyon with a length of only 20km. The differences with the previous cases are evident. For shallower canyons all curves collapse into a single one, which means that the canyon width does not have any

influence on tsunami propagation. For the case of a deeper canyon, even though tsunami arrival time decreases, the effect is not significant, demonstrating again that short canyons do not greatly influence tsunami propagation.

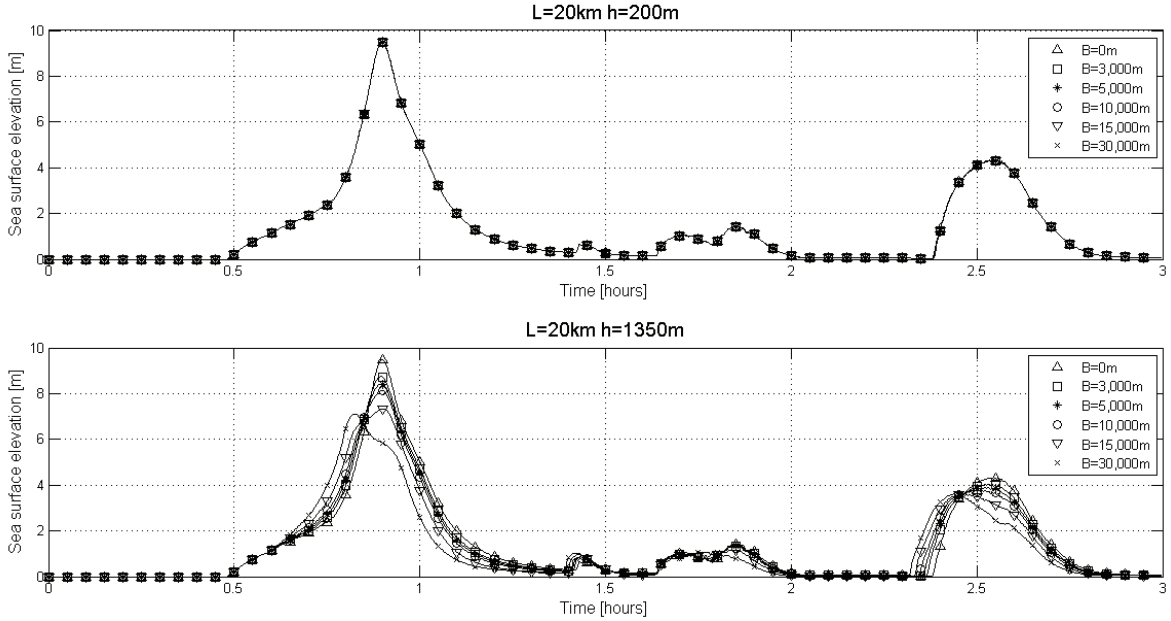

Figure 60. Time series of the sea surface elevation at the coastline in front of the canyon for a canyon length of 20km.

d. Tsunami propagation over other submarine canyons

Jinadasa (2008) correlated tsunami wave runup in Srilanka with nearshore bathymetry for the 2004 India Ocean tsunami. In his work, Jinadasa (2008) describes the continental shelf of Sri Lanka as narrow with an average width of 21km and an average depth of 200m, while the continental slope is 1:1, which corresponds to a slope of 45°. The study concluded that places where canyons are located were severely damaged due to a funneling effect. However, a closer look at Figure 53 shows that a submarine canyon with a length of 20km, similar to the canyons in Sri Lanka, has a limited effect on tsunami run-up, and that more attention should be paid to the continental slope instead. The analysis given by Goring (1978) allows to estimate that a high reflection coefficient can be produced due to this steep slope, and subsequently, that a lower amount of wave energy would be transmitted through the continental shelf. Therefore, from the results of the present research, it can be concluded that the crucial point in this case is that the relative high runup in front of the canyon was not generated by the canyon itself, but that the low runup beside the canyon was caused by reflection in the continental slope, which makes the values in front of the canyon seem higher.

Ioulalen et at. (2007) analyzed the 2004 Indian Ocean Tsunami and its impact in the Bangladesh. In this case, there is a submarine canyon located in front of the Bangladeshi coast, which runs in a NE direction and starts at around 25km south of the coast along the continental shelf. The length of the canyon is in the order of 140km, with maximum depth of 1200m and 20km in width. The width of the continental shelf varies from 140km to 170km. The simulations of Ioulalen et al. (2007) reproduced well field observation, which indicate a weak tsunami impact, with average wave amplitude of 1m. Their simulation also showed that north and eastward the canyon the wave amplitude is larger off the coast and distributed sparsely within the shelf. The main feature they found was that along and within the canyon the amplitude is low because of the deep waters, while in the area surrounding the canyon the amplitude is higher because of shoaling (Ioulalen et al., 2007). They also observed that the maximum wave amplitude took place front of Barisal, which is located some 70km east of the canyon end. This result is in good agreement with the behavior given in Figure 58 such that there is a wave amplitude concentration zone. Nevertheless, Ioualalen et al. (2007) also reported high wave amplitude just front of the canyon, which is possible since the end of the canyon is located 25km off the coast, and thus the shoaling process can occur and amplify the wave leaving the canyon. Furthermore, the canyon end section is not exactly perpendicular to the coast, and thus the amplitude concentration zones could be displaced, and subsequently, it could give the impression that the maximum wave amplitude occurs in front of the canyon.

The results reported by Ioulalen et al. (2007) in the Bangladeshi coast follow the behavior described in the present research. Nevertheless, it is also important to take into account that the shape of the Bay of Bengal and the wide continental shelf could propagates edge waves which are important in tsunami behavior (Yamazaki et al.,2011). Also, the nature of the sediments in the area (often made of mud) could have had an important influence in the propagation and dissipation of the tsunami wave, though this effect is currently poorly understood. Thus, the results for the case of Bangladesh should be viewed with caution.

Another case worth being analyzed is that of the San Antonio Canyon, which is located in front of San Antonio Harbor in Chile (71°37’S, 33°36’W). The width of the continental shelf here is only 30km, half of the one in the Region of Biobio, however, the canyon termination reaches the coast and practically enters the harbor. The width of the canyon is in the order of 15km while the depth is 1000m. Field surveys showed that

6km south from the Harbor (at Santo Domingo) the run up was 4.8m, and 19km south an inundation height of 5.2m was measured, while 5km north (at Cartagena) the inundation height was 4m (Fritz et al., 2010). However, the observed behavior of the tsunami inside the harbor are different; the southern breakwater was overtopped and the flow depth was only 1m, while inside the Harbor basin the surge was only 2m, affecting only some fishing vessels (Concejo Municipal, 2010). The information given by the Mayor of San Antonio city also mentioned seawater surging into Maipo River, which is located 4km south of the Harbor. Therefore, the wave amplitude distribution in this area was also highly influenced by the presence of the submarine canyon, and the higher runup measured at each side of the canyon was due to the concentration zones depicted in Figure 58.

From the previous paragraphs, it is seen that the distance from canyon end to the coast also takes an important role in tsunami defocusing and wave amplitude reduction. A particular case would be a "canyon" arriving right up to the land itself, such as in the cases of fjords, rias or estuaries; however in this case the behavior will differ from the phenomenon described in this research. In this case, the shoaling effect is significant and tsunami waves propagate long distances without wave energy being transferred laterally, and hence large runup can be expected at the coastline (Didenkulova and Pelinovsky, 2010; Choi et al., 2008). Examples of this phenomenon can be seen in the work of Shimozono et al. (2012) about the effect of the 2011 Tohoku Tsunami on the Sanriku coast, where tsunami height exceeding 20m in V-shaped bays were reported, and an extreme value of 35m was measured. The analysis of such type of geographical formations, however, is out of the scope of the present work.

e. Numerical simulation of 2010 tsunami over Biobio Canyon

In this subsection, the propagation of the 2010 Chile tsunami over the Biobio Canyon is analyzed considering now the real bathymetry given in Figure 48. The same TUNAMI model is used and 4 nested grids of 27, 9, 3 and 1" resolution were defined. In order to compare the tsunami behavior, three tsunami initial conditions were tested. The first case considered a planar fault model (PFM) or uniform initial condition used in previous sections, while the others two cases are Finite Fault Models (FFM) given by Lorito et al. (2012) and Hayes(2010). Figure 61 shows the initial condition and the sea surface elevation over the Biobio Canyon for all cases. From the snapshots shown at the right hand time frames in Figure 61, it is clear that the bathymetry influences tsunami

propagation. Even though initial sea surface elevations are completely different, all cases show a similar pattern, thus the behavior of the wave front agrees well with the results given in subsection 4.1., showing how the wave refracts and changes direction. In addition, Santa Maria Island enhances this effect due to its effect as a barrier and the diffraction process that occurs after it, resulting in the wave front propagating from north to south in the Gulf of Arauco (Aranguiz, 2012). This behavior is identical to the one described in Aranguiz (2011) for the non-uniform initial conditions of both the 1960 and 2010 tsunamis. Moreover, it is in agreement with the testimony of local people who observed the 2010 Chile tsunami at this location, interviewed during field surveys.

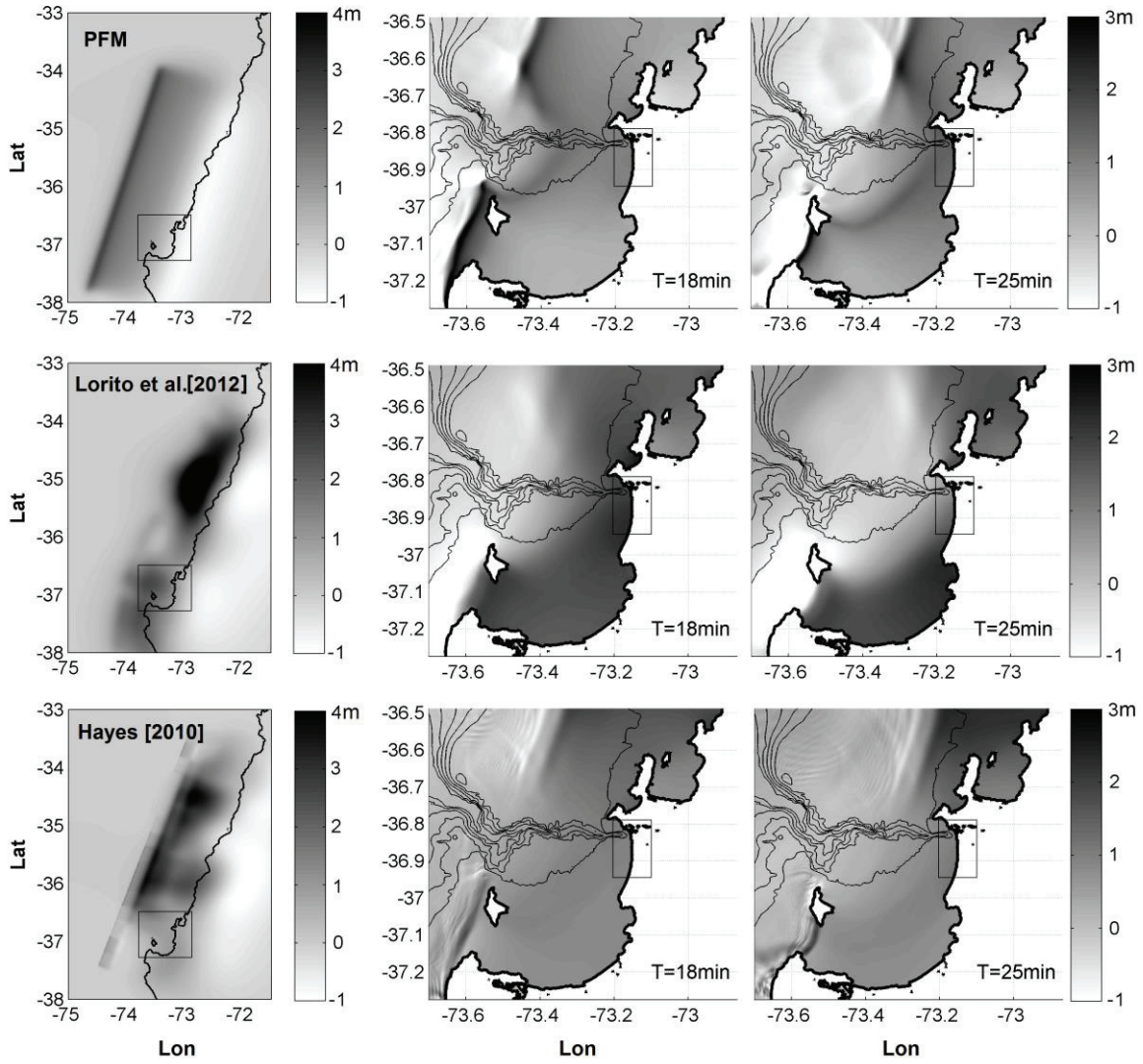

Figure 61. Numerical simulation of the 2010 Chile tsunami over the Biobio Canyon. Left frame shows the initial conditions. Right frames show snapshots of the tsunami propagation at 18min and 25min after the earthquake. The thin lines in the map represent the bathymetric contours.

Finally, the tsunami wave amplitude and inundation areas obtained from the numerical simulation at the study area (rectangles in Figure 61) are shown in Figure 62. The 50m bathymetric contour lines are also plotted in the figure. From the Figure, it can be seen that all tsunami scenarios show to have low inundation heights in the river (~2-3m) and generate areas were the tsunami wave amplitude is concentrated at both sides of the canyon. However, the FFM given by Lorito et al. (2012) showed to have higher tsunami amplitudes in the whole domain. A detail analysis of this case demonstrated that large tsunami amplitudes are due to edge waves propagating from the mayor slip patch located north of the epicenter, rather than the southern slip patch, which is located front of the Gulf of Arauco.

One of the most important feature is that the length, width and depth of the Biobio Canyon correspond to the values which give the lowest run up in front of the canyon head, as shown in Figure 53.

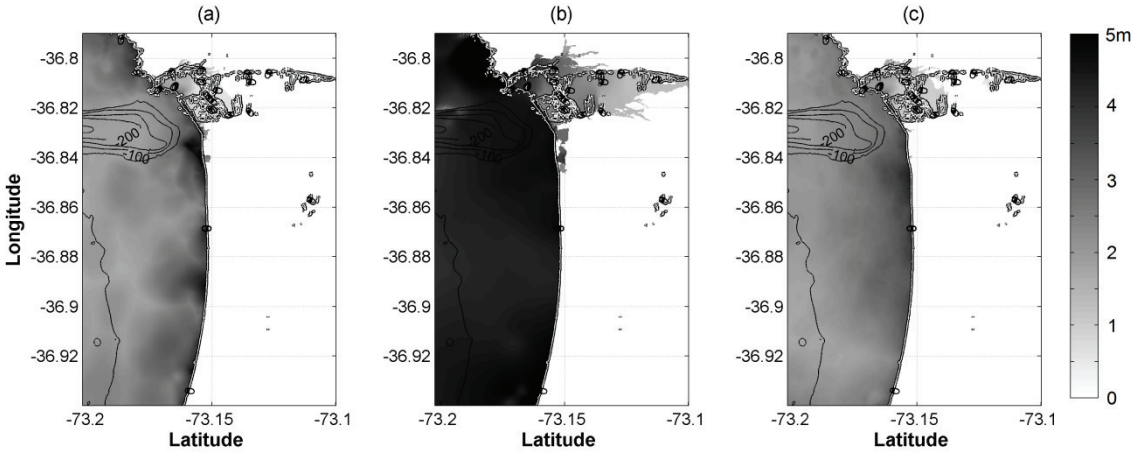

Figure 62. Tsunami wave amplitude and tsunami inundation area obtained from numerical simulation of 2010 Chile tsunami over real bathymetry. (a) Planar Fault Model. (b) Finite Fault Model from Lorito et al. (2012). (c) Finite Fault Model from Hayes (2010).

f. Discussion

The present chapter gave a general understanding of tsunami behavior over submarine canyons. These kinds of bathymetry shapes have strong influence on tsunami propagation and run up. It was found that most important variables which influence the tsunami propagation are the length and width of the canyon and less important, but not negligible, the depth. Submarine canyons result in a transfer of wave energy from the

area inside the canyon onto the area on top of the continental shelf to the sides of it. They primarily induce a diffraction effect on the wave front and then, since the wave front within the canyon approaches in a direction more normal to the canyon edges, the refraction causes the transmitted wave to turn even more normal to the canyon edge. Therefore, the transmitted wave front propagates in a diagonal direction to the coastline, thus a decrease in runup in front of the canyon and a spatial variation of the inundation height is observed along the coastline.

The numerical simulation of the 2010 Chile tsunami over the Biobio Canyon showed to be in good agreement with the tsunami behavior over the idealized bathymetry. The submarine canyon decreases the wave amplitude at the area behind the canyon, such that amount of sea water surging into the river is greatly reduced. In addition, it was found that the presence of Santa Maria Island enhances the diffraction process and the bathymetry within the Gulf of Arauco, thus the refraction process is also enhanced. Therefore, both the submarine canyon and the Santa Maria Island cause the wave front rotate in a clock-wise direction generating a greater effect in the southern shore of the Gulf, which is in good agreement with the field survey and numerical simulations given in sections 3.1 and 3.2

On the contrary of what was concluded by Jinadasa (2008) and Ioualalen et al. (2007), who reported amplification due to the submarine canyons in Sri Lanka and Bangladesh, respectively, it is possible to find some patterns which explain the those behavior as a function of the length and width of the canyon. The results of the present chapter do not contradict the statement of these authors, on the contrary, it gives more information to better understand the tsunami behavior. However, it is believed that other variables such as the steepness of the continental slope, the direction of the canyon with respect to the coast and the waves trapped in the continental shelf could influence also the tsunami behavior.

Chapter 4 Effect of possible future tsunamis

Scientific research has demonstrated that there is a seismic gap in the Arica-Tocopilla source region in Chile. Historical records of large earthquakes in this rupture zone assign it a return period of 111±33 years (Comte and Pardo, 1991). If the rate of moment deficit is taken into account, the seismic potential over the 1877 rupture area in 135 years equals an earthquake of minimum moment magnitude Mw~8.6 (Chlieh et al., 2011). The last event took place in 1877, and this event generated a destructive tsunami that affected not only the Chilean coast but also ports in the United States, New Zeland and Japan (Soloviev and Go, 1975). The ports located inside the Arica-Tocopilla source region suffered severe damage with a mean inundation height of 10m. The tsunami was also recorded at ports in central Chile (Lat 33S to 37S) such as Valparaiso and Talcahuano. The latter is located inside the Bay of Concepcion and 1,500km from the 1877 tsunami source area. On that ground, the analysis of possible future tsunamis which could affect the Bay of Concepción should be also analyzed. To do this, a tsunami forecast model at Talcahuano for hypothetical Arica-Tocopilla earthquakes is developed. This section is part of a journal paper published by Aranguiz et al, 2013.

Forecast models require pre-computing earthquakes events along potential earthquakes zones as well as deep ocean buoys to detect and estimate tsunami sources in real time. As an example, the NOAA Center for Tsunami Research (NCTR) has developed an operational tool that provides tsunami forecasts known as the Short-term Inundation Forecast for Tsunamis (SIFT) (Gica et al., 2008). This model uses 1160 pre-computed unit sources along the Pacific, Atlantic and Indian Oceans, and it can provide offshore forecasts of tsunami computed waveforms quickly at any specific site, though DART buoys and data inversion techniques are required. In a similar manner, The Japan Meteorological Agency (JMA) is in charge of the tsunami warning system in Japan. The model they used is based on hypocentral parameters such as location, depth and magnitude, and the tsunami-simulation database system which stores more than one hundred thousand cases of previously-conducted tsunami-propagation simulation results (Ozaki, 2011). The system also uses 12 GPS buoys and 172 tidal gauges for changing grades and areas of tsunami warnings/advisories.

Unfortunately, a forecast model like the ones mentioned above cannot be implemented in Chile yet, due to the fact that none of the required infrastructure is available along the Chilean coast at present (such as pre-computed earthquakes events

and DART or GPS buoys). Therefore, the development of a forecast propagation model could be very important in tsunami warning and evacuation plans. The main purpose of this chapter is to put forward a simple forecast model for Talcahuano. This model considers the magnitude of the earthquake, focal depth and tidal level. Through these results, it is possible not only to understand the possible effect of tsunamis from the north of Chile on the Bay of Concepción, but also allow local authorities in Talcahuano to issue domestic tsunami warnings knowing maximum tsunami heights and arrival times and to be focused on the most affected areas

4.1.Seismic gap and expected tsunami

Figure 63 shows the relevant seismic activity in Southern Peru and Northern Chile. South of the 1877 rupture zone, the 1995 Antofagasta earthquake (Mw8.1) had an extension of 180km, approximately. In addition, the 2007 Mw=7.7 Tocopilla earthquake ruptured the deeper portion of the seismogenic zone, realizing only a 4% of the moment deficit (Chlieh et al., 2011). In a similar manner, historical records show that in 1868 an earthquake with an estimated magnitude 8.8 affected the south of Peru, which had a rupture zone 450km in length, approximately. This zone could have also been activated in 1604 and 1784, with an extension similar to the 1868 event. On that ground, it is important to take into account the 2001 Arequipa earthquake (Mw 8.4), located in the northern part of the 1868 rupture zone. This earthquake partially filled the seismic gap in southern Peru (Ruegg et al., 2001) reaching the latitude of the city of Ilo (17,65°S), leaving the southern segment unbroken. Therefore, it can be said that the zone between Ilo and Tocopilla has not had "relevant" seismic activity the since 1877.

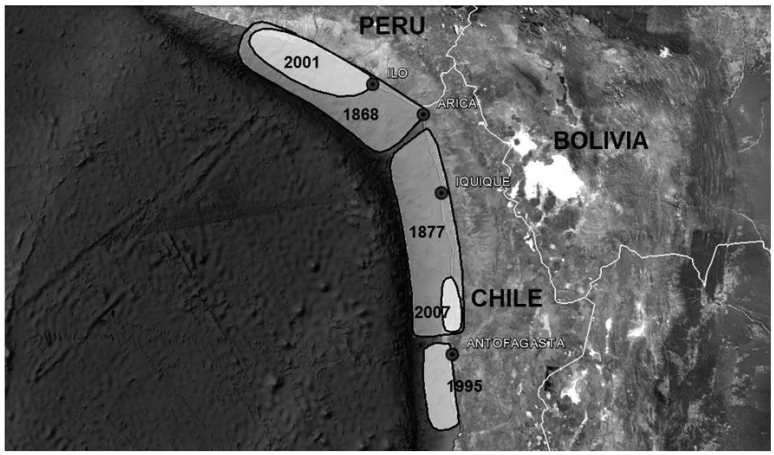

Figure 63. Rupture areas of the last 4 relevant earthquakes of 1868, 1877, 1995 and 2001 in Southern Peru and Northern Chile.

4.2. Fault models for hypothetical Arica-Tocopilla earthquakes

This forecast model gives the maximum sea surface elevation at the Talcahuano tide gauge located inside La Poza (36.71°S, 73.11°W), as a function of earthquake magnitude, tide level and focal depth. The forecast model was developed from five different moment magnitudes, Mw=8.0, 8.2, 8.4, 8.6, and 8.8, and the fault models were defined by means of theoretical and semi-empirical relationships between magnitude and fault parameters. In addition, the model implements tide effects with static sea level change from -0.5m to 1.2m.

Numerous studies relate magnitude and seismic moment with fault parameters such as length, width and average slip. These empirical relationships were derived from reliable data using least square regression method (Wells and Coppersmith, 1994). The studies also show that the regional setting has no influence on the relationships between the moment magnitude and the source dimensions, however there is a dependence on the slip mechanism type (Vakov, 1996). Haiyun and Xiaxin (2003) proposed simplified semi-empirical relationships for engineering and scientific practice which also considered slip type. They used the same database of Wells and Coppersmith (1994) in addition to nine historical earthquakes that occurred after 1993. However, the magnitude of the analyzed events is restricted to Mw< 7.7. For larger earthquakes, Papazachos et al. (2004) presented global empirical formulas which relate the fault parameters with the moment magnitude in dip-slip faults in subduction zone. The empirical formulas are compared with historical earthquakes in the Chile-Peru subduction zone to select the best-fit fault length and width. Six events with moment magnitude higher than 7.5 were selected for the study shown in Table 5.

Table 5. Magnitude and estimated rupture area of large earthquakes in the Chile-Peru seismic zone.

Name	Mag. Mw	L (km)	W (km)	Source
1960 Valdivia earthquake	9,5	1000	200	Barrientos, (1991)
1974 Peru earthquake	8.1	200	50	Wyss, (1979)
1995 Antofagasta earthquake	8.1	180	60	Guiborg et al (1997)
2001 Arequipa earthquake	8.4	300	100	Bilek and Ruff, (2002)
2007 Tocopilla earthquake	7.7	130	40	Peyrat et al, (2010)
2010 Cauquenes earthquake	8.8	450	150	Barrientos, (2010)

Figure 64 shows the plot of the empirical formula given by Papazachos et al. (2004) and Haiyun and Xiaxin (2003) together with the over Mw7.5 historical earthquakes in Table 5. From this it can be seen that the fault length computed with the Papazachos et al. (2004) formula is in very good agreement with the rupture length of the selected earthquakes, even for the largest recorded earthquake in 1960, while the formula given by Haiyun and Xiaxin (2003) underestimates the fault length for earthquakes larger than Mw8.0. With respect to the fault width, it is possible to see that the Papazachos et al (2004) formula agrees well with earthquakes larger than Mw8.5, however, it overestimates the fault width for smaller earthquakes. On the contrary, the Haiyun and Xiaxin (2003) formula gives good estimation of the fault width for earthquakes of magnitudes up to Mw9.0, despite the recommended magnitude being only for the range 7.0<Mw<7.7.

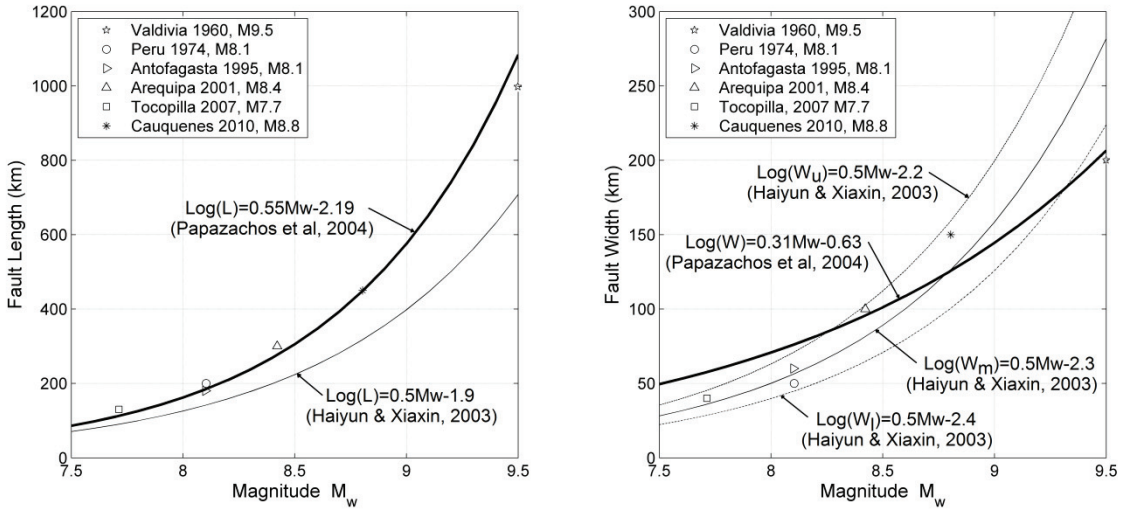

Figure 64. Relationships between the earthquake magnitude and the size of the rupture area.

The following analysis estimated the fault length from the equation given by Papazachos et al. (2004), while the fault width was estimated from the Haiyun and Xiaxin (2003) formula. Since the later equations include upper and lower bounds, three values of fault width were included in the analysis. Then, the fault slip was computed from the given moment magnitude and fault length and width estimated from the given equations. The other parameters such as strike, rake and dip were assumed to be constant and equal to 0°, 100° and 19°, respectively. Table 6 shows the fault parameters of all selected scenarios. In addition, all these scenarios considered several focal depths, which also changed the longitudinal coordinate due to the subduction zone. Large

earthquake had a minimum focal depth of 25km, while smaller earthquake had a focal depth as shallows as 10km. In all cases, the maximum focal depth was defined to be 50km. The table also shows the minimum and maximum depth of the upper side of the rupture area. A total of 114 numerical simulations were carried out in order to analyze both the size and depth of the earthquake.

Table 6. Source parameters used for the tsunami forecast model.

Magnitude	*L (km)*	*W (km)*	*D (m)*	*Min Focal Depth (km)*	*Min upper side depth (km)*	*Max upper side depth (km)*
8.0	160	63	4.1	20	9.7	39.7
		50	5.2	10	1.9	41.9
		40	6.5	20	13.5	43.5
8.2	210	80	5.0	20	7.0	37.0
		63	6.4	15	4.7	39.7
		50	8.0	20	11.9	41.9
8.4	270	100	6.2	20	3.7	33.7
		80	7.8	15	2.0	37.0
		63	9.8	20	9.7	39.7
8.6	350	125	7.6	20	1.0	29.7
		100	9.6	20	3.7	33.7
		80	12.0	20	6.9	37.0
8.8	450	160	9.3	25	1.0	24.0
		125	12.0	25	4.7	29.7
		100	15.0	25	8.7	33.7

4.3.Forecast Model

Figure 65 shows the maximum wave amplitude at Talcahuano tide gauge for all tsunami scenarios defined in Table 6, which have several earthquake magnitudes, rupture widths and focal depths. To validate the present forecast model, the maximum amplitudes obtained from the 1877 Mw 8.8 earthquake tsunami modeling with different focal depths in Chapter 3. are also plotted in Figure 65, which are close to the values of the mean rupture width. It can be seen that the maximum tsunami wave amplitude does not corresponds to the minimum focal depth, but corresponds to a focal depth of 30 to 40km instead. The spectral analysis in Chapter 3 reveals the maximum tsunami amplitude is due to the increase of spectral amplitude of a large bandwidth between 65

min are 160 min, which reaches maximum with the 40km focal depth at both the source (Gauge 1) and the entrance of the Bay of Concepcion (Gauge 6). Figure 65 shows that tsunamis generated by a magnitude Mw8.8 earthquake appears to have the largest maximum amplitude range, which is minimum for shallower earthquakes and maximum at 40km focal depth approximately. This range changes from 0.3 to 0.5m. On the contrary, smaller earthquakes almost converge into a single curve, with no significant amplitude range. Therefore, the size and shape of the rupture area has a stronger influence on large-earthquake tsunamis. As a first approximation, a 2nd degree polynomial curve could be fitted to the average values given by the upper, mean and lower bounds of each earthquake. These polynomials are plotted as a continuous line and the general equation is given by equation (9), in which $\eta_{\max\_0}$ is the maximum tsunami wave amplitude without the effect of tides, h_c is the focal depth or the depth at the centroid of the rupture area and the coefficients a, b and c define the shape of the polynomial. These coefficients were defined based on a least square method as a function of the earthquake magnitude only.

$$\eta_{\max\_0} = ah_c^2 + bh_c + c \tag{9}$$

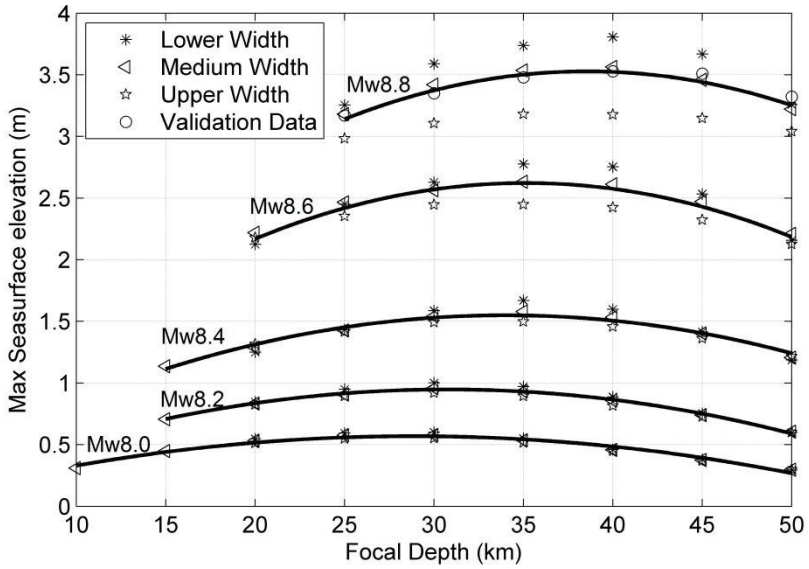

Figure 65. Maximum sea surface elevation as a function of the earthquake magnitude and focal depth. Upper and lower bounds of the rupture width are also indicated.

The polynomial coefficients as a function of the earthquake magnitude were defined based on the model adjustment, thus the relative root mean square error (RRMSE) was a minimal. In order to compute this error, the values given by the

simulated seasurface elevation (S) given in Figure 65 and the adjusted curve (A) given by equation (9) were related by means of equation (10) for each earthquake magnitude.

$$RRMSE = \sqrt{\frac{1}{n}\sum_{j=1}^{n}\left(\frac{A_j - S_j}{A_j}\right)^2} \tag{10}$$

The minimum values of the RRMSE was obtained for a 1st degree polynomial for coefficient a, a 3rd degree polynomial in coefficient b, and an exponential curve for coefficient c. The coefficient b showed to be the most sensitive coefficient, such that small changes in this parameter meant large changes in RRMSE. It is important to mention that the 3rd degree polynomial for coefficient b is not the best fit to the calculated points; it is an average of lineal and cubic regression instead, thus the minimum value of RRMSE is obtained. The analysis of coefficient b is shown in Table 7 as a function of the fitting curve. It is possible to see that the average curve reduced the relative error significantly, such that an average error of 5.51% is obtained between the simulated values and the adjusted curve.

Table 7. RRMSE for different fitting curves of coefficient *b*

Earthquake Magnitude	RRMSE of coefficient *b* (%)		
	Lineal	Cubic	Average Lineal and Cubic
8.8	0.91	1.90	0.83
8.6	4.06	4.80	3.10
8.4	13.16	3.18	6.32
8.2	13.09	33.07	10.26
8.0	43.46	43.46	7.01
Average	14.94	17.28	5.51

The plots of all polynomial coefficients together with their respective adjusted curves are shown in Figure 66. The present forecast model takes into account of the lower and upper width of the rupture area. Figure 66 (d) shows the values adopted for the upper and lower bounds of the mathematical model. These bounds were obtained from displacing the curve upward or downward with respect to the medium curve. The adjusted curve defined by equation (4) has a maximum relative error of 10% (See Table 7) however, this maximum error is obtained only for the 8.2 earthquake, while the 8.8 earthquake gives an error as low as 0.83%. Therefore, the lower and upper bounds must

include the error of the adjusted curve with respect to the simulated values. Subsequently, the proposed expression of the upper and lower bounds is given in equation (11).

$$\Delta\eta = RMSE_m + \frac{1}{2}(RMSE_u + RMSE_l) \tag{11}$$

where RMSE is the Root Mean Square Error, and the subindex m denotes the error of the adjusted curve with respect to the simulated values, while u and l represents the error of the upper and lower simulated values with respect to the mean simulated values, respectively. The RMSE is computed as given in equation (12).

$$RMSE = \sqrt{\frac{1}{n}\sum_{j=1}^{n}\left(A_j - S_j\right)^2} \tag{12}$$

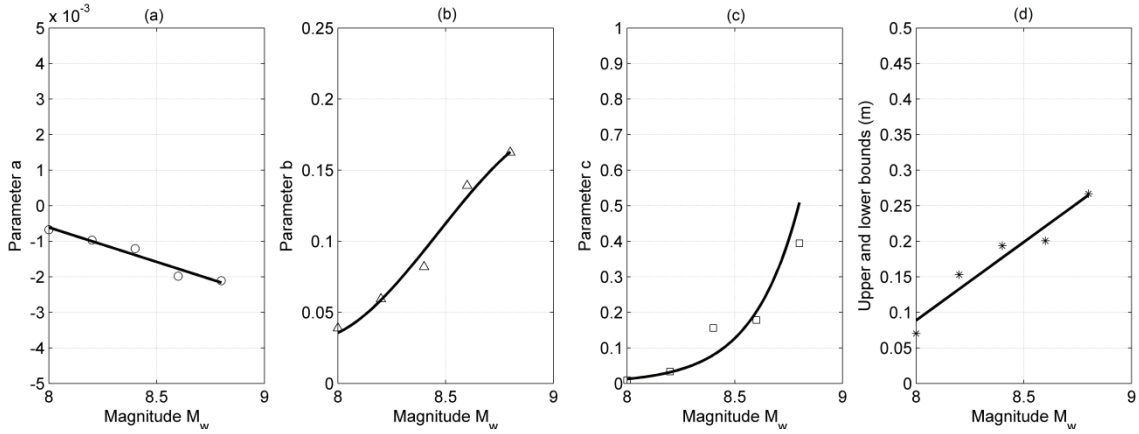

Figure 66. Variation of the polynomial coefficients and upper and lower bounds of the curves as a function of the earthquake magnitude

Figure 67 shows the results of the adjusted quadratic model given by equation (9) with the polynomial coefficients obtained from the curves in Figure 66. The curves of the lower and upper bounds of the model are computed as $\eta_{max\_0} \pm \Delta\eta$, where $\Delta\eta$ was defined in equation (11). It can be seen that the model represents well the behavior of the simulated values, and the bounds depend on the earthquake magnitude, thus the larger the magnitude, the wider the bounds. In general, all simulated values of maximum tsunami amplitude are bounded by the upper and lower limits, except for the earthquake magnitude Mw8.8, where few values are lower than the bounds. However, the forecast model would be in the safe side and can be deemed to be conservative. In the case of the earthquake of magnitude 8.4 the maximum sea surface elevation is over-predicted, while in the case of the 8.2 it is under-predicted. Nevertheless, the bounds

defined in equation (11) allow computing a wide range of maximum wave amplitude, such that all simulated values are bounded by the adjusted model.

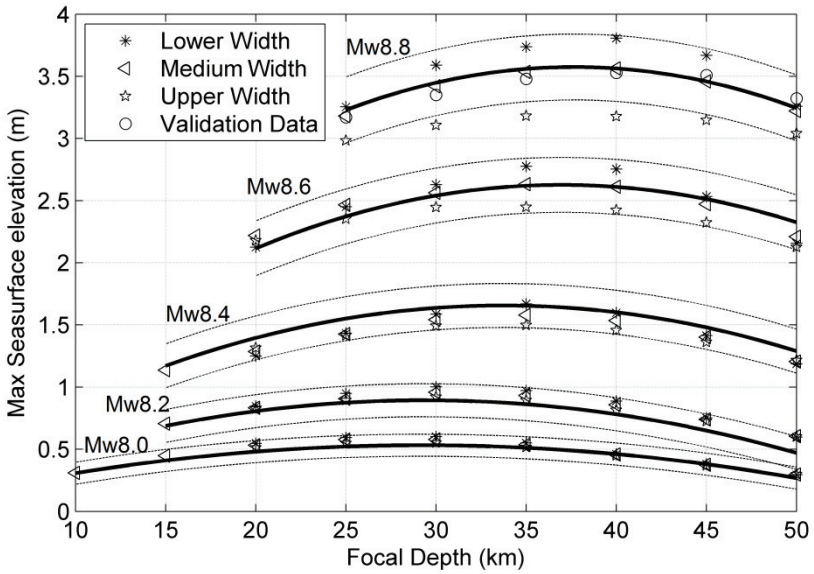

Figure 67. Maximum sea surface elevation as a function of the focal depth and the adjusted models for upper, lower and medium values.

The effect of the tide on the maximum sea surface elevation is shown in Figure 68. The left hand side figure shows the maximum sea surface elevation at Talcahuano as a function of the tide level for several earthquake magnitudes. From this figure it is apparent that the maximum sea surface elevation increases linearly as the tide level increases. In addition, the computed correlation coefficients are higher than 0.98. Therefore, it is possible to define an equation for the maximum sea surface elevation as given in equation (13)

$$\eta_{max} = m * \eta_{tide} + \eta_{max\_0} \tag{13}$$

In which η_{max_0} is the maximum sea surface elevation without considering the effect of the tide which was defined in equation (9), and m represents the slope of each lineal curve and is a function of the earthquake magnitude. Figure 68(b) shows the relation between the coefficient m and the earthquake magnitude. It can be seen that all values are around 1. A particular case is the earthquake of magnitude 8.8, where this coefficient m is 0.88, which means that the maximum sea surface elevation does not increase in the same proportion as the tide does. However, if a factor of 1 is assumed, the predicted maximum elevation would be conservative, and the RRMS error

computed by equation (10) would be only 0.42%. Therefore, the tide was included by just adding the tide level to the maximum sea surface elevation with no tide.

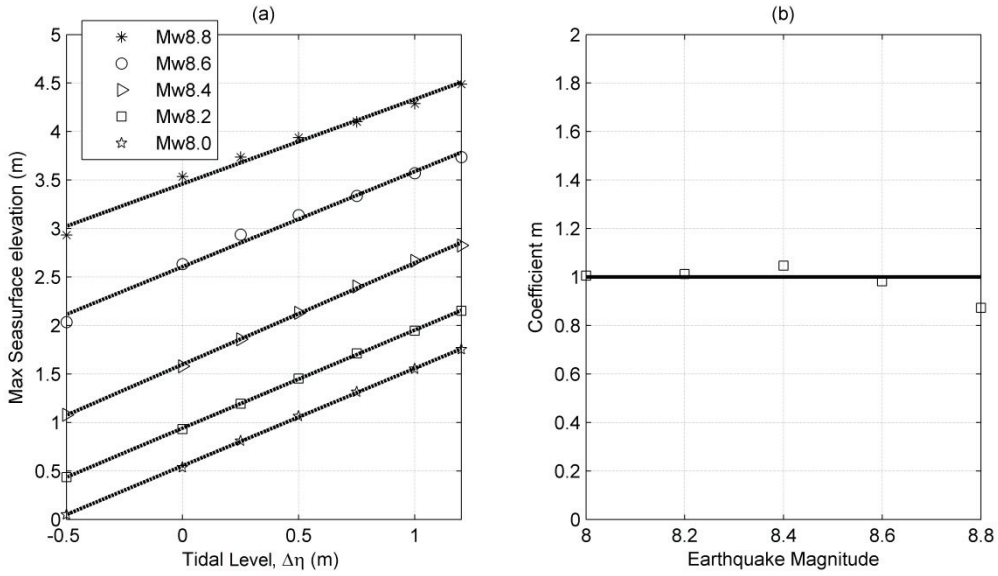

Figure 68. Effect of tide on maximum sea surface elevation. a) Maximum sea surface elevation as a function of the tide level and the earthquake magnitude. b) Relationship between the earthquake magnitude and the coefficient m (slope of the curves given in a).

Considering now equation (9), (11) and (13), the mathematical model of the maximum sea surface elevation at Talcahuano can be defined as follows

$$\eta_{max} = \eta_{tide} + a(M_w)h_c^2 + b(M_w)h_c + c(M_w) \pm \Delta\eta(M_w) \quad (14$$

In which η_{tide} is the tide level at the moment of maximum inundation at Talcahuano, h_c is the focal depth at the centroid of the rupture area, $a(M_w)$, $b(M_w)$ and $c(M_w)$ are the polynomial coefficients which are function of the earthquake magnitude, and $\Delta\eta(M_w)$ is the maximum seasurface elevation bounds. The tide level at moment of maximum inundation is computed as the tide level 4 hours and 45 min after the earthquake, as seen in Figure 24. The general expressions for each coefficient are given in Table 8.

Table 8. Mathematical expressions of all coefficients given in equation (14)

Coefficient	Equation
$\boldsymbol{a}$	$1.9407 \times 10^{-3} M_w + 1.4915 \times 10^{-2}$
$\boldsymbol{b}$	$-3.70645 + 94.1205 M_w^2 - 397.1676 M_w + 1{,}114.5581$
$\boldsymbol{c}$	$e^{(4.625127 M_w - 41.376650)}$
$\boldsymbol{\Delta\eta}$	$0.2204 M_w - 1.6742$

4.4. Example of Application

In order to apply the forecast model, a tsunami generated by an earthquake of arbitrary magnitude was simulated. This event was not included in the development of the model. Therefore, the maximum tsunami wave amplitude obtained from the numerical simulation of this event was compared with the maximum wave amplitude range given by the forecast model. The selected earthquake corresponds to an event of magnitude 8.7, and the assumed source parameters are the followings: L=395km, W=120km, D=10m, and a focal depth of 37km. The other parameters such as the strike, dip and rake angles remained constant. In addition, a tide level of 60cm was assumed at Talcahuano during the arrival of the maximum tsunami wave.

Figure 69 shows the result of the numerical simulation and the forecast model. The dotted lines represent the upper and lower bounds estimated from the forecast model given in equation (14), while the asterisk corresponds to the maximum tsunami wave amplitude obtained from the numerical simulation with NEOWAVE. Both results included the tide level. It can be seen that the numerical simulation (3.608m) is bounded by the forecast model. The upper and lower bounds corresponding to a focal depth of 37 km are 3.9572m and 3.4712m, respectively.

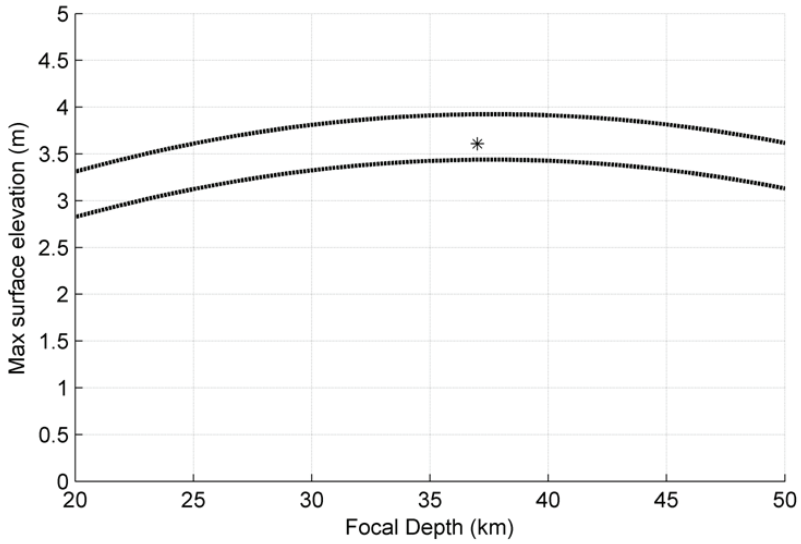

Figure 69. Maximum tsunami wave amplitude for a tsunami generated by an earthquake of magnitude 8.7. The dotted lines indicate the upper and lower limits obtained from the forecast model given in table5, while the asterix denotes the maximum tsunami wave amplitud

Chapter 5 Conclusions

The behavior of past tsunamis and their effects on the Biobio Region, Chile, were analyzed by means of numerical simulations. The tsunami behavior is strongly influenced by the morphology of the study area, and the present thesis enhanced the understanding of the behavior of the 2010 Chile tsunami based on two different aspects: the tsunami resonance in the Bay of Concepcion, and the presence of the Biobio submarine canyon at the northern side of the Gulf of Arauco.

The natural oscillation modes of the Bay of Concepcion were estimated by means of the Empirical Orthogonal Functions. This method was demonstrated to give reasonable oscillations periods for the Bay of Concepcion. The fundamental period of the Bay was computed to be 95min, which is larger than previous calculations based on theoretical expressions. The main reason for such a difference is the influence of the continental shelf on the oscillation modes, which is not considered in the theoretical expressions. The spectral analysis of past tsunamis demonstrated that tsunami waves excite natural oscillation modes of the Bay, and hence a large amplification area can be observed within the Bay. In addition, a coupling between the shelf resonance and bay oscillations was observed. The tsunamis from Central and Northern Chile excited the fundamental oscillation mode, which is an along-the-bay oscillation, thus large amplification take place at the southern shore of the Bay. The tsunami from southern Chile excited higher frequency modes, which are across-the-bay oscillations rather than the fundamental mode; therefore, the inundation at the southern shore was lower.

The most important variables which influence tsunami propagation over submarine canyons are the length and width of the canyon. Less important, but not negligible, is the effect of the depth of the canyon. The canyon causes a spatial variation of the wave amplitude along the coastline. While the runup in front of the canyon is always lower than in the case without the canyon, there are wave amplitude amplification zones at each side of the canyon. The lower value of runup in front of the canyon is highly influenced by the canyon size: the larger the length and deeper the depth, the lower the runup in front of the canyon head. Actually, for large canyon lengths, the run up could be as low as 20% of the runup without the canyon, while small canyon lengths have little effects on tsunami runup. In addition, numerical simulations of the 2010 Chile tsunami over the Biobio Canyon were shown to be in good agreement with the tsunami behavior over the idealized bathymetry. The submarine canyon

decreases the wave amplitude at the area in front of the canyon, such that amount of sea water surging into the river is greatly reduced. The canyon induces a diffraction-refraction-transmission process on the wave front, and thus changes direction and propagates parallel to the coast. In addition, the presence of Santa Maria Island enhances the diffraction process and the bathymetry within the Gulf of Arauco enhances the refraction process. These processes explain the large tsunami runup at the southern shore of the Gulf. The behavior of the wave front given by the numerical simulation, and elucidated in the present analysis, is in close agreement with that described by witnesses' of the event. Nevertheless, the present research has highlighted the very important concept (and up to now largely unreported phenomenon) that underground canyons *by themselves* result in a *comparative* reduction of the amplitude of the wave directly in front of them, and a magnification to the sides of them.

The analysis of possible future tsunamis affecting the Bay of Concepcion is focused on tsunamis generated in the Arica-Tocopilla source region in Northern Chile. Since the analysis of the historical event of 1877 revealed that this event took place during a period of neap tides, and the maximum tsunami amplitude at Talcahuano (3 m) occurred during low tide, it is possible to conclude that tide level decreased the effect of the tsunami. Therefore, the analysis of future tsunamis must include the effect of a 1.8 m tidal range in the study area. Keeping this in mind, the first tsunami forecast model for Talcahuano was developed. This model uses the earthquake magnitude, the focal depth and tide level to determine the maximum tsunami amplitude. Despite this model being restricted to earthquakes inside the Arica-Tocopilla source region, it represents an important tool to easily and quickly estimate the maximum tsunami amplitude at Talcahuano.

Future research will analyze the tsunami resonance in other semi-enclosed basins such as the Bay of Coliumo, San Vicente and Coronel in order to analyze the influence of the continental shelf on tsunami resonance. In addition, in the case of submarine canyons, other variables such as the orientation, the distance to the coast and the continental slope will be studied in detail. Moreover, tsunamis generated by landslides inside the canyon should be also considered as a possible hazard. Finally, further studies can extend the forecast model to include the effect of far field tsunamis from any place in the Pacific Ocean.

References

Aranguiz, R., (2011) “Preliminary Study on the effect of Biobio Canyon on Tsunami Propagation”, XXth Congress on Hydraulic Engineering, October 2011, Santiago, Chile. (in Spanish).

Aranguiz, R, (2012) The effect of a submarine canyon on tsunami propagation in the Gulf of Arauco, Chile. Int. Conf. of Coastal Eng.,ICCE2012, ASCE, Santander, Spain.

Aránguiz (2013). “Generation of the 1960 tsunami in southern Chile” XXIst Congress on Hydraulic Engineering, October 2013, Concepción, Chile. (in Spanish).

Aránguiz, R., and Belmonte, A., (2012). “The Effect of a tsunami generated in northern Chile on the Bay of Concepcion”. XXV Latinamerican Congress of Hydraulics, San José, Costa Rica. September 9th-12th, 2012. (in Spanish).

Aránguiz, R., Shibayama, T. (2013), Effect of Submarine Canyons on tsunamis propagation: Case study of Biobio Canyon, Coast. Eng. J(55):22. DOI:10.1142/S0578563413500162.

Aránguiz, R., Shibayama, T., Yamazaki, Y. (2013), Tsunamis from the Arica-Tocopilla Source Region and their Effects on Ports of Central Chile. Natural Hazards 12/2013; DOI:10.1007/s11069-013-0906-5.

Barrientos, S., Ward, S., (1990). The 1960 Chile Earthquake: inversion for slip distribution from surface deformation. Geophys. J. Int, 103, 589-598.

Barrientos, S.. (1991), “Large events, seismic gaps, and stress diffussion in Central Chile”. In Tectonic of the southern Central Andes, K. -J . Reutter, E. Scheuber, and P, J, Wigger Editors, 111-117.

Barrientos, S., (2007). “Earthquakes in Chile” in: Moreno, T., & Gibbons, W., (eds). The Geology of Chile. Geological Society, London, pp263-288

Barrientos, S. (2010). “Updated Technical Report May 27th, 2010-Cauquenes Earthquake February 27of 2010” (In spanish). Servicio sismológico de la Universidad de Chile, [available online at http://www2.ing.puc.cl/~wwwice/sismologia/INFORME_TECNICO%20(may%2027).pdf].

Bellotti, G., Briganti, R., Beltrami, G., M., Franco, L., (2012), Modal analysis of semi-enclosed basins. Coastal Engineering 64 (2012) 16–25.

Bilek, S. L. and Ruff, L., J., (2002). “Analysis of the 23 June 2001 Mw = 8.4 Peru underthrusting earthquake and its aftershocks”. Geophys. Res. Lett., 29 (20), 1960, doi:10.1029/2002GL015543

Birkman, J., 2006. Measuring vulnerability to promote disaster-resilient societies: Conceptual frameworks and definitions, In: J. Birkmann (Ed.): Measuring Vulnerability to Natural Hazards: Towards Disaster Resilient Societies. Tokyo: United Nations University Press. Pp. 9-54

Björnsson, H., Venegas, S., A., 1997, A Manual for EOF and SVD Analyses of Climatic Data. Department of Atmospheric and Oceanic Sciences and Centre for Climate and Global Change Research McGill University.

Canals, M., Puig, P., Durrieu de Madron, X., Heussner, S., Palanques, A., & Fabres, J., (2006) “Flushing submarine Canyons”, Nature, vol 444, 16 November 2006, doi:10.1038.

Chlieh, M., Perfettini, H., Tavera, H., Avouac, J-P., Remy, D., Nocquet J-M., Rolandone, F., Bondoux F., Gabalda, G., Bonvalot, S., (2011). “Interseismic coupling potential along the Central Andes subduction zone”. Journal of Geophysics research, vol 116, B12405, doi:10.1029/2010JB008166.

Choi, B. H , Pelinovsky, E., Kim, D. C., Didenkulova, I. & Woo, S.-B., (2008) “Two- and Three Dimensional Computation of Solitary Wave Runup on Non-plane Beach”, Nonlinear Processes in Geophyscs, 15, 489-502.

Cifuentes, I. (1989). The 1960 Chilean Earthquakes. Journal of Geophysical Research, vol 94, N° B1, pp 665-680.

Comte, D., Pardo, M., (1991). “Reappraissal of great historical earthquakes in the northern Chile and southern Peru seismic gap”. Natural Hazards, v.4, p.23-44, doi: 1.1007/BF00126557.

Concejo Municipal, (2010) “Sesión Ordinaria N° 07/2010, miércoles 3 de marzo de 2010”, Ilustre Municipalidad de San Antonio, 21pp. (in Spanish).

Condie, K.C. (1997). Plate tectonics and crustal evolution (4th ed.). Butterworth-Heinemann. p. 282. ISBN 978-0-7506-3386-4. Retrieved 2010-06-18.

Delouis, B., Nocquet, J., & Valeé, M., (2010) “Slip distribution of the February 27, 2010 Mw=8.8 Maule Earthquake, central, Chile, from static and high-rate GPS, InSAR and teleseismic data”, Geophysical Research Letters 37, L17305.

Didenkulova, I., & Pelinovsky, R., (2011) “Run ups of tsunami waves in U shapes bays”, Pure and Applied. Geophysics. 168, 1239-1249.

Divyalakshmi K., S., Rammohan, V., & Ramana Murthy, M., V., (2011) "Modification of Tsunami Wave by Submarine Canyon: Case Study of Multiple Canyons at South East Coast of India", Marine Geodesy, 34:2-15, 2011.

Duda, S. J., 1963. Strain release in the circum-pacific belt, Chile, 1960, J. geophys. Res., 68,5531-5544.

Ferraras, S. F., (1978), Tsunami resonant condition of Conceptión Bay (Chile). Marine Geodesy, 1:4, 355-360

Fritz, H. M., Petroff, C. M., Catalán, P. A., Cienfuegos, R., Winckler, P., Kalligeris, N., Weiss, R., Barientos, S., Meneses, G., Valderas, C., Ebeling, C., Papadopoulus, A., Contreras, M., Almar, R., Dominguez, J. C., & Synolakis, C. E., (2011) "Field Survey of the 27 February 2010 Chile Tsunami", Pure and Applied. Geophysics. Apringer Basel AG.

Gica, E., Spillane, M.C., Titov, V.V., Chamberlin, C.D., and Newman J.C., (2008). "Development of the forecast propagation database for NOAA's Short-term Inundation Forecast for Tsunamis (SIFT)" . NOAA Technical Memorandum OAR PMEL-139.

Gil, J. (1945). "Charles Darwin, viaje de un naturalista alrededor del mundo", Librería El Ateneo, Buenos Aires Argentina.

Grilli, S., T., Ioualalen, M., Asavanant, J., Shi, F., Kirby, J. and Watts, P., (2007). Source constraints and model simulation of the December 26, 2004 Indian Ocean Tsunami. J. Waterway Port Coastal Ocean Eng. ASCE 133(6):414-428

Grupo de Ingeniería Oceanográfica y de Costas, (2000) "Documento de Referencia, Vol 1: Dinámicas". Universidad de Cantabria. (in Spanish)

Goring, D. G., [1978] "Tsunamis: The propagation of long waves onto a shelf", Thesis for Degree of Doctor of Philosophy, California Institute of Technology, Pasadena, California.

Guibourg, S., Heinrich, P., Roche, R., (1997). "Numerical modeling of the 1995 Chilean tsunami. Impact on French Polynesia". Geo Res Letters, vol 24, N°7, p775-778

Haiyun, W., Xiaxin, T., (2003). "Relationships between moment magnitude and fault parameters: theoretical and semi-empirical relationships". Earthquake engineering and engineering vibration. Vol 2 N°2, pp201-211.

Hayes, G. (2010). “Finite fault model, updated result of the feb 27, 2010 Mw 8,8 Maule Chile Earthquake”. National Earthquake Information Center (NEIC) of United States Geological Survey2010. [available on : http://earthquake.usgs.gov/earthquakes/eqinthenews/2010/us2010tfan/finite_fault.php].

Henry, R. F., Murty, T. S. Tsunami Amplification due to Resonance. N. Shuto (eds.), Tsunami: Progress in Prediction, Disaster Prevention and Waming, 117·128.

Imamura, F., Yalciner, A., & Ozyurt, G., (2006), “Tsunami Modelling Manual, TUNAMI model”. IOC Manuals and Guides N°30, IUGG/IOC TIME PROJECT.

Ioualalen, M., Pelynovsky, E., Asavanant, J., Lipikorn, R., & Deschamps, A., (2007) “On the weak impact of the 26 Indian Ocean tsunami on the Bangladesh Coast”, Nattural. Hazards and Earth System. Science., 7, 141–147.

Jinadasa, S.U.P (2008) “Interaction of Tsunami wave propagation with coastal bathymetry and geomorphology; a case study in Sri Lanka”, General Bathymetric Chart of the Oceans (GEBCO) Science day 2008, Japan Coast Guard, Tokyo, Japan.

Kanamori, H. and Cipar, J.J., (1974). Focal process of the Crreal Chilean earthquake May 22, 1960, Phys. Earth Planet. Inter., 9, 128-136, t 974.

Kundu, A. (2007): Tsunami and Nonlinear Waves, Springer Science+Business Media.

Lagos, M., (2000). Tsunamis de origen cercano a las costas de Chile. Revista de Geografía Norte Grande, 27: 93-102.

Lagos, M., Gutierrez, D., (2005). Simulación del tsunami de 1960 en un estuario del centro-sur de Chile. Revista de Geografía Norte Grande, 33: 5-18.

Larrañaga, E. (2010). “Anexo IV Análisis del proceso de toma de Decisiones”: (http://www.armada.cl/prontus_armada/site/artic/20100325/asocfile/20100325094239/anexo_iv.pdf).

Levin, B., & Nosov, M. (2009) “Physics of Tsunami”, Springer Science+Business Media.

Loomis, H. G., (1973). Anew method for determining normal modes of irregular bodies of water with variable depth. Hawaii Institute of Geophysics reports HIG-73-10 (NOAA-JTRE-86), p 27.

Lomnitz, C., (1970). Major Earthquakes and Tsunami in Chile during the period 1535 to 1955. Geol. Rundschau 59, 3, 938-960.

Lynett, P., J., (2011) “Effect of a Shallow Water Obstruction on Long Wave Runup and Overland Flow Velocity”, Journal of Waterway, Port, Coastal and Ocean Engineering, Vol 133, N° 6 pp455-462

Madariaga, R., (1998), “Sismicidad en Chile”. Física de la tierra, 10, 221-258.

Mikami, T., Shibayama, T., Takewaka, S., Esteban, M., Ohira, K., Aranguiz, R., Villagran, M., Ayala, A., (2011). Field survey of the tsunami disaster in Chile 2010, Journal of Japan Society of Civil Engineers, Ser. B3 (Ocean Engineering), 67(2), I_529-I_534. (In Japanese with English abstract)

Mofjeld, H. O., Titov, V. V., Gonzalez, F. I., & Newman, J. C., (2000), “Analytic Theory of Tsunami Wave Scattering in the Open Ocean with Application to the North Pacific”. NOAA Technical Memorandum OAR PMEL-116.

Murata, S., Imamura, F., Katoh, K., Kawata, Y., Takahashi, S., & Takayama, T., (2010) “Tsunami: To survive from tsunami”, Advanced Series on Ocean Engineering-Vol 32.

Okada, Y., (1985) “Surface Deformation of Shear and Tensile Faults in a Half-Space”, Bulletin of the Seismological Society of America, 75, [4], 1135-1154.

Okal, E., A., Borrero, J., C., Synolakis, C., E., (2006). Evaluation of Tsunami Risk from Regional Earthquakes at Pisco, Peru. Bulletin of the Seismological Society of America, Vol. 96, No. 5, pp. 1634–1648, October 2006, doi: 10.1785/0120050158

Olsen, K., and Hwang, L., S., (1971), Oscillation in a Bay of Arbitrary Shape and Variable Depth. Journal of Geophysical Research. vol. 76, NO. 21.

Ozaki, T., (2011). “Outline of the 2011 off the Pacific coast of Tohoku Earthquake (Mw 9.0) —Tsunami warnings/advisories and observations—“, Earth Planets Space, 63, 827–830

Papazachos B. C., Scordilis E. M., Panagiotopoulos D. G., Papazachos C. B. and Karakaisis G. F. (2004). “Global Relations between seismic fault parameters and moment magnitude of Earthquakes”. Bulletin of the Geological Society of Greece vol. XXXVI, 2004.

Pelinovsky, E., Choi, B., Talipova, T., Woo, S., Dong., K, [2010] “Solitary wave transformation on the underwater step: Asymptotic theory and numerical experiment”. Applied Mathematics and Computation, 217, pp. 1704-1718.

Peyrat, R. Madariaga,E. Buforn,J. Campos,G. Asch and J. P. Vilotte. (2010). “Kinematic rupture process of the 2007 Tocopilla earthquake and its main

aftershocks from teleseismic and strong-motion data". Geophys. J. Int. (2010) 182, 1411–1430.

Quezada, J., Jaque, E., Belmonte, A., Fernández, A., & Martínez, C., (2010) "The third tsunami wave in Biobio Region bays during the Chilean 27th February 2010 earthquake", American Geophysical Union Chapman Conference, Valparaiso, Viña del Mar and Valdivia, Chile. May 14-24, 2010.

Quezada, J., (2000) "Visión General de los Riesgos Geológicos en la Comuna de San Pedro de la Paz, Chile Centro Sur". Congreso Chileno n° 10, Puerto Varas. (in Spanish).

Rabinovich, A., B., (2009). Seiches and Harbor Oscillations. In: Kim YC (ed) Handbook of Coastal and Ocean Engineering. World Scientific Publ., Singapur, pp 139-236

Roeber, V., Yamazaki, Y. and Cheung, K., F., (2010). Resonance and impact of the 2009 Samoa tsunami around Tutuila, American Samoa, Geophysical Research Letters, vol. 37, L21604, doi:10.1029/2010GL044419

Ruegg, J., C., Olcay, M., Lazo, D., (2001). "Co-post- and pre- seismic displacement associated with the Mw=8.4 southern Peru earthquake of 23 June 2001 from continuous GPS measurements". Seismol. Res. Lett., 72, 673-678.

Sandoval, F., Ferraras, S., (1993), Tsunami Resonance of the Gulf of California. In S. Tinti (ed), Tsunamis in the World, \07-119.

Soloviev, S., L., & Go, Ch., N., (1975) "A catalogue of tsunamis on the Eastern shore of the Pacific Ocean", Nauka Publishing House, Moscow, 202p

Sobey, R., (2006), Normal mode decomposition for identification of storm tide and tsunami hazard, Coastal Engineering 53 (2006) 289 – 301

United Nations (2005) Hyogo Framework for Action 2005–2015: Building the Resilience of Nations and Communities to Disasters, World Conference on Disaster Reduction, 18–22

UNESCO/IOC (2009), Hazard Awareness Risk Mitigation. Manuals and Guides No 50, ICAM Dossier No 5.

UNESCO/IOC (2012), "Sea Level Monitoring Facility", available at http://www.ioc-sealevelmonitoring.org/station.php?code=talc, (access: April 9th, 2012).

Shibayama, T., Esteban, M., Nistor, I., Takagi, H., Thao, N., D., Matsumaru, R., Mikami, T., Aranguiz, R., Jayaratne, R., Ohira, K. (2013). Classification of Tsunami and Evacuation Areas. Nat Hazards DOI 10.1007/s11069-013-0567-4

Shimozono, T., Sato, S., Okayasu, A., Tajima, Y., Fritz, H., Liu, H., & Takagawa, T., (2012). “Propagation and Inundation Characteristics of the 2011 Tohoku Tsunami on the Central Sanriku Coast”. Coastal Engineering Journal. Vol. 54, N°1, 1250004

Takahashi, R. (1961). A Summary Report on the Chilean Tsunami of May 1960. Report on the Chilean Tsunami of May 24, 1960, as observed along the Coast of Japan. Committee for the Field Investigation of the Chilean Tsunami of 1960.

Tolkova, E., and Power, W., (2011), Obtaining natural oscillatory modes of bays and harbors via Empirical Orthogonal Function analysis of tsunami wave fields. Ocean Dynamics 61:731-751.

Vakov, A., (1996). “Relationships between earthquake magnitude, source geometry and slip mechanism”. Tecnophysics 261, 97-113.

Vela, J., Pérez, B., González, M., Otero, L., Olabarrieta, M., and Canals, M., (2010). Tsunami resonance in the Palma de Majorca bay and harbor induced by the 2003 Boumerdes-Zemmouri Algerian earthquake (Western Mediterranean). in: Proceedings of 32nd International Conference on Coastal Engineering (ICCE 2010), ASCE, 2010.

Vargas, G., Farías, M., Carretier, S., Tassara, A., Baize, S., & Melnick, D., (2011), Coastal Uplift and Tsunami Effects Associated to the 2010 Mw 8.8 Maule Earthquake in Central Chile”. Andean Geology 38 (1):219-238.

Vidal-Gormaz, F., (1878). “Algunos datos relativos al terremoto de 9 de mayo de 1877, i a las ajitaciones del mar i de los otros fenómenos ocurridos sobre las costas occidentales de Sud-América”. En: Anuario hidrográfico de la marina de Chile n°4. Imprenta nacional; Santiago, Chile. pp. 458-480.

Watanabe, Y., Mitobe, Y., Saruwatari, A., Yamada, T., & Niida, Y., (2012) “Evolution of the 2011 Tohoku Earthquake Tsunami on the Pacific Coast of Hokkaido”, Coastal Engineering Journal. Vol. 54, N°1, 1250002

Well, D., and Coppersmith, K., (1994). “New empirical relationships among magnitude, rupture length, rupture width, rupture area and surface displacement”. Bulletin of Seismological Society of America, 84 (4): 974-1002.

Wyss, M. (1979). “Estimating maximum expectable magnitude of earthquakes from fault dimensions”. Geology, v. 7, p. 336-340

Yamazaki, Y., and Cheung, K. F. (2011) “Shelf Resonance and Impact of Near-field Tsunami generated by the 2010 Chile Earthquake”, Geophyical Research Letters, 38(12), L12605, doi: 10.1029/2011GL047508.

Yamazaki, Y., Cheung, K.F., and Kowalik, Z. (2011) “Depth-integrated, non-hydrostatic model with grid nesting for tsunami generation, propagation, and run-up”. International Journal for Numerical Methods in Fluids, 67(12), 2081-2107.

Yamazaki, Y., Kowalik, Z., and Cheung, K. F. (2009) “Depth-integrated, non-hydrostatic model for wave breaking and runup”, Int. J. Numer. Methods Fluids, 61(5) , 473-497.

Yeh, H., Robertson, I., Preus, J., (2005). Development of Design Guidelines for Structures that Serve as Tsunami Vertical Evacuation Sites. Washington Division of Geology and Earth Resources pp34.

List of Research Achievements

種類別 (By Type)	題名、　発表・発行掲載誌名、　発表・発行年月、　連名者（申請者含む） (theme, journal name, date & year of publication, name of authors inc. yourself)
Jounals	
○1)	Tsunamis from the Arica-Tocopilla Source Region and their Effects on Ports of Central Chile Natural Hazards, published 27 October, 2013, doi:10.1007/s11069-013-0906-5 **Aránguiz, R.**, Shibayama, T., Yamazaki, Y.
○2)	Effect of Submarine Canyons on tsunamis propagation: Case study of Biobio Canyon Coastal Engineering Journal, 55(4), 1350016, (2013) **Aránguiz, R.**, Shibayama, T.
○3)	Classification of Tsunamis and Evacuation Areas Natural Hazards, 67(2), 365-386, (2013) Shibayama, T., Esteban, M., Nistor, I., Takagi, H., Thao, N., D., Matsumaru, R., Mikami, T., **Aranguiz, R.**, Jayaratne, R., Ohira, K.
○4)	Tsunami Risk in Tubul Town: Extreme Events and Post-earthquake Territorial Transformations Revista Geografía Norte Grande, 53, 85-106 (2012), (In Spanish with English abstract) Martínez, C., Rojas, O., **Aránguiz, R.**, Belmonte, A., Altamirano, A. P. Flores
○5)	Use of trees as a tsunami natural barrier for Concepción, Chile Journal of Coastal Research, SI 64, 450-454, (2011) **Aránguiz, R.**, Villagrán, M., Eyzaguirre, G
○6)	Field survey of tsunami disaster in Chile 2010 Journal of Japan Society of Civil Engineers, Ser. B3 (Ocean Engineering), 67(2), I_529-I_534. (2011), (In Japanese with English abstract) Mikami, T., Shibayama, T., Takewaka, S., Esteban, M., Ohira, K., **Aranguiz, R.**, Villagran, M. & Ayala, A.
○7)	Numerical Simulation of the 2010 Chile Tsunami in the Bay of Concepcion with non-uniform initial condition Revista Obras y Proyectos, 8, 12-18, (2010), (In Spanish) **Aránguiz, R.**
○8)	Effect of tsunami breakwater as a mitigation measure at the Bay of Concepción Revista Obras y Proyectos, 8, 2-7, (2010), (In Spanish) Van Adrichem, R., **Aránguiz, R.**
Conferences	
○1)	Generation of the 1960 Tsunami in Southern Chile. XXI Chilean Congress of Hydraulic Engineering, Oct-2013, Chile, (in Spanish) **Aránguiz, R.**
○2)	Beach Profile Study of a Lacustrine System using a Low-Cost Wave Recorder Coastal Dynamics 2013, June 2013, France **Aranguiz, R.**, Villagrán, M.

種類別 By Type	題名、　発表・発行掲載誌名、　発表・発行年月、　連名者（申請者含む） (theme, journal name, date & year of publication, name of authors inc. yourself)
○3)	Tsunami propagation from northern Chile to the Bay of San Vicente, Chile XXXII Congress of Marine Sciences, Oct-2012, Chile, (In Spanish) **Aránguiz, R.**
○4)	Effect in the Bay of Concepcion of a tsunami from northern Chile XXV Latinamerican Congress of Hydraulics, Sept-2012, Costa Rica, (In Spanish) **Aránguiz, R.**, Belmonte, A.
○5)	The Effect of a submarine canyon on tsunami propagation in the Gulf of Arauco International Conference of Coastal Engineering, ICCE-2012, July-2012, Spain **Aránguiz, R.**
○6)	Stability of Ruble Mound Breakwater against Solitary Waves International Conference of Coastal Engineering, ICCE-2012, July-2012, Spain Esteban, M., **Aranguiz, R.**, Morikubo, I., Mikami, T., Danh Thao, N., Ohira, K., Ohtani, A., Shibayama, T.,
○7)	Preliminary study on the effect of Subamrine Canyons on tsunami propagation XX Chilean Congress of Hydraulic Engineering, Oct-2011, Chile, (In Spanish) **Aránguiz, R.**
○8)	The effect of the Santa María Island on Tsunami propagation XX Chilean Congress of Hydraulic Engineering, Oct-2011, Chile, (In Spanish) Jimenez, M., **Aránguiz, R.**
○9)	Disaster Mitigation after the 2010 Chilean Earthquake and Tsunami 8th Int. Workshop on Coastal Disaster Prevention, Sept-2011, Japan **Aranguiz, R.**,
○10)	Tsunami Inundation simulation in the Bay of Concepcion, Chile, using TUNAMI and Delft3D models European Geosciences Union, Assembly 2011. April-2011, Austria Van Adrichem, R., **Aranguiz, R**., Vatvani, D.
Research Projects	
1)	Enhancement of Technology for Development of Tsunami-Resilient Community JICA-SATREPS, period 2012-2015 Role: Leader of working group 2 in Chilean side
2)	Research and Integrated Managament of Natural Distasters Center (CIGIDEN) (Centro de Investigación y Gestión Integrada de Desastres Naturales). FONDAP (Chilean Government) 2013-2018 Role: Researcher